Chapter 5

Domain Structure on the Nanoscopic Scale

Experiments described in Chapter 4 suggest that crystal defects are the source of pseudoelasticity in UICs containing 2,10-undecanedione. The study of these defects will be examined below.

5.1 Probing Variations in Strain: Synchrotron White Beam X-Ray Topography

Synchrotron white beam X-ray topography (SWBXT)[1] is a diffraction experiment that can discern minute differences in strain with a spatial resolution on the order of approximately one micron. This technique, performed in conjunction with crystal stress-strain experiments, has made possible large advances in the understanding of ferroelasticity in urea inclusion compounds. The SWBXT experiments discussed in this chapter were performed by Dr. Mark Hollingsworth, Dr. Matthew Peterson, Dr. Mike Dudley and Dr. Balaji Raghothamachar, with the assistance of Dr. Govindhan Dhanaraj, at Brookhaven National Laboratory, in Brookhaven, NY. (In certain cases, the experimentalist is noted.)

In the SWBXT experiment, a stationary crystal is exposed to highly collimated radiation from a synchrotron light source, and its diffraction pattern is recorded on high-resolution film. An example topograph of a UIC crystal containing a mixture of 2,9-decanedione and 2-decanone is provided in Figure 5.1. (This topograph was collected by Balaji Raghothamachar.) The extremely high degree of beam collimation virtually eliminates blurring so that every reflection appears as an image of the diffracting power of crystal. Because the radiation is polychromatic, numerous Miller planes meet the

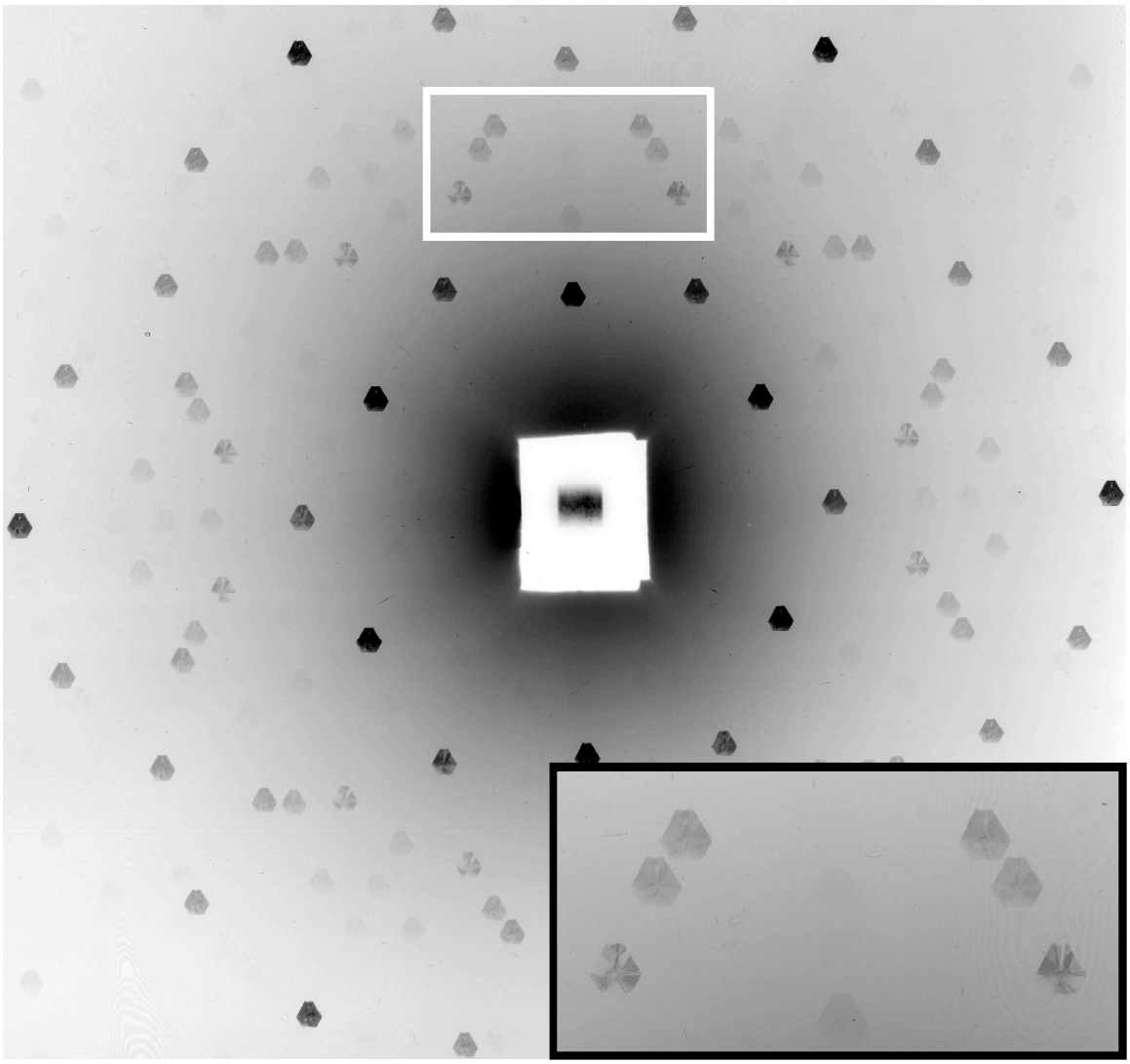

Figure 5.1 Synchrotron white-beam X-ray topography (SWBXT) of a UIC crystal grown from a methanol solution containing an 89.6:10.4 mixture of 2,9-decanedione and 2-decanone. The polychromatic incident radiation allows the Bragg condition to be met for numerous Miller planes of a stationary crystal so that each exposure produces a multitude of reflections. In this image, the darker reflections are overexposed, but the weaker reflections reveal variations in intensity between twins. The inset provides examples of how rotational twinning is visible with this technique. Here, a close-up image of the reflections bounded by the white box. The highly collimated incident radiation produces in each reflection a photographic image of the diffracting power of the crystal. For crystals in which different regions exhibit small differences in the magnitude or orientation of crystallographic strain, the positions of those regions within each image will be altered. In this topograph the images are undistorted, indicating hexagonal metric symmetry. This topograph was collected by Dr. Balaji Raghothamachar at Brookhaven National Laboratory.

Bragg condition for any given crystal orientation. Consequently, the exposure time is short (typically, around ten seconds) so that only the most intense reflections are exposed. In X-ray topography, the orientation of the diffracting planes is described using the **g** vector, which bisects the incident and diffracted beams.[1] The importance of the **g** vector will be further discussed below.

A consequence of using highly collimated, polychromatic radiation is that small differences in the magnitude or orientation of strain can be easily discerned in the exposed topograph. This effect is illustrated in the topograph[2] (Figure 5.2) of a crystal containing mostly 2,10-undecanedione and 2-undecanone. For this twinned ferroelastic crystal (see Sections 1.1 and 4.2), each reflection is observed as a cluster of images that appear quite unlike those of Figure 5.1. Neighboring sectors within the crystal possess different orientations of their spontaneous strain so that their images appear shifted relative to one another. Since opposite sectors are distorted along the same direction (see Figure 2.6), their reflections are shifted in the same fashion, and they remain paired in the topograph. However, the polychromatic radiation allows the diffraction of different wavelengths by differently strained (or oriented) regions. Thus, although SWBXT is very sensitive to strain, it does not provide a straightforward means of measuring strain.

5.1.1 Domain Structure and Ferroelasticity

The sensitivity of SWBXT to minor variations in strain makes it ideal for the study of ferroelasticity in urea inclusion compounds. A tentative conclusion from Chapter 4 is that the mother domain contains fewer stressed defects and is therefore lower in energy than the daughter domain. Using SWBXT, changes in crystallographic strain

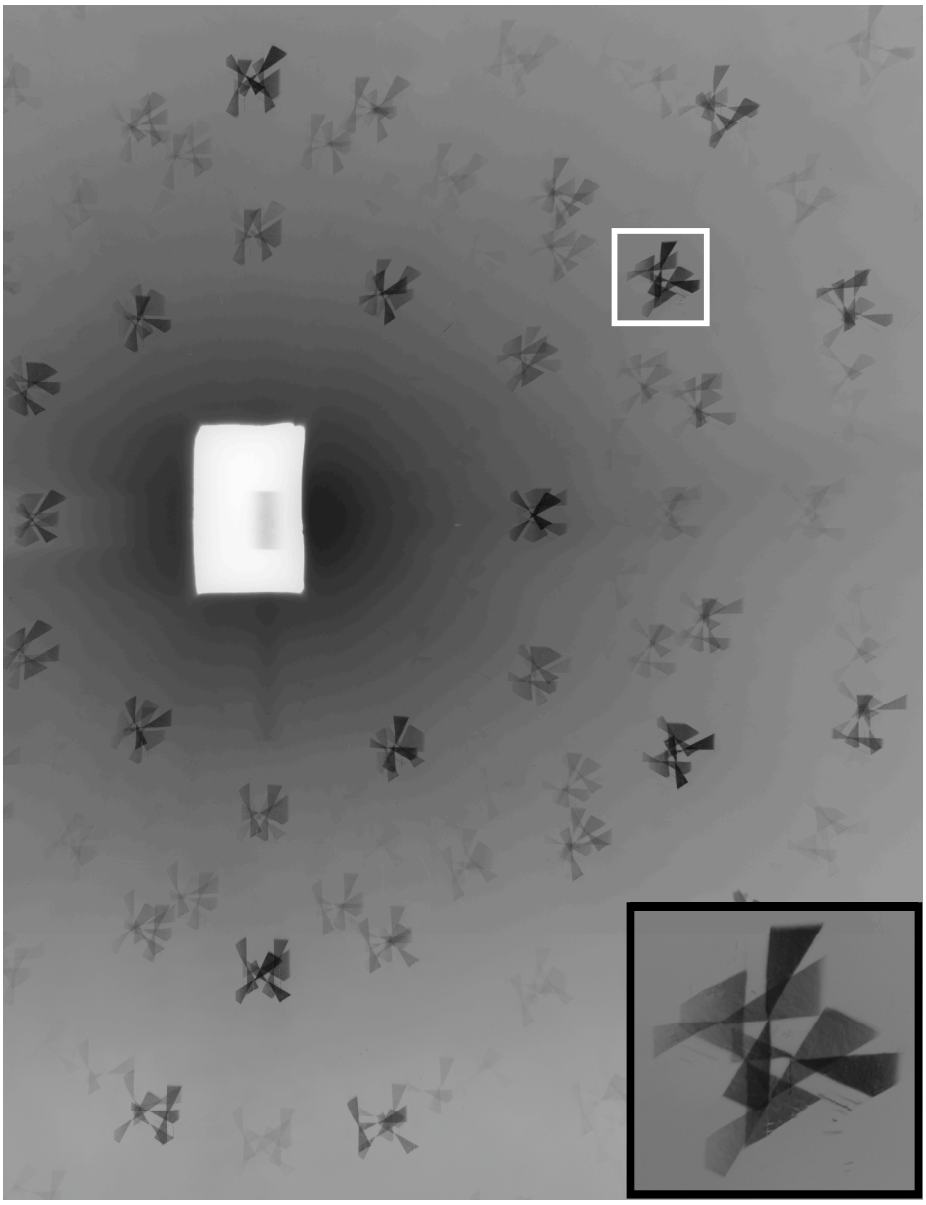

Figure 5.2 X-ray topograph of a UIC crystal grown from methanol solution containing a 98:2 mixture of 2,10-undecanedione and 2-undecanone. Unlike the topograph of 2,9-decanedione/urea (Figure 5.1), the reflections in this topograph do not look like the crystal itself. Inset is a close-up image of the cluster bounded by the white box. The strain in the crystal allows for sectors of different orientation to meet the Bragg condition at different wavelengths and angles. Thus, the topograph "appears as an exploded clusters of images in which each image corresponds to a particular Miller plane, and in which opposite sectors appear in pairs."* On closer inspection the sectors appear littered with fine striations. The nature of these striations is discussed in the text. This topograph was collected by Hollingsworth, Peterson, Dudley, Raghothamachar and Dhanaraj at Brookhaven National Laboratory.

*Excerpted from Hollingsworth, *et al*., *Cryst. Growth Des*., **5**, 2100-2116 (2005).

caused by ferroelastic domain switching and the growth of defect structure can be studied in minute detail. If, by virtue of possessing fewer defects, the mother domain is more perfect than the daughter, X-ray topographs recorded during *in situ* stress experiments should provide clues about those differences in perfection.

In these studies, UIC crystals containing predominantly 2,10-undecanedione and 2-undecanone were stressed, and the event was recorded with a combination of videomicroscopy (between crossed polars and with λ plate) and transmission-mode SWBXT. The results, presented in Figures 5.3 and 5.4, are striking. For crystals grown in solutions containing from 0 to 12% monoketone, plastic domain switching was observed. Figure 5.3a-c illustrates the experiment on a crystal grown from a 98:2 mixture of 2,10-undecanedione and 2-undecanone. (Unlike the other crystals discussed in this section, this crystal was not analyzed for guest content.) Topographs recorded for this crystal demonstrate that reflections from the switched sectors elongate to more than twice their original size when under stress (Figure 5.3b). Here, the applied stress has created within the crystal a broad range of crystallographic strains so that the topograph image appears smeared. However, the relative insensitivity of some of the sectors to the stress is also notable; these sectors did not switch because their strain was not oriented in the proper fashion.

Thus, the majority of changes in the topograph are concentrated into those sectors capable of domain switching. Upon release (Figure 5.3c), some relaxation of the patterns can be seen, although reflections from the distorted sectors are visibly altered from their appearance in Figure 5.3a. Since daughter domains are oriented differently from mother domains, their reflection positions will differ. Within these sectors, stripes can be seen

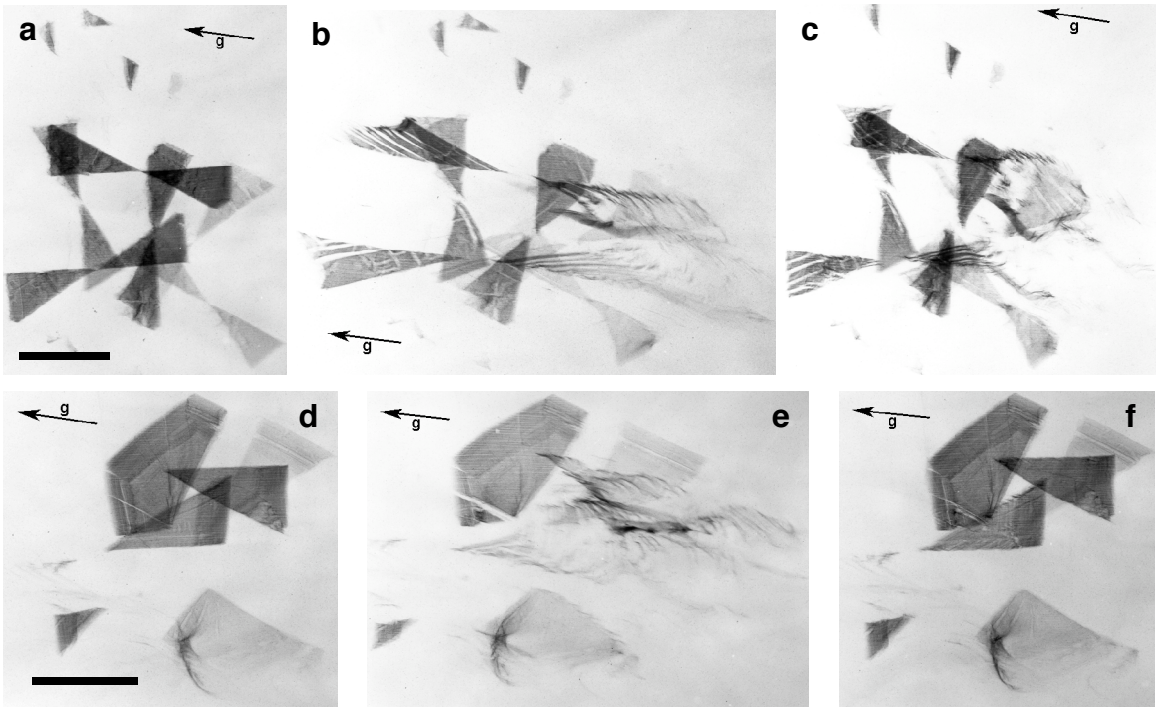

Figure 5.3 Synchrotron white beam X-ray topography stress experiments on UIC crystals containing mixtures of 2,10-undecanedione and 2-undecanone. **(a-c)** Plastic domain switching in a crystal grown from a solution containing 98% diketone. Transmission mode X-ray topographs of the same reflection at different stages of the stress experiment. Scale bar = 2.0 mm (on topograph **a**). The two-dimensional projection of the **g** vector onto each topograph image is denoted by the arrow. **(a)** Crystal before stress. **(b)** With 58 cN force applied horizontally. Here, the applied stress has stretched some images to more than twice their original size. **(c)** Following the release of stress, some of the images return to their original size. However, plastic domain switching produces a topograph that appears appreciably different from that shown in **a**. **(d-f)** Pseudoelastic domain switching in a crystal containing 84% diketone. Transmission mode X-ray topographs of the same reflection at different stages of the stress experiment. Scale bar = 2.0 mm (on topograph **d**). **(d)** Crystal before stress. **(e)** With 90 cN force applied horizontally. **(f)** Following the release of stress. Note that pseudoelastic reversion of the daughter domains appears much more complete in this crystal than for the crystal in **a**-**c**. Figure and caption adapted from Hollingsworth, *et al.*, *Cryst. Growth Des.*, **5**, 2100-2116, (2005). These topographs were collected by Hollingsworth, Peterson, Dudley, Raghothamachar and Dhanaraj at Brookhaven National Laboratory.

where plastic daughters were formed. In addition, topograph images of the stressed sectors appear somewhat distorted, suggesting a change in the overall domain structure of those regions.

For a crystal containing 16% 2-undecanone (by HPLC), the expected pseudoelastic response was observed. Figure 5.3d-f shows the experiment for this crystal. In the experiment, the applied stress again distorts the topograph images of the appropriate sectors to more twice their initial size. Optical images taken following stress release (not shown) show that the crystal has undergone pseudoelastic domain reversion. For this crystal, topograph images recorded following stress release are quite similar in shape and overall appearance to those taken prior to the stress; the subtle differences observable in these images are discussed below.

The stress experiment for a UIC crystal containing an 89:11 mixture of 2,10-undecanedione and 2-undecanone proved especially interesting (Figure 5.4). While under light stresses (applied horizontally), some distortion of switched sectors was noticeable. Furthermore, as illustrated in Figure 5.4b, portions the daughter formed under light stress can be observed to diffract as single crystals. Upon stress release, these reflections remain intact and are not heavily distorted; they persist following the release of much greater stresses as well (Figure 5.4d). A photomicrograph taken of the crystal after the stress experiment (Figure 5.4f) reveals the regions from which these reflections originate. Notable is the different orientations of these switched regions: for domain #1, the strain is oriented perpendicular to the horizontally applied stress (as expected), but for domains #2, the strain is not. For this region, the strain is oriented approximately 60° to

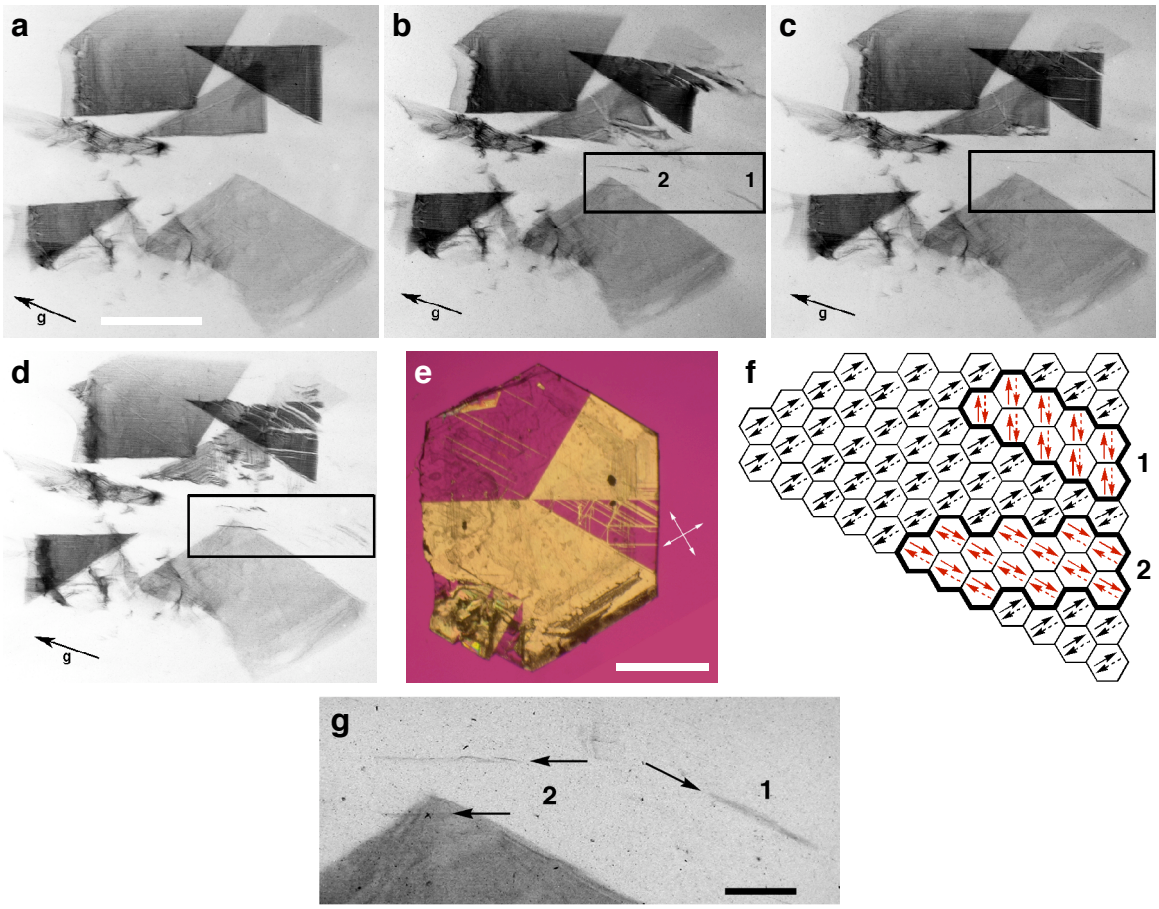

Figure 5.4 Plastic domain switching in a UIC crystal containing an 89:11 mixture of 2,10-undecanedione and 2-undecanone. **(a-d)** Transmission mode X-ray topographs of the same reflections collected at different stages of the stress experiment. Scale bar = 2.0 mm (on topograph **a**). **(a)** Crystal before stress. **(b)** Under 63 cN force applied horizontally. In this image the applied stress has switched the domains, and the sectors appear somewhat distorted. Close inspection of this topograph reveals the presence of small stripes, labelled **1** and **2** (in **b**). These were generated from the dark sector directly above them (note matching regions of decreased reflection intensity, especially visible in **c**). **(c)** Following the release of stress. Most of the distortion observed under stress has vanished, so the sectors in this topograph appear very similar in shape to those in **a**. A close-up of the area within the box is presented in **g** (scale bar = 0.5 mm). Here, reflections **1** and **2** remain visible. **(d)** X-ray topograph recorded following the release of 112 cN force. Some damage in the topograph is evident, yet reflections **1** and **2** are still discernible. **(e)** Photomicrograph of the crystal following the conclusion of the stress experiment (after **d**), taken between crossed polars (orientation shown with arrows) and with a λ plate. Here, the domains responsible for reflections **1** and **2** can be seen in the extinguished sector. Scale bar = 2.0 mm. A schematic of the domains observed in this sector is provided in **f**. Figure and caption adapted from Hollingsworth, *et al.*, *Cryst. Growth Des.*, **5**, 2100-2116, (2005). The topographs were collected by Hollingsworth, Peterson, Dudley, Raghothamachar and Dhanaraj.

the applied stress (as it was for the mother domain). Understanding this sort of ferroelastic behavior is important and will be discussed below.

The observation of diffraction by the daughter domain suggests that the damage incurred from the compressive force is small. This stands in contrast to the topograph images collected for crystals with smaller monoketone concentrations (*e.g.* Figure 5.3a-c). For crystals with small fractions of 2-undecanone, the application of large compressive forces produces topograph images that are appreciably distorted. With an 89:11 mixture of guests, however, the concentration of monoketone is small enough to yield a plastic response, yet large enough so that the shapes of the topographs for the daughters, which reflect the state of strain of these segments, are not highly distorted. For the daughters observed in the topographs, the relaxive impurity may facilitate defect repair to the extent that these domains are ordered and can diffract to produce relatively undistorted images.

These observations are important to the discussion of energetics. In Chapter 4, a potential energy curve for ferroelastic UICs was postulated in which the mother and daughter are separated by a kinetic barrier of substantial magnitude (Figure 4.11). During and following the application of stress, the crystal containing 2% guest impurity produced topographs in which the stressed sectors appeared appreciably deformed. Although plastic daughter domains were noticeable under the microscope, they appear quite distorted in distorted topographs such as Figure 5.3c. Unlike the crystal with 11% monoketone, in which small regions of daughter domain were shown to diffract as single crystals, the fraction of monoketone in this crystal is presumably not great enough to sufficiently facilitate the annealing (or prevention) of stressed defects. Such defects

should make the daughter metastable with respect to the mother, but the barrier between daughter and mother is large enough to prevent pseudoelastic reversion at low impurity concentrations. In the SWBXT experiment, the distortion observed in stressed crystals suggests the nature of these defects involves variations in strain.

In Section 4.3 it was shown that UICs containing mixtures of 2,10-undecanedione and 2-undecanone exhibit a critical impurity concentration for pseudoelasticity. In Figure 5.3, the crystal containing 16% monoketone exhibited spontaneous domain reversion. Although the application of stress distorts the topograph images (for instance, see Figure 5.4b), pseudoelastic reversion after stress release produces topograph images in which much of the deformation has disappeared.

Comparing Figures 5.3c and f, one notes significant differences in the topograph images of the two crystals collected after the release of stress. For the crystal grown from a 98:2 mixture of 2,10-undecanedione and 2-undecanone, a substantial degree of distortion in the topograph images is observed. Apparently, this crystal was irreversibly damaged by the application of stress, and the damage is visible as smeared topograph images. In contrast, application of force to the crystal containing 16% impurity produced only minor distortion of the topograph images following stress release. Here, the mother reflections exhibit their original shapes and most of the same features. This crystal is somehow better able to accommodate the applied stress so that less permanent deformation occurs.

Ferroelastic domain switching provides one avenue by which a solid material can adapt to an externally applied stress because reorientation of strain accompanies the compression. When this occurs, the crystal yields to the stress and reduces the likelihood

of being damaged. By facilitating the process of defect repair, the monoketone impurity should reduce crystal damage resulting from the stress experiment. However, the observable changes in the topographs in all of the crystals following stress and release (regardless of monoketone content) indicates that high concentrations of monoketone do not eliminate these imperfections entirely. Nevertheless, the topographs taken after stress release clearly indicate less deformation in the pseudoelastic 84:16 crystal than in the plastic 98:2 crystal.

Topographs recorded for the crystal containing 11% 2-undecanone (Figure 5.4) present a case between the two extremes. For this crystal, ferroelastic domain switching after the application of a light stress produced X-ray topographs in which only minor distortion was observed. Further compression did yield a small amount of distortion in the images recorded following release, though not nearly as much as in crystals containing less monoketone. The topographs also reveal reflections arising from ferroelastically switched regions; photomicrographs (such as Figure 5.4e) taken following the stress experiment indicate that one of these is oriented differently than expected for a "daughter" domain (discussed below). (The orientation of each domain was confirmed from photomicrographs (not shown) collected at several crystal orientations.) Inasmuch as the formation of stress-induced defects tends to broaden and distort the images, these domains appear to have successfully relaxed (or avoided) stressed defects so that a fairly uniform strain orientation is achieved. Apparently, the incorporation of a moderate amount of 2-undecanone has provided this crystal the capacity to repair stressed defects to a greater degree than for the 98:2 crystal. In terms of the potential energy surface

discussed in Section 4.3.4 (Figure 4.11), this daughter containing greater amounts of monoketone should be lower in energy.

In the crystal containing 16% monoketone, the daughter is presumably capable of repairing stressed defects. As discussed in Chapter 4, the observation of pseudoelasticity indicates a larger decrease in the reversion barrier than in the thermodynamic stability of the daughter, at least for the sites that exhibit the slowest reversion rates. Because it contains less relaxive impurity, the crystal containing 11% monoketone may not be as capable of repairing stressed defects present within the daughter. The inability of these domains to revert to mother suggests that the reversion barrier has not been reduced *enough* for pseudoelastic reversion, as it was for the fully pseudoelastic crystal. Therefore, these daughters are thought to be higher in energy than the mother but *kinetically* stable toward pseudoelastic domain reversion.

5.1.2 Striations in X-Ray Topographs Indicate Nanoscopic Twinning

The observation of defect repair within daughter domains provides important clues concerning the source of the ferroelastic memory effect. However, close examination of X-ray topographs reveals an additional important feature. Many of the topographs exhibit fine stripes that vary in intensity, or *striations*, that span the length of the sector image. This behavior is especially visible in Figure 5.3d; here, the striations run horizontally across the dark image. These striations differ from those observed in undistorted crystals such as 2,12-tridecanedione/urea,[3] which are thought to arise from changes in scattering power between rotational twins that are present.[4] For strained UICs containing 2,10-undecanedione, topograph striations are thought to arise from twinning

as well; however, for these crystals, the distortions that occur at the twin boundaries lead to an additional effect known as *dynamical diffraction contrast*, which is explained below.

Ideally, all diffracting planes in a crystal are exposed to radiation of the same intensity; such behavior is the basis of *kinematical diffraction* theory, which is used in the treatment of X-ray intensities for the purposes of crystal structure determination. However, for a *perfect crystal* in which the diffracting planes are evenly spaced, the incident beam is attenuated as it scatters through successive volumes of the sample. This effect is known as *primary extinction*, and it is especially severe for intense reflections. Many crystals behave as if they diffract kinematically, so Darwin[5] proposed that most crystals are not composed of perfectly spaced planes throughout, but instead contain many small, misaligned regions of perfect planes. For many crystals, these *mosaic blocks* are on the order of tens to hundreds of nanometers in size.[6,7] Primary extinction can occur within these blocks, but this effect is often not severe if the blocks are small enough and/or scattering is weak. Alternatively, diffraction at some mosaic blocks reduces the intensity of exposure for others that possess the same alignment, an effect known as *secondary extinction*.[8-10]

The phenomenon of primary extinction can be treated within the theory of *dynamical diffraction*, which was developed by Ewald,[11] and which takes into account the interactions of the electric fields of the incident and scattered waves. According to this theory, small differences in perfection (such as strain) can give rise to variations in reflection intensity in high resolution topographs.[1] This phenomenon, known as

dynamical diffraction contrast, makes SWBXT exceptionally sensitive to strain and variations in crystal perfection.[12]

Although dynamical diffraction contrast reveals differences in strain between regions of a crystal,[13,14] the structural features that lead to dynamical diffraction contrast in SWBXT images may be much smaller than the striations that appear in the topographs. It is likely that the twins are very small and that each striation results from a combination of twins. (Thus, the number of twins is far greater than the number of striations observable in the topograph images.) Indeed, photomicrographs taken at high magnification of crystals for which striations are readily observed do not exhibit structural features to which the striations may be attributed. Furthermore, twins of micro- or macroscopic size should meet the Bragg condition at different angles so that their reflections (e.g., diffraction of daughter observed in Figure 5.4) would be observed somewhere else in the topograph. If dynamical diffraction contrast is the cause of the observed striations, those striations are most appropriately assigned to twinning that is not observable under the microscope. It is on this basis that submicroscopic (i.e., nanoscopic) twins are thought to exist in ferroelastic UICs.

Submicroscopic twins are thought[15] to exist in lanthanum-doped lead zirconate titanate (PLZT) ceramics, where they give rise to a "diffused phase transition."[16] And so-called "intimate twins," crystallographically distinct regions in which members of one domain are wholly enclosed by members of the other, have been identified in synthetic zeolite ECR-1[17] and in ferroelectric barium titanate oxide.[18] Thus, submicroscopic twinning is a general phenomenon that may be important to many important materials. The observation of ferroelectric distortion and phase transition behavior[19] in perovskite

($PbTiO_3$) films down to three unit cells in thickness concurs with the hypothesis of nanoscopic twinning in ferroelastic UICs: ferroic behavior is possible to very small domain sizes.

If the striations are caused by variations in strain at submicroscopic (nanoscopic) twin boundaries, what is the nature of the twinning? Figure 5.5 illustrates some examples where the striations are particularly enhanced within a crystal. In each case the striations exhibit well-defined orientations within the sectors, which indicates that the twin boundaries are oriented in a systematic fashion. Although nanoscopic twins should be present in several orientations, it is those that are aligned along the **g** vector that exhibit the greatest diffraction contrast and are therefore observed in the topograph images.[2]

Just as for macroscopic twins in ferroelastic urea inclusion compounds, nanoscopic twins should be subject to the constraints of strain epitaxy along domain walls, so this is assumed throughout this section. (Refer to Section 4.2.4 for a discussion of strain epitaxy.) Thus, there are only a handful of "allowed" twin boundaries for nanoscopic twinning, and it is those that are aligned nearest the **g** vector that are typically observed in an X-ray topograph. For example, the topograph image in Figure 5.5b is a (110) reflection in which the projection of the **g** vector is parallel to [310]; here, the striations from {130}{130} twins that run along this direction appear more intense than in the topograph image where the **g** vector and nanoscopic twin boundaries are further from parallel (Figure 5.5a).

Figure 5.5c depicts some of the possible orientations of twins for which strain epitaxy is preserved at the domain wall. As discussed in Section 4.2.4, strain epitaxy is possible for rotational twins that are joined along only a few orientations, and these are

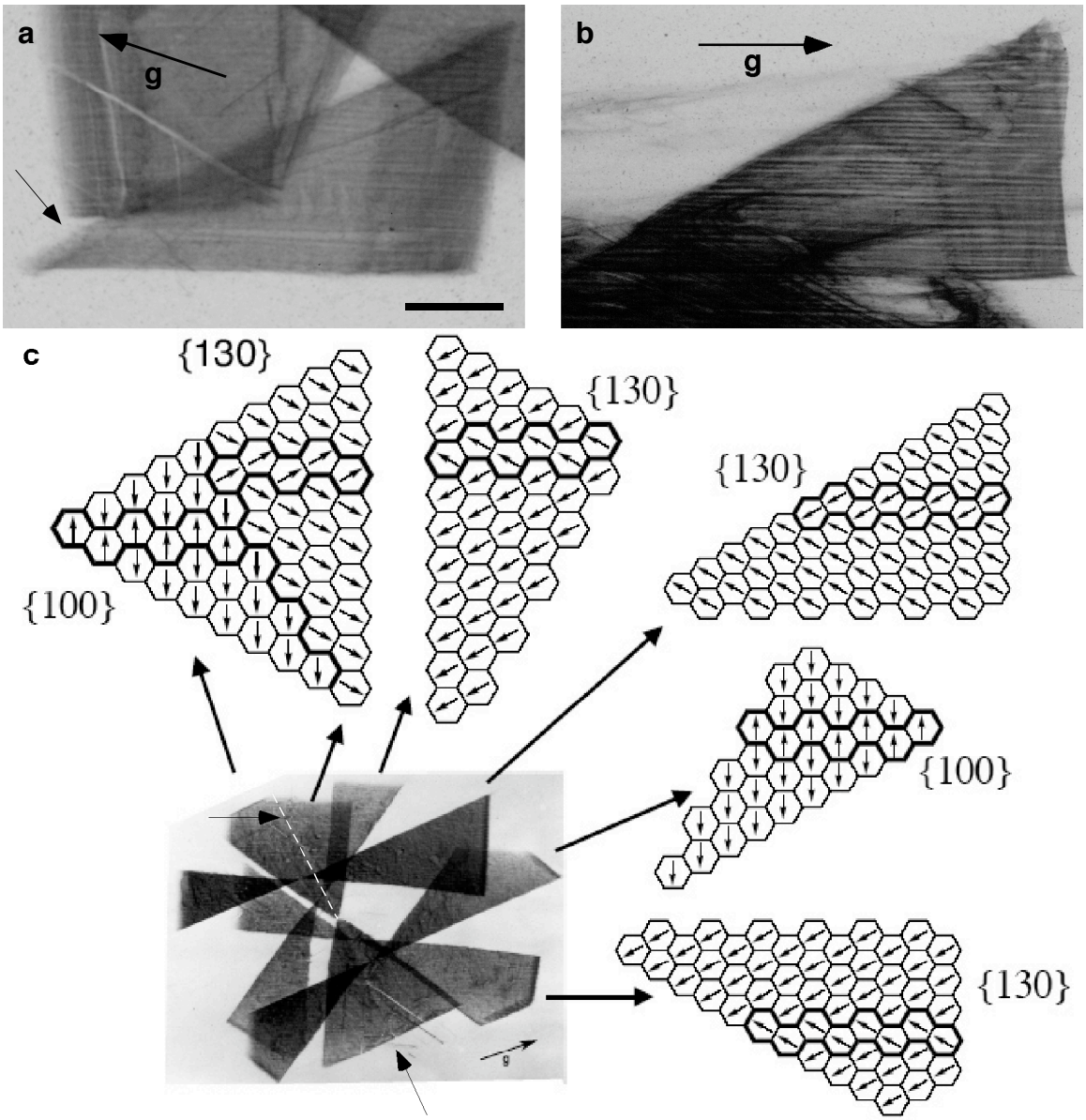

Figure 5.5 Striations in X-ray topographs caused by dynamical diffraction contrast. **(a,b)** Transmission mode SWBXT images of the unstressed UIC, containing an 84:16 mixture of 2,10-undecanedione and 2-undecanone (from Figure 5.3). Although many domain wall orientations are possible, the alignment of the **g** vector determines the most intense striation for each sector. **(a)** A close-up of the $(\bar{2}43)$ reflection. This reflection is located at the center of Figure 5.3d. Scale bar (on the topograph film) = 0.5 mm. **(b)** The same sector, reflection (110), from the same topograph presented in **a**. For both **a** and **b** the striations suggest twinning along the horizontal. However, in **b**, the twins are oriented nearly parallel to the projection of the **g** vector, and the strain contrast is enhanced. **(c)** Topograph image from the unstressed crystal grown from a solution containing 98% 2,10-undecanedione, as described in Figure 5.3. For each sector, the schematic diagrams depict the nanoscopic twinning proposed to give rise to dynamical diffraction contrast. The arrow in **a** denotes rounded reflection edges that are seen near the crystal nucleus; arrows in **c** denote {130}{130} boundaries between rotational twins whose reflections are coincident. (One of these is denoted using a dashed line.) Images **a** and **c** and caption adapted from Hollingsworth, *et al.*, *Cryst. Growth Des.*, **5**, 2100-2116, (2005). These topographs were collected by Hollingsworth, Peterson, Dudley, Raghothamachar and Dhanaraj.

favored over twin boundaries that do not preserve epitaxy. For example, many twin boundaries run along [310] and join neighboring twins at a {130}{130} boundary. However, for the twin boundary that runs along [010], a boundary between {100} faces results. This type of twin boundary lies approximately perpendicular to the strain from each twin; because the slow axis orientation is equivalent for the neighboring domains, these domains exhibit the same slow axis orientation. Between twins joined along a {100}{100} boundary there should be a shift toward hexagonal symmetry caused by the loss of hydrogen bonding. As discussed in Section 4.2.4, this should be observable in birefringence images such as those presented in Figure 4.5. However, the variation in strain that should occur at such a boundary also makes it detectable using X-ray topography.[2] Although there are other twins possible in each of the topograph images, the diffraction contrast is strongest for those observed.

Summing up all of the images in Figure 5.5c, each sector can possess up to three distinct orientation states that are related to one another by rotations of approximately 60°. An unstressed crystal consists of mother domain; depending on the orientation of the applied stress, the daughter domain can exist in either of the two remaining orientations. The third orientation should be epitaxially matched with the mother and daughter domains along {130}{130} or {110}{110} boundaries. Just as twins of mother and daughter are observed to grow spontaneously, the possibility of a third orientation state is suggested by Aizu's ferroelastic species[20,21] 622F222 (see Chapter 3). As described in the following section, nanoscopic twins of the third orientation state are thought to be crucial to the discussion of ferroelasticity in urea inclusion compounds.

One additional feature can be observed in the X-ray topographs. In Figure 5.5a, the top edge of the reflection image appears to curve as it nears the crystal nucleus (see the small arrow). This behavior is observable in some of the domains depicted in Figure 5.5c, as well. Furthermore, for pairs of twins in Figure 5.5c, the reflection intensity disappears at the location of the nucleus. As discussed in Section 4.2.4 (see Figure 4.5), the crystal nucleus is a site at which multiple rotational twins are joined; it is reasonable that crystalline order is reduced and the unit cell constants shift toward hexagonal metric symmetry near this intersection. Because X-ray topography is a diffraction technique, changes in unit cell constants should give rise to shifts in the Bragg angle and lead to the disappearance of the crystal nucleus (and regions near it) in the topographs. In a similar fashion, for adjacent rotational twins whose topograph images appear paired (see the light arrows in Figure 5.5c), the domain boundary can be discerned as a slight change in reflection intensity. This change in reflection intensity suggests that variations in strain produce diffraction contrast along this boundary. Both features are consistent with reduced strain and order that are thought to be present at domain walls.

5.1.3 Nanoscopic Twins Influence Ferroelastic Behavior

Section 5.1.1 illustrated the utility of SWBXT for probing variations in strain within ferroelastic UICs. For experiments in which crystals were analyzed with SWBXT while under stress, Dr. Matthew Peterson observed that a second type of stress-induced domain could be observed in addition to the daughter that intersects the mother along a {110}{110} face. Unlike the daughter, which intersects the growth face at an angle of approximately 60° (Figure 5.4f), this new domain runs nearly perpendicular to the growth

face, and its slow axis orientation is that of neither daughter nor mother, but is rotated by 60° from both. Thus, this domain exhibits the third orientation state predicted for this ferroelastic species (Section 5.1.2). For the following discussion it is instructive to consider the stress-topography experiment for the 89:11 crystal (Figure 5.4).

The mother domain described in Figure 5.4f is oriented with its distortion (*a* axis) approximately 30° CCW from horizontal. (As discussed above, the orientation of each domain was confirmed from photomicrographs (not shown) collected at several crystal orientations after the topograph experiment.) As compressive stress was applied along the horizontal direction, ferroelastic domain switching transformed portions of the mother domain into daughter domain via ~60° CCW rotation of the ferroelastic strain. In this fashion, the strain of the daughter became aligned vertically, *i.e.*, perpendicular to the applied stress. For the third orientation state, which is oriented ~60° from both the mother and the daughter, the strain must be oriented 30° CW from horizontal. Therefore, although domains of the third orientation state are epitaxially matched with surrounding mother domain (they border at {130}{130} boundaries), they are degenerate with the mother with respect to the applied stress and are therefore anomalous. Nevertheless, the coincidence in orientations of the anomalous domains (Figure 5.4e-g) and the nanoscopic twins observed in the unstressed sector (Figure 5.4a) suggests they may possess the same domain orientation. It is therefore postulated that these twins arose from growth of nanoscopic twins during the stress experiment.

How do the anomalous domains grow? Striations in topographs of unstressed crystals indicate the presence of nanoscopic twins *before* ferroelastic reorientation. Only once the crystal in Figure 5.4 is stressed and released do the anomalous domains become

observable under the microscope. This suggests that the stress experiment has increased the size of the nanoscopic twins so that they become visible under the microscope. Although they are thought to be epitaxially matched with the mother, nanoscopic twins should be mismatched with daughter domains (see Figure 5.4f). Because of their appreciable surface area in comparison to their volume; strain mismatch should make smaller twins less stable in comparison to larger twins (whose volume is larger in comparison to their surface area). Stability should therefore be increased through growth of these domains.

The observation of nanoscopic twins in ferroelastic UICs is important because it provides a possible mechanism for the production of the stressed defects that are thought to be responsible for spontaneous ferroelastic domain reversion. If the nanoscopic twins are indeed epitaxially matched with the mother domains that surround them, they cannot at the same time be epitaxially matched with daughter domains created in a stress experiment. In Section 4.2.4, strain mismatch was demonstrated to drive domain reorientation in a growing crystal of 2,10-undecanedione/urea; it could also be responsible for the difference in energy between the mother and daughter that gives rise to pseudoelastic domain reversion. If so, then the process of annealing the daughter might involve the establishment of strain epitaxy between the nanoscopic twins and the daughter, which should reduce the energetic advantage of domain reversion and effectively "erase" the memory. This idea will be more fully developed in the sections that follow.

The idea that crystalline ordering can drive pseudoelastic reorientation is not unique to urea inclusion compounds. As discussed in Section 1.2, the "rubber-like"

behavior observed in certain metal alloys is thought to depend on the symmetry relationships between the parent phase and point defects.[22-25] After a paraelastic crystal is cooled through the martensitic phase transition, point defects within the parent adopt the symmetry of their surroundings through annealing processes. When this material is deformed, those point defects become incompatible with the symmetry of the new phase and therefore provide a bias for reversion to the parent domain. By allowing the symmetry of point defects to adopt that of the surrounding parent phase, annealing the daughter phase at ambient temperature can erase the rubber-like memory effect.[26,27]

The following sections describe experiments conducted to test the hypothesis that strain mismatch between nanoscopic domains and their surroundings is, in fact, one kind of stressed defect that is responsible for spontaneous domain reversion in ferroelastic UICs. Like the work done on rubber-like alloys, the studies described here reveal fine subtleties about the nature of this phenomenon and provide us with a clear picture of ferroelasticity in UICs.

5.2 Confirming the Existence of Nanoscopic Twins

The observation of nanoscopic twinning in ferroelastic UICs and their hypothetical involvement in the domain switching process raises many questions about the nature of this process. These include:

1) Are nanoscopic domains detectable by other means?
2) What effect does acoustomechanical treatment have on nanoscopic twins?
3) How do nanoscopic domains contribute to ferroelastic behavior?

The sections that follow describe work aimed at answering these (and other) questions.

5.2.1 *In Situ* Stress Diffraction Experiments Reveal the Third Domain Orientation

The previous discussion on nanoscopic twinning in ferroelastic urea inclusion compounds assumes that strain epitaxy between the nanoscopic twin and its surroundings is achieved. The symmetry of the orthorhombic channel limits the number of possible orientations for epitaxially matched rotational twins so that they may possess one of three orientations: mother, daughter, and a third orientation; these are related to one another by approximately 60° rotations about the channel axis. This section discusses an experiment in which the diffraction pattern and photomicrographs of a stressed crystal are collected in tandem. The findings of this experiment, combined with the optical observation of anomalous domains in the SWBXT experiments above, have provided a leap in the understanding of the ferroelastic memory effect exhibited by urea inclusion compounds.

The *in situ* stress diffraction experiment involves the compression of a crystal that is mounted onto an X-ray goniometer head. In total, there were three experiments of this kind performed with the device described in Figure 4.7. The crystal is glued to one of the nylon stress bars, and stress is applied using an actuator controlled by a thumbscrew. The precision with which strain can be applied with this device is quite limited; as constructed, the thumbscrew provides an estimated strain precision of no better than 5 μm.[28] For the first crystal stressed in this manner, L_0 was estimated to be 830 μm; thus, the strain values presented in that case are accurate only to about 0.6%.[29]

This *in situ* experiment was performed on the Bruker SMART1000/P4 single crystal diffractometer at Kansas State University. In this experiment, the crystal was subjected to X-rays in a direction nearly parallel to [001] (the channel axis). This arrangement allows the observation of orientation states that are rotated about the [001]

axis. X-ray rotation frames consisted of 6° rotations about the ϕ axis, which is oriented perpendicular to the channel axis, over the duration of 30 seconds. (The collection of a series of 0.2° frames confirmed the reflections of interest to be included entirely within the range of the 6° ϕ rotation.[30]) In addition, an optical camera equipped with nearly crossed polarizers and light source was installed so that optical photos could be used to monitor the crystal. (Despite considerable effort, it was not possible to perfectly cross the polarizers, which were placed on either side of the crystal using ring stands and clamps. Colors due to slightly uncrossed polarizers are clearly observable in the photomicrographs of Figure 5.7.) The photos obtained provide an important comparison with the X-ray data collected through the course of the stress experiment.

The fragment used was cleaved[31] from a larger crystal that was grown in a slowly cooled solution containing 2.5 M urea and a 90:10 mixture of 2,10-undecanedione and 2-undecanone.[32] This fragment was 990 μm across at zero strain, and was 520 μm thick. These dimensions are larger than the 500 μm collimated cross section of the incident X-rays; however, by using a thick crystal (which is more resistant to breakage) the presence of weak reflections was more easily observed. (The use of a large crystal reduces the reliability in the measured reflection intensities. For this experiment, the lattice constants and orientations, which are affected much less by inconsistencies in the irradiated volume of the sample, are reliable.)

The experimental setup is diagrammed in Figure 5.6d. At this crystal orientation, the X-ray source is located above the page (behind the viewer), and the detector is located 5 cm behind it (at 10° in 2θ). As stress was applied, an optical photograph was taken, followed by the 6°, 30 s, ϕ rotation frame. (The initial goniometer settings for the

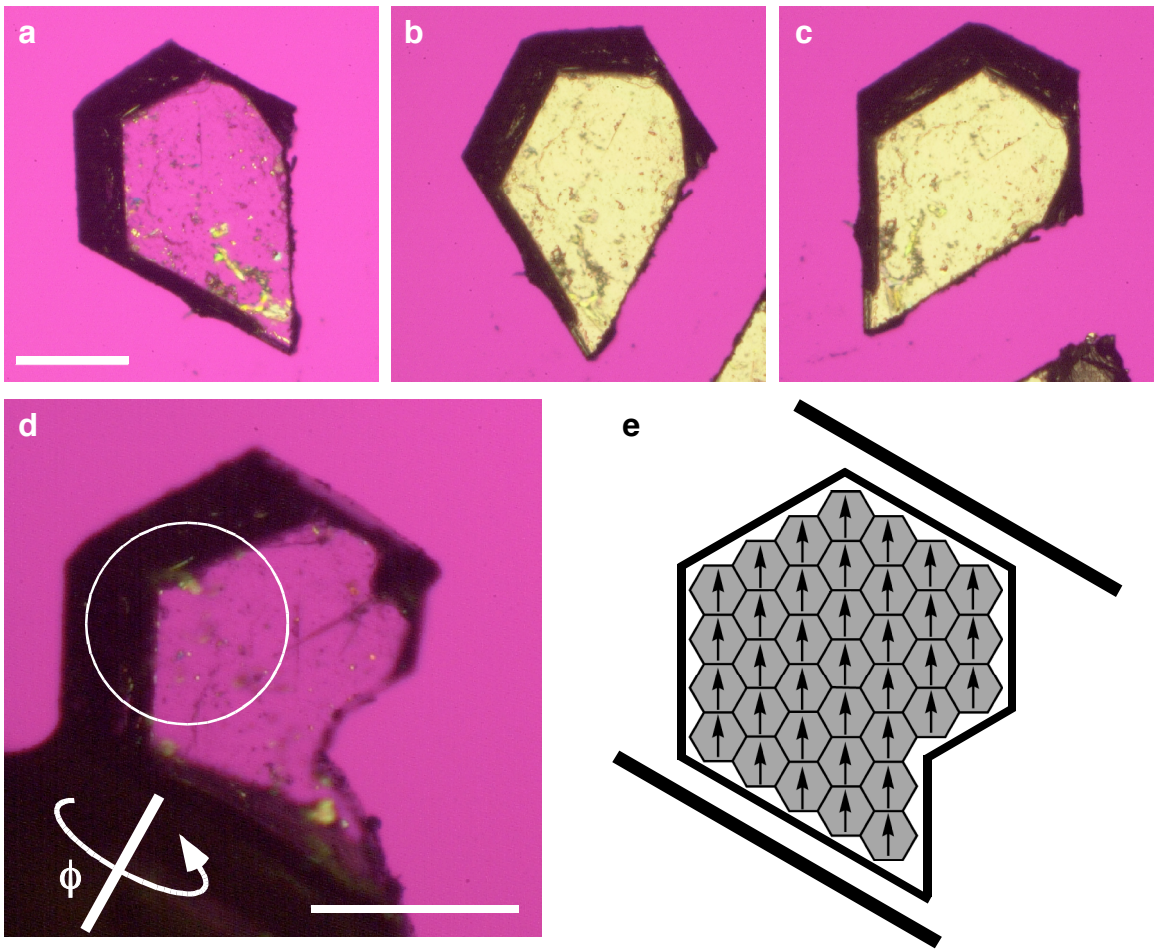

Figure 5.6 The first *in situ* stress-diffraction experiment. **(a-c)** Photomicrographs of the crystal taken between crossed polars and with λ plate, viewed along [001]. This fragment was cut from a larger portion that contained rotational twins. Scale bar = 0.50 mm (Nikon 1.3x). **(a)** 0° stage rotation. **(b)** 30° CW stage rotation. **(c)** 60° CW stage rotation. These photos demonstrate the presence of a single mother domain. **(d)** The crystal, mounted to the stress goniometer pin with a small amount of epoxy adhesive. Initially, the crystal was attached to the nylon pin in the wrong orientation. The removal and remounting of this crystal caused the damage and small crack towards the right of the crystal. The approximate location of the incident X-rays (0.50 mm collimation) is indicated by the white circle. Rotation images were collected by rotating the crystal about the ϕ axis (shown here). Scale bar = 0.50 mm (Nikon 1.3x). **(e)** Schematic diagram illustrating the unstressed crystal. In this orientation and in **a** and **d**, $[100]_{mother}$ is oriented vertically, and the mother is extinguished. Stress applied by the black stress bars produces a daughter in which the slow axis has rotated 60° CCW away from the extinguishing position.

rotation images were $2\theta = 10°$, $\omega = 0°$, $\phi = 56°$, $\chi = -29$. During this collection, ϕ ranged from 56° to 62° over the 30 second period.[33]) An example of a rotation image is provided in Figure 5.7a. In this image, the diamond-like array of reflections indicates a lattice with approximate C-centering. (As discussed in Section 2.2.4.1, the incorporation of 2-undecanone reduces the lattice symmetry of this crystal from $C222_1$ to some other lower symmetry, possibly P1. Nevertheless, within the limits of detection, the diffraction pattern appears to exhibit C-centered orthorhombic symmetry.) The orientation matrix provides a unit cell orientation consistent with the extinguished mother domain observed in Figure 5.6: $[100]_{mother}$ is oriented vertically, and $[010]_{mother}$ is oriented horizontally. Unfortunately, for a C-centered crystal with *nearly* hexagonal dimensions, 60° rotational twins (e.g., orientation states such as mother and daughter) are not distinguishable with Mo radiation at low h and k indices. This is explained graphically in Figure 5.8. However, for higher reflection indices, reflections from 60° rotational twins diverge, and the mother, daughter and the anomalous twin are all observable.

The stress diffraction experiment is summarized in Figure 5.7. For each step of the experiment, an X-ray rotation image, optical photomicrograph and line profile plot of three sets of reflections are provided (Figure 5.7a-c, respectively). Stress and strain values are provided as well. In this experiment, the stress bar was moved while the crystal was in position for rotation image collection. Rotation of the crystal into position for collection of the photomicrograph ($2\theta = 10°$, $\omega = 0°$, $\phi = 124°$, $\chi = -29°$) required rotation about ϕ from 62°, the ending value for rotation image collection, to 124°.[33] As the upper stress bar changes orientation with respect to the ground, mechanical play in the device allows some shifting of mass and the applied stress is reduced. As

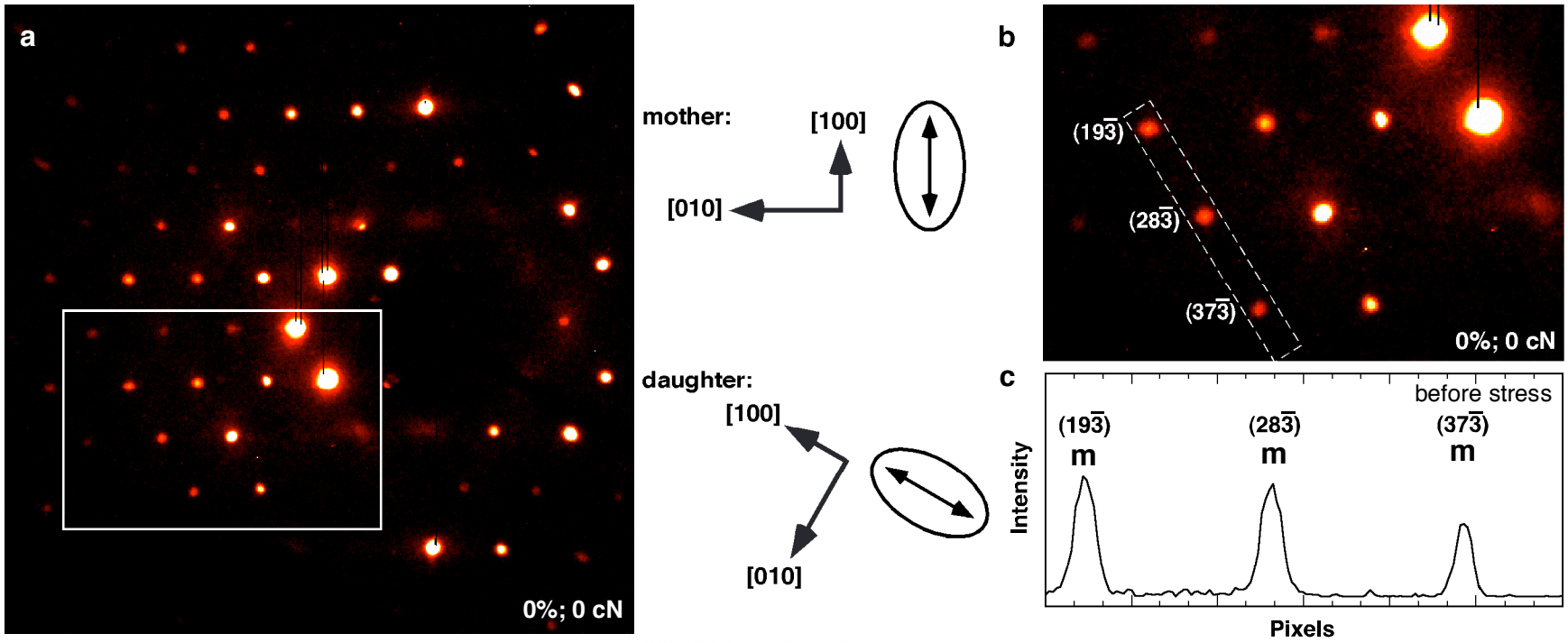

Figure 5.7 The *in situ* stress diffraction experiment described in Figure 5.6. In this experiment, X-ray rotation images and optical photomicrographs were collected as the crystal was stressed. The rotation images were collected over 30 sec, 6° rotations about ϕ (see Figure 5.6d); the optical photomicrographs were taken between crossed polars. **(a)** The rotation image obtained at the point of first contact (L_0; 0% strain, 0 cN applied force). Here, the reflections observed are due to the original mother domain. The orientation of the unit cell and optical slow axis for the mother and daughter are depicted in the diagram at right. In the rotation image, the diamondlike pattern in the reflections indicates the expected C-centered lattice. For compressive stress applied ~30° clockwise from vertical (along $[31\bar{0}]_{mother}$), domain reorientation will produce a daughter domain with strain (and [100]) aligned ~30° from the horizontal. **(b)** A close-up view of the portion of the rotation image outlined in **a**. Plot profile analysis was performed for the three indexed reflections. The box outlines the area of analysis. **(c)** Plot profile for the three reflections indicated in **b**. Similar profile analyses were performed for each rotation image collected in the experiment. Here, reflection intensity is plotted vs. pixels, or position within the linear sample region.

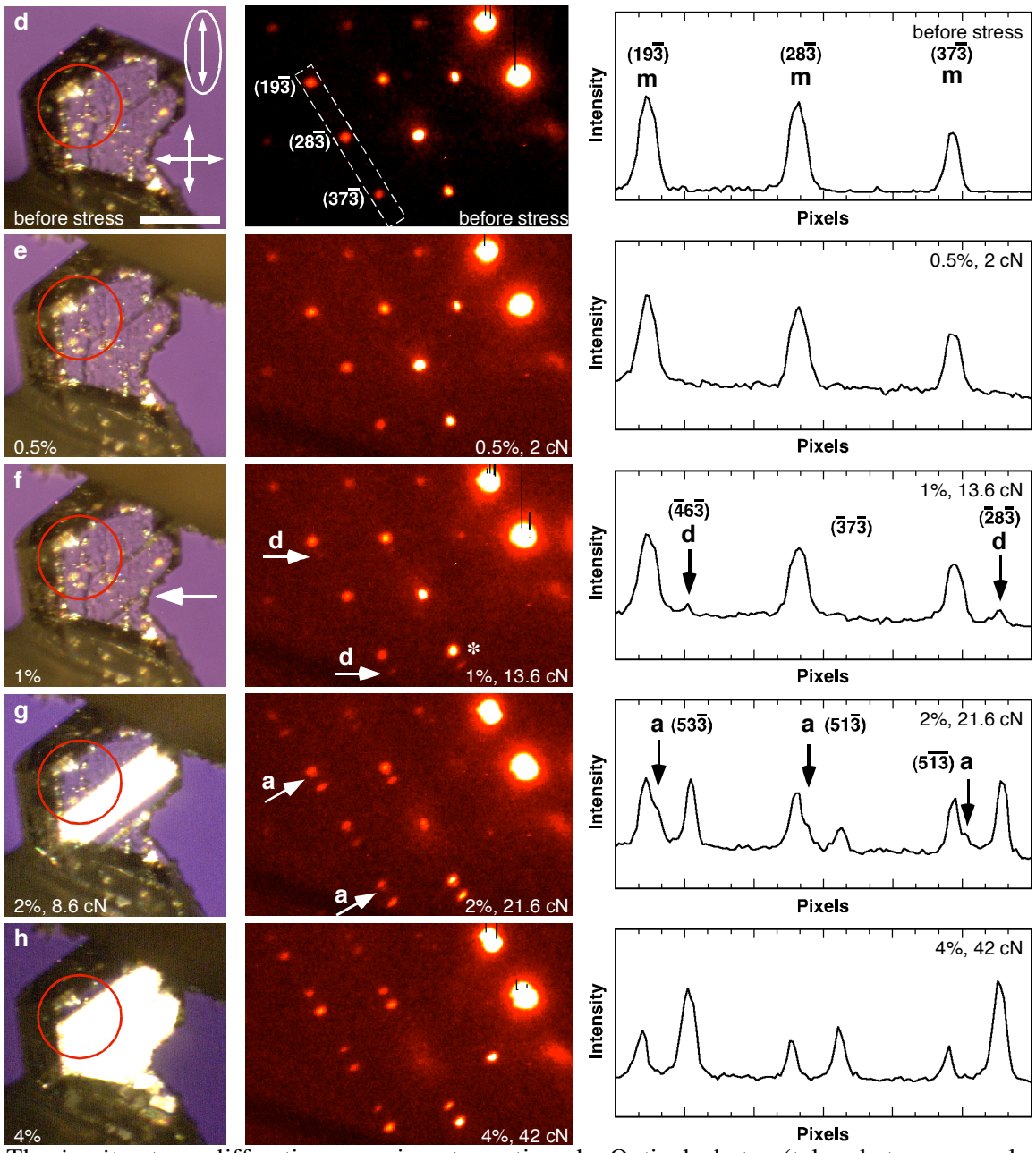

The *in situ* stress diffraction experiment, continued. Optical photos (taken between nearly crossed polars oriented according to the crossed arrows) and 6° ϕ rotation images were collected in sequence during the stress experiment. (The approximate location of the X-ray beam in each photograph is indicated by the red circle.) The line profile plots are all drawn using the same scale. In **d**, the optical photomicrograph reveals a mother domain of uniform slow axis orientation (represented by the double-headed arrow). The rotation image collected at this time exhibits one set of reflections with [100] aligned vertically (orientation depicted in **a**). At 1% strain (**f**), reflections from the daughter domain emerge (see arrows labelled "d" in **f**). At this time, a small daughter domain is observed that lies *outside* of the region of X-ray incidence; this is denoted by the arrow in the photomicrograph. (See **z** for a close-up image.) By 2% strain (**g**) the daughter has grown in size so that its reflection intensity rivals that of the mother. In addition, shoulders appear on the "mother" reflections; the presence of these is discernible in the plot profile for this rotation image (see arrows). The shoulders are attributed to the presence of the domain orientation, labelled "a" for "anomalous." The reflection indices from the unit cell determination of each lattice (see text) are provided in the line profiles. Scale bar (in **d**) = 0.50 mm.

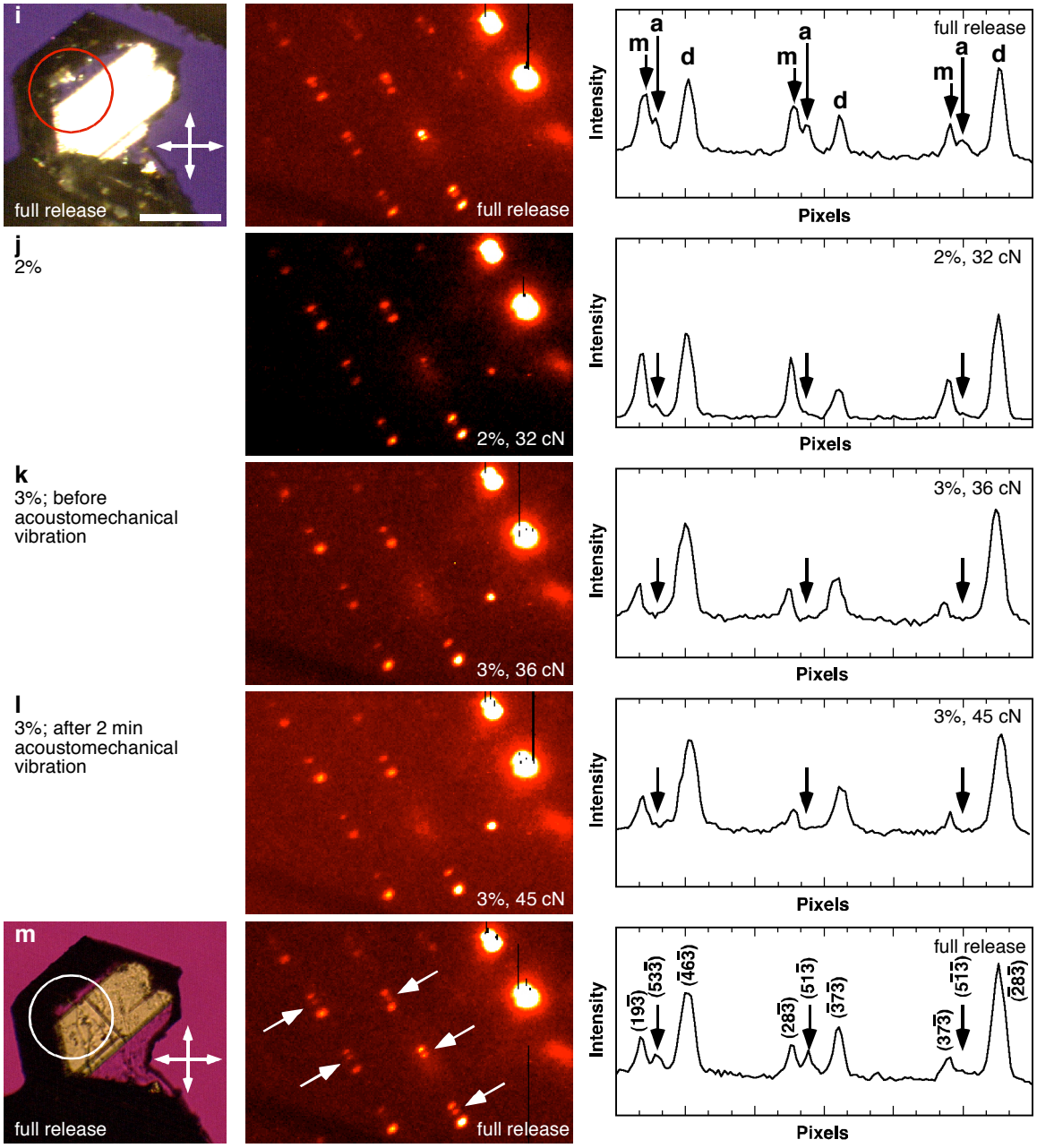

The *in situ* stress-strain experiment, continued. In **i**, the stress has been released from a maximum crystal strain of 4% (**h**, previous page). Here, the optical photomicrograph reveals a plastic response. The rotation image (and line profile plot) indicate the presence of all three orientation states. (Reflections from these domains (mother, daughter and third orientation state) are denoted m, d, and a, respectively.) As stress is again applied, the intensity of the daughter grows at the expense of intensity from the other two orientations. By 3% strain (**k**), reflection intensity from the third orientation state is reduced substantially. Acoustomechanical vibration was applied for 2 minutes at 3% strain, between images **k** and **l**. Rotation photos **k** and **l** are very similar, even though the applied force has increased. **(m)** Following stress release. This optical photograph utilized a λ plate (slow axis oriented 45° from the polarizers along the axis connecting NW to SE). In the rotation image, all three orientations are observed. Reflections from the third domain orientation are indicated by the arrows. Scale bar (in **i**) = 0.50 mm.

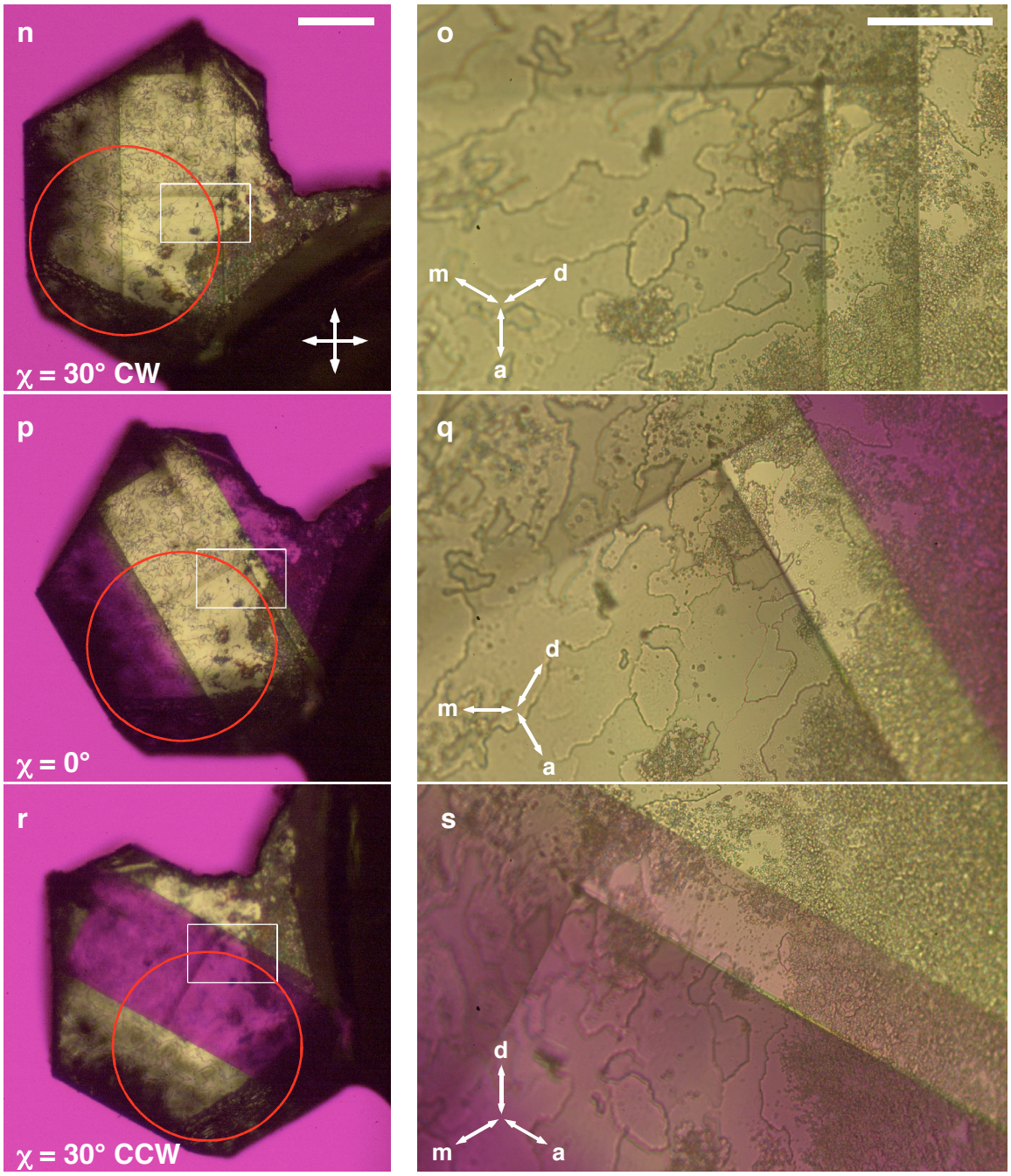

Photomicrographs taken between crossed polars and with λ plate following the *in situ* stress experiment. In these photos, the crystal is aligned on a microscope-mounted goniometer so that [001] is perpendicular to the page. **(n,p,r)** Low magnification photos illustrate the extinguishing position of the macroscopic mother and daughter domains. Here, small domain stripes with ~90° boundaries are observable. It was considered possible that these domains might contribute to the reflection intensity of the third orientation state. The red circles point out the estimated location of the X-ray beam. Scale bar = 200 μm (Nikon 5x). **(o,q,s)** High magnification photos corresponding to regions outlined in **n**, **p** and **r**. The regions photographed were chosen because the suspect domains were most visible here (see text). Slow axis orientation for mother (m), daughter (d) and anomalous orientation (a) are designated by the arrows. Scale bar = 50 μm (Nikon 40x). These photos illustrate that the domain stripes in this crystal are oriented as the mother domain (they are extinguished in **q**) and are from neither the third orientation (**o**) nor daughter (**s**). The average thickness for all three domain stripes is estimated at 1.4 ± 0.1 μm.

(t) Data for the three unit cells identified from the data set collection performed following *in situ* stress-diffraction. See text for details.

			anomalous domain		
	mother	**daughter**	**experimental**	**derived 1**	**derived 2**
cell axes (Å)					
a	8.340 (2)	8.3164 (12)	8.341 (3)	8.341 (3)	8.341 (3)
b	13.963 (5)	13.918 (4)	13.961 (3)	13.963 (4)	13.963 (4)
c	32.980 (10)	32.897 (5)	32.980 (11)	32.978 (8)	32.978 (8)
Eulerian angles (deg)					
1	–26.225	–26.178	–26.135	–26.225	–26.225
2	93.268	93.234	93.081	93.268	93.268
3	–59.134	2.404	60.194	–118.234	–120.929
reflections					
total	248	536	27		
unique	165	226	20		

(u,v,w) Gaussian peak fitting of the three groups of reflections outlined in **m**. See text for details.

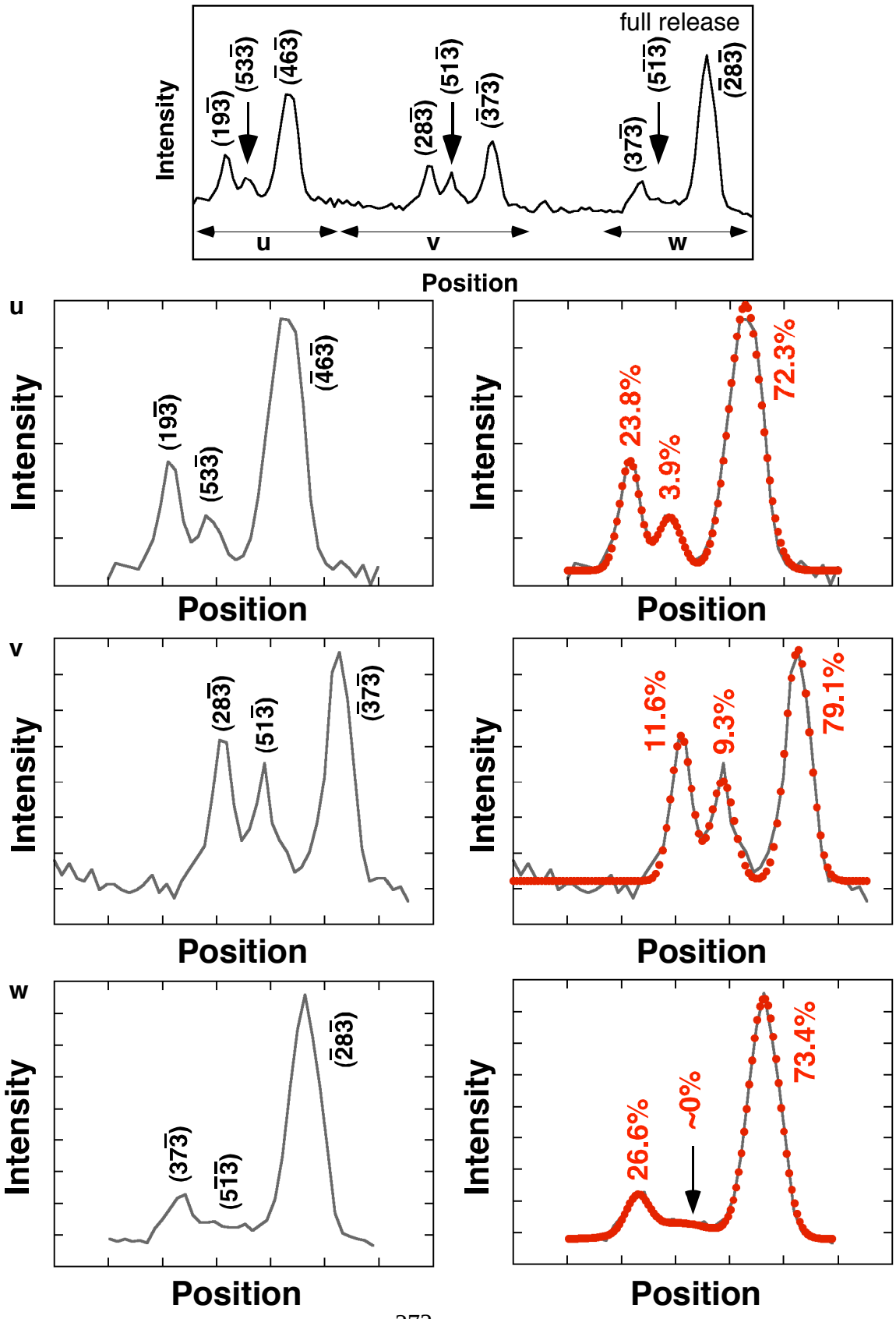

x

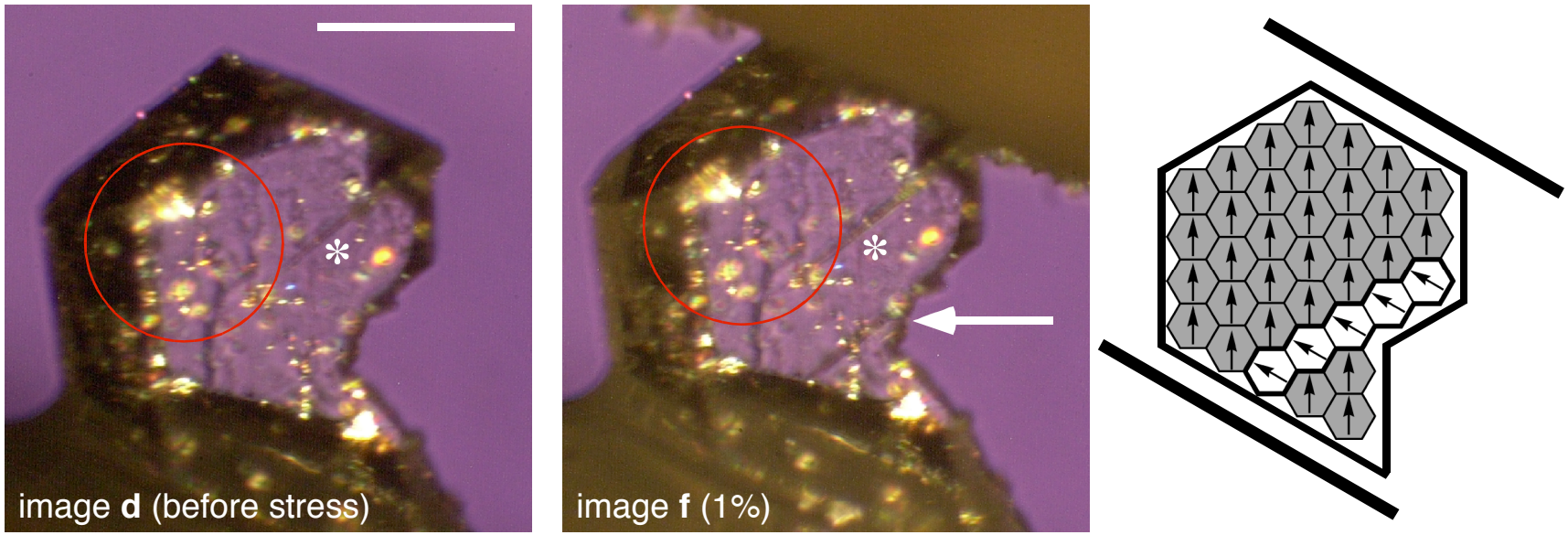

(x) Close-up images of photomicrographs **d** and **f**. A crack spreading from the upper face of the crystal (see *) is visible throughout the experiment. At 1% strain, the first daughter domain to be observed optically (see arrow) is approximately 0.2 mm from the region of X-ray incidence. The schematic at right illustrates the daughter domain borders the mother at {110}{110} boundaries. This geometry is preserved at higher strains (e.g., Figure 5.7g, h, i). Scale bar = 0.50 mm.

(y,z,aa) Data for fitted peaks (from Figure 5.7m) shown in **u**, **v** and **w**, respectively. The last column provides relative areas for the reflections in each group, which are based on the scaled intensities. In **ab**, the mean scaled intensity (multiplied by a factor of 10,000) for each domain is tabulated; these data can be used to compare reflection intensities between groups (see text). Here, mother and daughter areas were averaged from three reflections whose intensities are provided in **y**, **z** and **aa**; the area of the anomalous domain was determined from the average of two reflections whose intensities are provided in **y** and **z**.

y

		Gaussian peak fitting				intensity, scaled	
peak	**index**	**area**	**center**	**width**	**$(10Fc)^2$**	**(area/$(10Fc)^2$, × 10^4)**	**area (%)**
mother	(1 9 $\bar{3}$)	1.091	0.11476	0.037707	1296	8.418	23.8
anomalous	(5 3 $\bar{3}$)	0.6179	0.18823	0.043902	4476	1.381	3.9
daughter	($\bar{4}$ 6 $\bar{3}$)	4.2932	0.32862	0.061236	1681	25.54	72.3

z

		Gaussian peak fitting				intensity, scaled	
peak	**index**	**area**	**center**	**width**	**$(10Fc)^2$**	**(area/$(10Fc)^2$, × 10^4)**	**area (%)**
mother	(2 8 $\bar{3}$)	0.64058	0.8093	0.030656	1197	5.352	11.6
hump		1.0591	0.86531	0.11898			
anomalous	(5 1 $\bar{3}$)	0.24815	0.88768	0.01964	576	4.31	9.3
daughter	($\bar{3}$ 7 $\bar{3}$)	1.8361	1.0267	0.04479	502	36.6	79.1

aa

		Gaussian peak fitting				intensity, scaled	
peak	**index**	**area**	**center**	**width**	**$(10Fc)^2$**	**(area/$(10Fc)^2$, × 10^4)**	**area (%)**
mother	(3 7 $\bar{3}$)	0.801	1.5361	0.053646	502	16.0	26.6
anomalous	(5 $\bar{1}$ 3)				576		
daughter	($\bar{2}$ 8 $\bar{3}$)	5.2815	1.7634	0.056627	1197	44.12	73.4

ab

domain	**mean scaled intensity (× 10^4)**
mother	9.91
anomalous	2.84
daughter	35.4

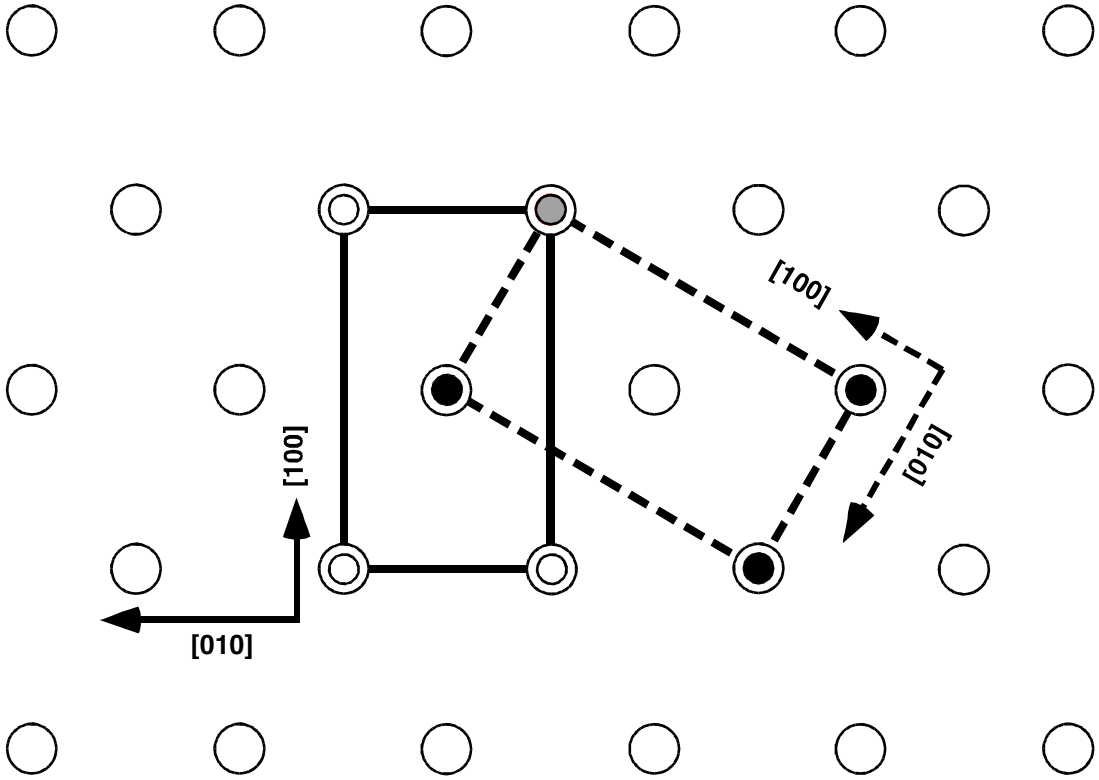

Figure 5.8 The reciprocal lattice for a C-centered orthorhombic crystal, viewed parallel to [001]. The reciprocal lattice for the mother domain (whose orientation is known) is found by connecting (a*b*) reflections and is represented by the solid lines. (The unit cell axes are drawn in direct space to the left). For 2,10-undecanedione/urea (and mixtures of this guest and 2-undecanone), the ferroelastic strain runs parallel to [100]. Ferroelastic switching involves the generation of a cell that is crystallographically identical to the mother but which is rotated by approximately 60°. The application of stress along [3$\bar{1}$0] will produce a daughter whose reciprocal lattice is denoted by the dashed rectangle and whose whose strain is perpendicular to the applied force. The dashed arrows, at right, denote the unit cell axes for this cell. Because the crystal is distorted only 3.7% from hexagonal symmetry and is C-centered, reflections from daughter and mother are indistinguishable at low reflection angles. At higher indices (a + b), the reflections diverge so that the reflections can be resolved.

demonstrated in the second stress-diffraction experiment, this effect can be appreciable so that stress values recorded during rotation image collection are larger than for the photomicrographs. When known, stress data recorded during collection of the photomicrographs are provided.[34]

At low strains, reflections due to the mother domain were observed exclusively. The lattice constants and unit cell orientation for this domain were determined from a full data set collected following the stress experiment (discussed below). The identification of the mother domain orientation is important because it can be compared with the orientations of other domains created during the experiment.

As stress is applied to this crystal, several important events transpire. After stressing from 0.5 to 1% strain, the daughter domain is observable in the rotation image and line profile plot (Figure 5.7f). (For comparison, each of the line profile plots in Figure 5.7 is drawn using the same, arbitrary, scale.) In the optical photomicrograph, no observable change has occurred in the region on which the X-ray beam is incident. (See red circle in each photomicrograph. The location of the 0.5 mm X-ray beam is known with an (estimated) accuracy of 0.1 mm. Its position was estimated[35] by noting the position of crystal landmarks when viewed through the goniometer-mounted telescope. However, any misalignment of the telescope would contribute to the error in the beam position.) However, on the right of the crystal a small stripe is observed (arrow in Figure 5.7f). Since this stripe lies approximately 0.2 mm from the edge of the beam, it is not thought to contribute to the observed reflections. An enlarged version of the photomicrograph in Figure 5.7f is found in Figure 5.7x. Here, the region of X-ray incidence appears free of daughter domains. (The apparent daughter domain in Figure

5.7f (x) is actually a crack; see asterisk in Figure 5.7x.) As discussed above, the act of rotating the crystal into position for the X-ray rotation image can lead to a shift in the applied stress. However, this effect is thought to be small enough that it did not inadvertently induce large-scale domain reorientation.

Continuing with the stress experiment, by 2% strain (Figure 5.7g), the daughter domain has grown in size so that its reflection intensity compares to that of the mother. Optical photos taken at this strain reveal that an appreciable fraction of the crystal has undergone domain switching.

At 2% strain an additional feature of ferroelasticity is observed. In the rotation image (Figure 5.7g), small shoulders can be seen on the reflections from the mother domain, and the line profiles confirm their presence. In Figure 5.7g, these are indicated by the arrows. (Below, it is demonstrated that these reflections belong to the third orientation state. In the figures, they are labeled a, for "anomalous.") By 4% strain, the shoulders have disappeared (Figure 5.7h). At this maximum strain, the area of X-ray incidence consists primarily of daughter domain so that its intensities are greater than those of the mother.

Figure 5.7i-m illustrates the second portion of this experiment. Following compression to 4%, the stress was removed; the images and plot profiles in Figure 5.7i demonstrate some relaxation, but this crystal exhibited primarily a plastic response. The rotation image collected following stress release reveals appreciable intensity from all three orientation states (m, a and d). Although it disappeared between 2 and 4% strain, reflection intensity from the anomalous domain is again visible after the stress has been released.

Figure 5.7j-l describe an attempt to observe the effects of increased stress and acoustomechanical vibration. As compressive stress was reapplied to the crystal, reflection intensity from the daughter appears to increase at the expense of the other domains. This time, the crystal was stressed to 3% strain (Figure 5.7k), and acoustomechanical vibration was applied for 2 minutes. (Here, the same 4.1 kHz piezoelectric transducer discussed in Section 4.3.4 was glued to the nylon goniometer 1 cm below the crystal. It was oriented so that the vibration was emitted along [001]; the applied voltage was 12.0 V.) Immediately following this acoustomechanical treatment and before stress release, a second rotation image was collected (Figure 5.7l). The plot profile collected following stress release is provided in Figure 5.7m. A comparison of this profile with the one collected following the first cycle of stress and release (and without acoustomechanical treatment) (Figure 5.7i) suggests an increase in relative reflection intensity for the daughter domain. Unfortunately, a quantitative comparison of intensities is precluded by the likelihood that the crystal may have shifted positions slightly over the course of this experiment. In addition, the effects of repeated stress (as in Section 4.4.2) and acoustomechanical vibration have not been disentangled in this experiment.

Data set collection and analysis[36] (performed at a crystal-detector distance of 10 cm) following the stress experiment confirms the orientation of each of the observable domains. For this crystal, three orthorhombic unit cells of approximate dimension 8 × 14 × 33 Å were identified. They are summarized in the table shown in Figure 5.7t and will be discussed below. The unit cell parameters for all three domains are reasonably close to those of 2,10-undecanedione/urea: a = 8.345 (1), b = 13.939 (1), c = 32.982 (6) Å).[37]

The observation of diffraction from the anomalous domains in the experiment described above demonstrates that nanoscopic domains can grow, but it is unclear how large they must be to be observed by X-rays. Following this first *in situ* experiment, the daughter domain was not itself "homogeneous." Indeed, when observed under the microscope following the stress experiment, this crystal exhibited additional domains within the daughter (Figure 5.7n-s). Because these traverse the crystal at angles of approximately 90° it was conceivable that they contained the third (anomalous) orientation state. Knowledge of the slow axis orientations of these regions was crucial since they were located within the crystal area exposed to the X-ray source (red circles in Figures 5.7n, p, and r).

At high magnification these domains are optically biaxial: they exhibit definite extinguishing and non-extinguishing positions. Their extinguishing orientation, however, coincides with that of the mother domain (Figure 5.7q) and not with either the daughter (Figure 5.7s) or the anomalous domain (Figure 5.7o). At high magnification, the majority of the region of X-ray incidence appears free of additional domains. Although the location photographed in Figure 5.7o,q,s was not in the center of the area of incidence, it was chosen because the optical behavior of the additional domains was most discernible in this region. Because they are aligned with the mother, these domains are not the source of X-ray intensity observed for the third, anomalous domain. The absence of optically observable domain structure for the third domain suggests that it is smaller than the resolution limit of the optical microscope. (Using the 40× objective, the maximum achievable resolution is on the order of 0.4 μm; see Chapter 7.6.4.) This is consistent with an anomalous domain orientation that is composed of nanoscopic twins.

The demonstration of strong diffraction from the third domain orientation in the absence of optical evidence suggests that it is possible for submicroscopic domains to diffract, although further investigation is required. (See the discussion that follows.) In future *in situ* stress diffraction experiments, it is essential that improvements to the rigidity of the stress device be made so that the applied force can be constant and reliable. Alternatively, the ability to record optical photos and X-ray images at the same crystal setting could help to avoid unintended increases in the applied stress caused by goniostat rotation. This might involve mounting a miniature camera near the X-ray source and positioning the requisite illumination and polarization equipment near the location of the detector. A promising setup, in which X-ray and optical equipment were exchanged without moving the stressed crystal, was utilized for the X-ray topography experiments[38] discussed in Section 5.1. In addition, unambiguously locating the region of X-ray incidence is critical so that domain switching occurring *outside* of this region can be excluded as the cause of changes in the oscillation images. This could involve collecting photographs of a fluorescent screen while it is exposed to X-rays. Finally, higher resolution photomicrographs will be extremely helpful in discerning minor changes in the optical behavior of stressed samples.

Additional analysis of the data collected following the stress-diffraction experiment provides greater insight into the subtleties of domain switching and growth. Using Eulerian angles provided in Figure 5.7t, it is possible to compare the relative orientations of the three lattices and demonstrate their distinctness. Eulerian angles are used to relate the orientation of the crystal unit cell to the goniometer (laboratory) frame of reference;[39] their determination was performed by the SMART[40] software used for

identifying the unit cells. The Eulerian geometry is defined as follows. In the diffractometer frame of reference, the z-axis is perpendicular to the ground, the incident beam runs along the y-axis, and the x-axis is normal to both of these. Eulerian angles are defined when all goniostat angles are driven to zero, i.e., when $2\theta = 0°$, $\omega = 0°$, $\phi = 0°$ and $\chi = 0°$. For an orthorhombic unit cell, the first Eulerian angle (E1) is zero when *a* is along the X-ray beam, the second Eulerian angle (E2) is zero when *b* is perpendicular to the beam (but in the equatorial plane), and the third Eulerian angle (E3) is zero when *c* is perpendicular to these (i.e., along diffractometer *z*). For this crystal, rotation in the plane perpendicular to the channel corresponds to rotation about E3. Thus, all three orientation states may be interconverted via rotations of approximately ±60° (in the third Eulerian angle), in accordance with the expected relationships.

In more rigorous terms, when a pair of orientation states in 2,10-undecanedione/urea are twinned across {130}{130} boundaries, they are rotated by 59.1°; when twinned across {110}{110}, they are rotated by 61.8°.[41] Using the SMART software, it is possible to transform one unit cell orientation into another. Because the domains are related by rotations about the c-axis, the transformation matrix has the form:[42]

$$\begin{vmatrix} \cos\alpha & \pm a/b \sin\alpha & 0 \\ \mp b/a \sin\alpha & \cos\alpha & 0 \\ 0 & 0 & 1 \end{vmatrix},$$

where α is the angle of rotation and *b* and *a* are the lattice constants perpendicular to the rotation axis (*b* and *a* axes). For example, from photomicrographs presented in Figure 5.7, it is known that daughter and mother domains border along {110}{110} boundaries.

(This is presented schematically in Figure 5.7x). For the mother domain, application of the transformation matrix,[43]

$$\begin{vmatrix} 0.4726 & -0.5264 & 0 \\ 1.4755 & 0.4726 & 0 \\ 0 & 0 & 1 \end{vmatrix},$$

rotates the mother domain CCW by 61.8°; for this cell, the Eulerian angles match those of the daughter. It is unclear along which boundaries the mother and anomalous domain (or the daughter and anomalous domain) are grown. If mother and anomalous domain border along {130}{130} boundaries, the transformation matrix,

$$\begin{vmatrix} 0.5135 & 0.5125 & 0 \\ -1.4366 & 0.5135 & 0 \\ 0 & 0 & 1 \end{vmatrix},$$

produces a 59.1° CW rotation of the mother cell; application of this matrix to the mother cell produces a cell whose Eulerian angles match those of the anomalous domain. In the fourth column of Figure 5.7t, this first set of "derived" Eulerian angles is presented. (For this orthorhombic unit cell, rotation of +60° is indistinguishable from rotation by –120°. Thus, although they differ by 180°, the third Eulerian angles for the experimentally determined and "derived" anomalous domains describe the same unit cell orientation.) However, since it is unclear if mother and anomalous domain meet along {130}{130}, one must consider the alternative {110}{110} case. For this type of boundary, the domains are related by a 61.8° rotation. Application of the transformation matrix,

$$\begin{vmatrix} 0.4726 & 0.5264 & 0 \\ -1.4755 & 0.4726 & 0 \\ 0 & 0 & 1 \end{vmatrix},$$

produces a 61.8° CW rotation of the mother cell. This second set of "derived" Eulerian angles for the anomalous domain is presented in the fifth column of Figure 5.7t. Since both derived orientations are so close to the experimentally determined orientation, it is impossible to tell which transformation relates mother to anomalous domain; by extension, it is not possible to describe which domain boundary separates them. Nevertheless, this analysis illustrates the distinctness of the three unit cells identified in these data.

Although quantitative comparison of reflection intensities is complicated by the large crystal size and the presence of multiple domains, a rough comparison of domain populations is provided by analysis of the reflection intensities collected during the stress diffraction experiment. Using Origin (v. 7.0, for Windows), peak intensities were measured for the plot profile obtained at the conclusion of the stress experiment (Figure 5.7m). This process involves fitting the intensity data using multiple Gaussian functions and then integrating the area under each Gaussian maximum. In this analysis, conducted by Mark Hollingsworth and the author,[44] three groups of reflections were separated as shown in Figure 5.7u-w. For each, the portion of the line profile is plotted in black (left plot), while the points predicted by the Gaussian fit is overlaid in red (right plot). (Data from each fit are provided in Figure 5.7y-aa.) For the first group of reflections ($(19\bar{3})_{mother}$, $(53\bar{3})_{anomalous}$ and $(\bar{4}6\bar{3})_{daughter}$), an adequate fit was obtained using three Gaussian functions, the maxima of which correspond to the positions of greatest reflection intensity for each of the domains (Figure 5.7u). Here, the relative integrated areas of mother, anomalous domain and daughter are 1.09, 0.618 and 4.29; dividing these areas by the expected reflection intensities (calculated for the room temperature crystal

structure of 2,10-undecanedione/urea[37]) provides the scaled intensities in the penultimate column of Figure 5.7y. (To facilitate discussion, the reflections are multiplied by a factor of 10^4.) These values can be used to compare relative populations of each of the three domains. In the final column, these values have been divided by the summed intensity for the group, providing *relative intensities* for this group of reflections. (Strictly speaking, the structure factors for this crystal are not the same as for 2,10-undecanedione/urea. However, the host substructure should be quite similar for both; therefore, this analysis utilizes reflections of index $l = 3$, which are dominated by the host substructure.) From this group, the mother comprises approximately 23.8% of the total population, the anomalous domain, 3.9%, and the daughter, 72.3%.

In a similar fashion, the second and third groups of reflections were deconvoluted. In the second group ($(28\bar{3})_{\text{mother}}$, $(51\bar{3})_{\text{anomalous}}$ and $(\bar{3}7\bar{3})_{\text{daughter}}$), curve fitting of the three reflections is complicated by the broad hump centered within the group (Figure 5.7v). This hump appears most prominently as shoulders on the lower portions of the mother and anomalous domain reflections and may contain contributions from multiple domains. This group was therefore fitted using four Gaussian functions, one of which corresponded to the broad hump. The relative integrated areas of mother, anomalous domain and daughter were 0.641, 0.248 and 1.84; the area of the hump was 1.06. For the three observed reflections, the calculated relative populations are 11.6%, 9.3% and 79.1%. Because the broad hump was centered nearer the maximum for $(51\bar{3})_{\text{anomalous}}$ than $(28\bar{3})_{\text{mother}}$, the contribution to the anomalous domain might increase its *apparent* population; however, the close correspondence between modeled and observed intensity suggests that the reflection intensity was measured appropriately. In any event, these data

appear *qualitatively* similar to the value determined from the first reflection group (Figure 5.7v) and are consistent with the daughter population, which constitutes approximately 72-79% of the total population for all three groups of reflections.

For the third reflection group ($(37\overline{3})_{\text{mother}}$, $(5\overline{13})_{\text{anomalous}}$ and $(\overline{2}8\overline{3})_{\text{daughter}}$), the intensity of $(5\overline{13})_{\text{anomalous}}$ was not quantifiable (Figure 5.7w). (Since the fitted data presented in Figure 5.7w exhibits a hump near $(5\overline{13})_{\text{anomalous}}$, the data used to generate this plot must have consisted of three Gaussian functions. Unfortunately, these data were lost; the numerical data discussed here is based on a fit with two Gaussians.) Although observed at other points in the stress experiment (see Figure 5.7g and i), this reflection was not readily observed in this rotation image; with greater sensitivity, perhaps this reflection would become observable following stress release. Nevertheless, the relative integrated area of reflections from mother and daughter, 0.801 and 5.28, provide relative populations of 26.6% (mother) and 73.4% (daughter). Again, the daughter is present in approximately three times the population of the other possible orientation states, as expected from a portion of crystal that exhibited plastic domain switching.

Although Figure 5.7y-aa provides relative intensities within each group of reflections, it is possible to compare all reflections. For instance, the scaled area ($\times 10^4$) of the anomalous domain reflection in group 1, $(5\ 3\ \overline{3})_{\text{anomalous}} = 1.381$; this value is about 25.8% as large as $(2\ 8\ \overline{3})_{\text{mother}}$ (group 2; scaled intensity = 5.352) and about 3.9% as large as the *mean* scaled area (= 3.52) for all three mother reflections analyzed (see Figure 5.7ab). Since the mean scaled intensity for three daughter and mother reflections were very similar, $(5\ 3\ \overline{3})_{\text{anomalous}}$ is also 3.9% as intense as the *mean* scaled intensity for all three reflections from the daughter domain (= 3.54); while $(5\ 1\ \overline{3})_{\text{anomalous}}$ is approximately

12.2% as large as the combined intensity for all reflections from both mother and daughter domains.

These data illustrate that diffraction intensity from channels exhibiting the third domain orientation can be comparable (on the order of 4-12%) to intensity observed for mother and daughter domains. Due to the large size of this crystal and the presence of an unquantified fraction of daughter and mother domain *within* the incident X-ray beam, a quantitative comparison of these domain populations is not possible. (For instance, the scaled areas of three reflections from the mother domain differ by a factor of 2.99. For the daughter domain, this factor is only 1.7. This discrepancy probably arises from changes in volume elements that pass through the incident beam as the crystal is rotated.) Nevertheless, a *qualitative* comparison of domain populations appears reasonable. In the absence of optical evidence for the anomalous orientation state (Figure 5.7n-s), this is strong evidence for diffraction by submicroscopic domains (intimate twins) and concurs with the observation that such domains can grow (in size or concentration) as a response to ferroelastic stress.

Although the anomalous domain orientation was observed with this experiment, it does not guarantee the presence of nanoscopic twins. Even though such domains were not observed in photomicrographs recorded during the experiment, the increased stress applied during rotation image collection could have given rise to domains of the anomalous orientation that were large enough to diffract. This possibility was addressed during a second *in situ* stress diffraction experiment. In this experiment, a crystal grown from a methanol solution a 90:10 mixture of 2,10-undecanedione and 2-undecanone was compressed in smaller increments. (For this experiment, a 3.3 cm long Allen key was

used to adjust the applied stress; this permitted the application of finer graduations of strain. The circumference of the circle traced by this key is approximately 21 cm; for control of 2.1 mm, or 3.6° rotation, the highest precision in the applied strain is estimated at 3.1 μm. For this crystal, L_0 = 2.24 mm; therefore, strain could be applied to an estimated maximum accuracy of 0.1_4%.) Another improvement was the addition of a λ plate into the optical light path; this improved the brightness and contrast in the photomicrographs. The experiment is illustrated in Figure 5.9; as with the first *in situ* experiment, photomicrographs were taken before the crystal was rotated into position for the X-ray rotation image (60 s rotation through 6° ϕ). For this experiment,[45] the goniometer settings during collection of the rotation image were 2θ = 20°, ω = 0°, ϕ = 41°, χ= -30°; for the photomicrographs, ϕ = 116.1°. Finally, the distance between the crystal and the detector was increased from 5 to 7 cm.

In this trial, crystal stress was measured both initially (at the position used for photomicrograph collection) and during collection of each rotation image (once the crystal had been rotated 85° through ϕ). (Both values are provided in Figure 5.9.) Although the goniometer settings were slightly different between this experiment and the last, the increase in force (and, presumably, strain) measured during collection of rotation images is appreciable and is probably comparable to those produced in the first experiment. As discussed below, the differences in stress measured for these two goniostat settings raises the question of whether the daughters could have grown to microscopic size during collection of the rotation images in the first and second experiments. It is therefore difficult to make any firm conclusions concerning diffraction from daughter domains that are not observed optically.

At the outset of this experiment, Figure 5.9a, the domain structure of this crystal appeared homogeneous in the photomicrograph and accompanying X-ray rotation image. At 0.2% strain, reflections from daughter domain were observable in the rotation image (see arrows), yet the photomicrograph provided no evidence of domain switching (Figure 5.9b). Unfortunately, the appreciable increase in stress (from 4.5 to 18 cN) incurred between collection of the photomicrograph and the rotation image makes any conclusion inappropriate: the crystal may or may not have possessed optically visible daughter domains (in the region of X-ray incidence) during collection of the rotation image. Upon stress release (Figure 5.9c), pseudoelastic reversion occurred, and the rotation image exhibited reflections from a single unit cell orientation.

When stress was reapplied, reflections from a second domain were again observed. At 0.5% strain, the photomicrograph collected before the rotation image (Figure 5.9d), showed only mother domain; upon reorientation of the crystal for collection of the rotation image, the measured force increased from 14 to 21 cN, and strong reflections from the daughter domain were observed. What makes this portion of the experiment interesting is that once the crystal was reoriented (following collection of the rotation image in Figure 5.9d) and a second photomicrograph collected, the effects of the increased stress became obvious. Figure 5.9e provides the photomicrograph taken immediately following the return to the appropriate goniometer setting; here, the settings of the stress-strain device had not been adjusted since the collection of the preceding X-ray rotation image. Although the measured force had decreased (from 21 cN) to 7 cN, a large stripe of daughter domain crossed the region of X-ray incidence. Presumably, this daughter was present during the collection of the diffraction image, and it remained

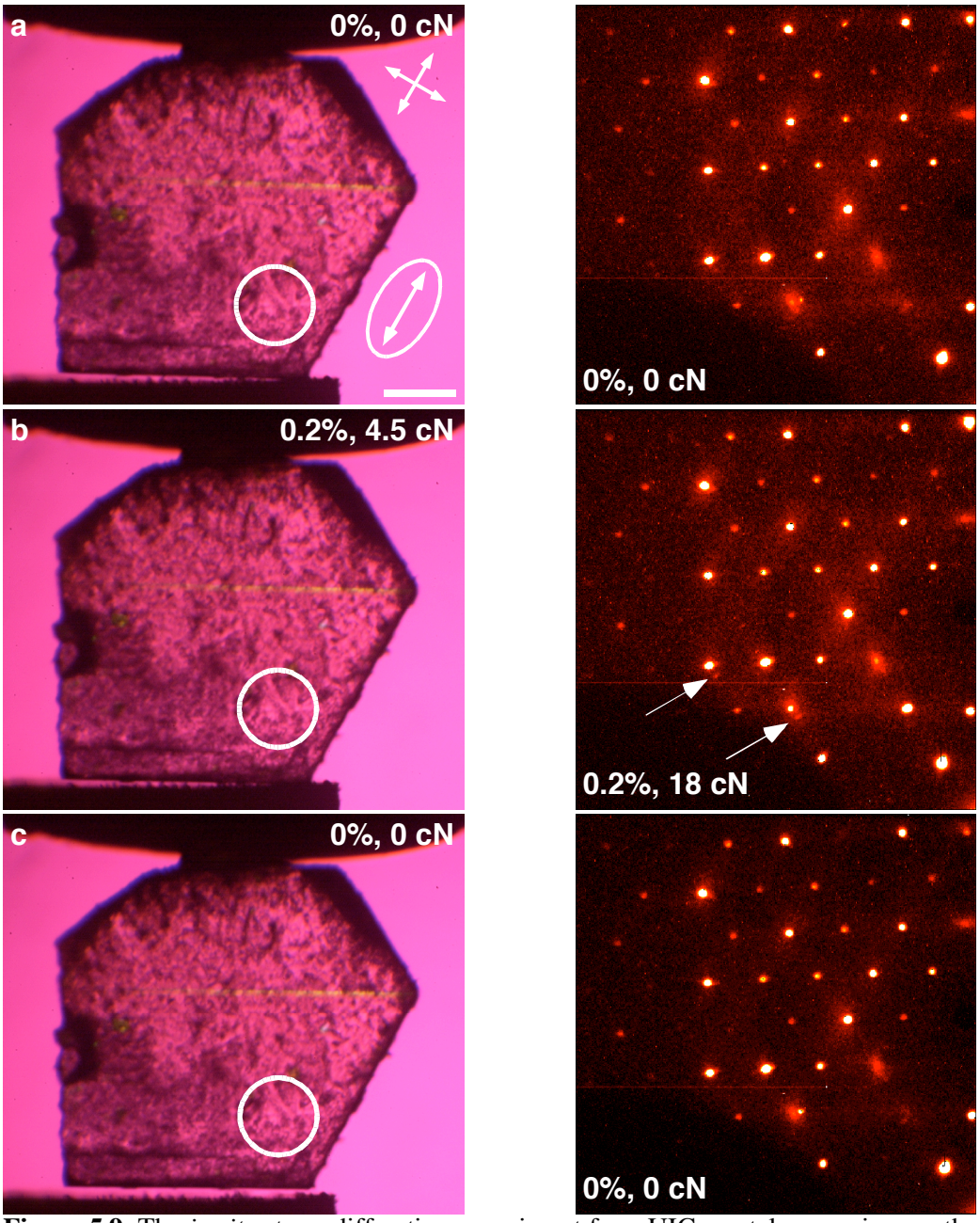

Figure 5.9 The *in situ* stress diffraction experiment for a UIC crystal grown in a methanol solution containing a 90:10 mixture of 2,10-undecanedione and 2-undecanone. This experiment was performed as the experiment described in Figure 5.7. Photomicrographs (crossed polars oriented as shown, λ plate) were taken prior to each X-ray rotation image. The slow axis orientation of the mother domain is shown by the arrow; the circle denotes the approximate area of incidence for the X-rays (0.50 mm collimation). During collection of the rotation images, the crystal was oriented so that [100] was vertical (and [010] was horizontal). In each photomicrograph and accompanying rotation image, the applied stress and strain are provided. Because these were collected at different goniometer positions, for a given setting, the applied stress increased during collection of the X-ray image. At 0.5% strain (**d**), this increase is enough to induce domain reorientation within the crystal (see bright region in **e**). (The photomicrograph in **e** was collected immediately following the rotation image in **d**; no adjustments to the stress-strain device, other than the goniometer orientation, were made.) The uncertainty in applied stress is discussed in the text.

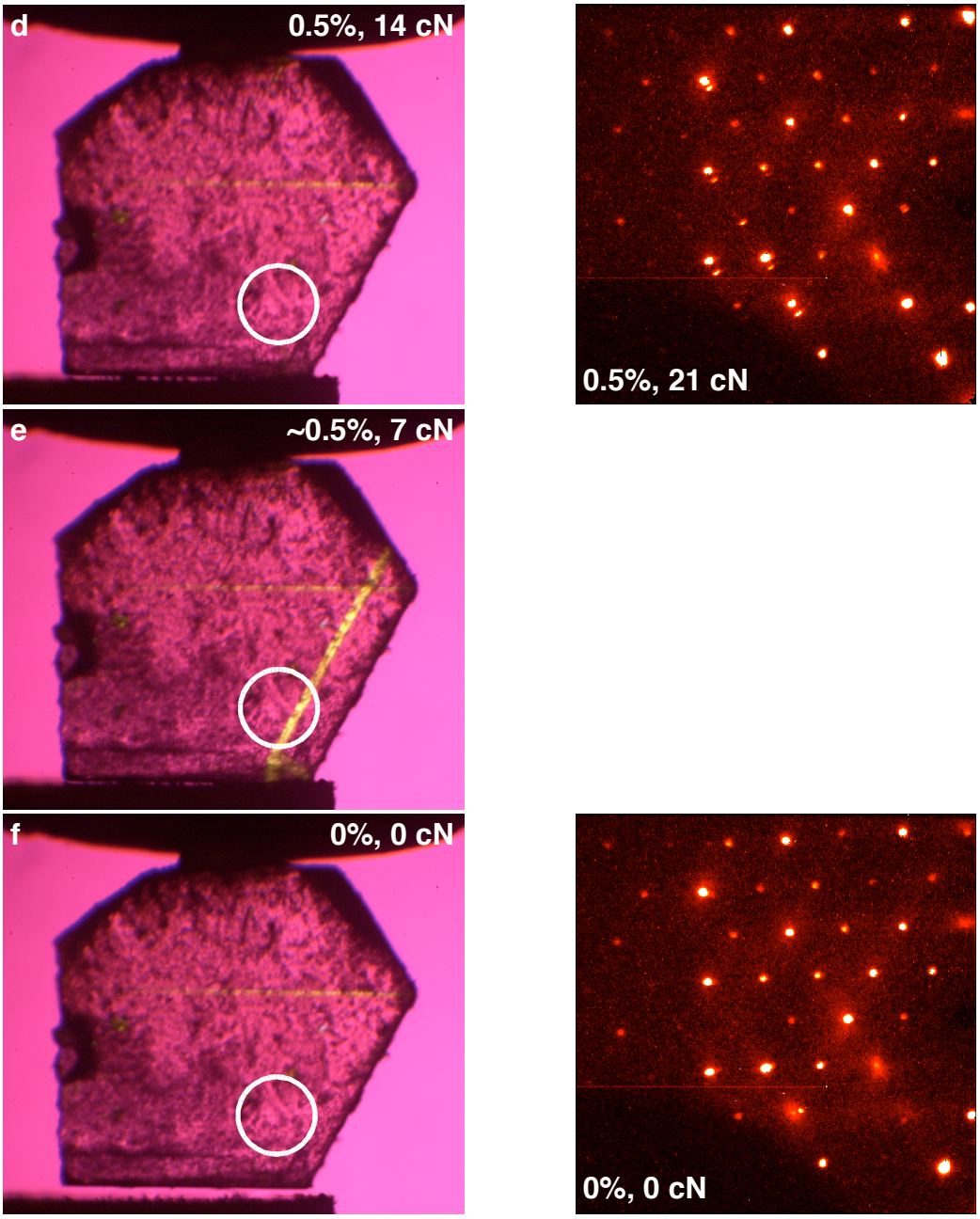
d
0.5%, 14 cN
0.5%, 21 cN
e
~0.5%, 7 cN
f
0%, 0 cN
0%, 0 cN

because of ferroelastic hysteresis. Its observation underscores the potential difficulties in observing X-ray diffraction maxima by domains too small for detection by optical means and emphasizes the importance of designing an experiment in which the photos and X-ray frames can be taken without changing the crystal's position.

How do domains possessing the third orientation become visible to X-rays? In Section 5.1.1, the emergence of domains possessing the third orientation was described for a UIC crystal containing 11% 2-undecanone. In that crystal, the twins ran parallel to [310] and were also parallel to the topograph striations observed in that sector (see Figure 5.5). This suggests that twins observed in photomicrographs such as Figure 5.4e are related to the nanoscopic twins responsible for the striations. In other words, nanoscopic twins can exhibit the third, anomalous, orientation.

If they are simply the third ferroelastic orientation state, the nanoscopic domains should exhibit ferroelasticity. A process by which this occurs is postulated in Figure 5.10. (Referral to the helical wheel diagram in Figure 5.15 (Section 5.2.2) may be of assistance to the following discussion.) On a microscopic scale, the mother domain appears populated by channels exhibiting a single orientation state. If nanoscopic twins are present within this otherwise homogeneous phase, they may possess either of the two alternative orientation states: depending on the direction of applied stress, one of these (the one that is able to reorient and not counter the applied stress) is called the daughter and the other, the third orientation state. (Alternatively, they can form a displacive twin such as those presented in Figure 4.3c. However, twins such as these are not observable in the *in situ* stress-diffraction experiment because they are merohedral, as discussed below.) Figure 5.10a schematically depicts a possible mother domain, which

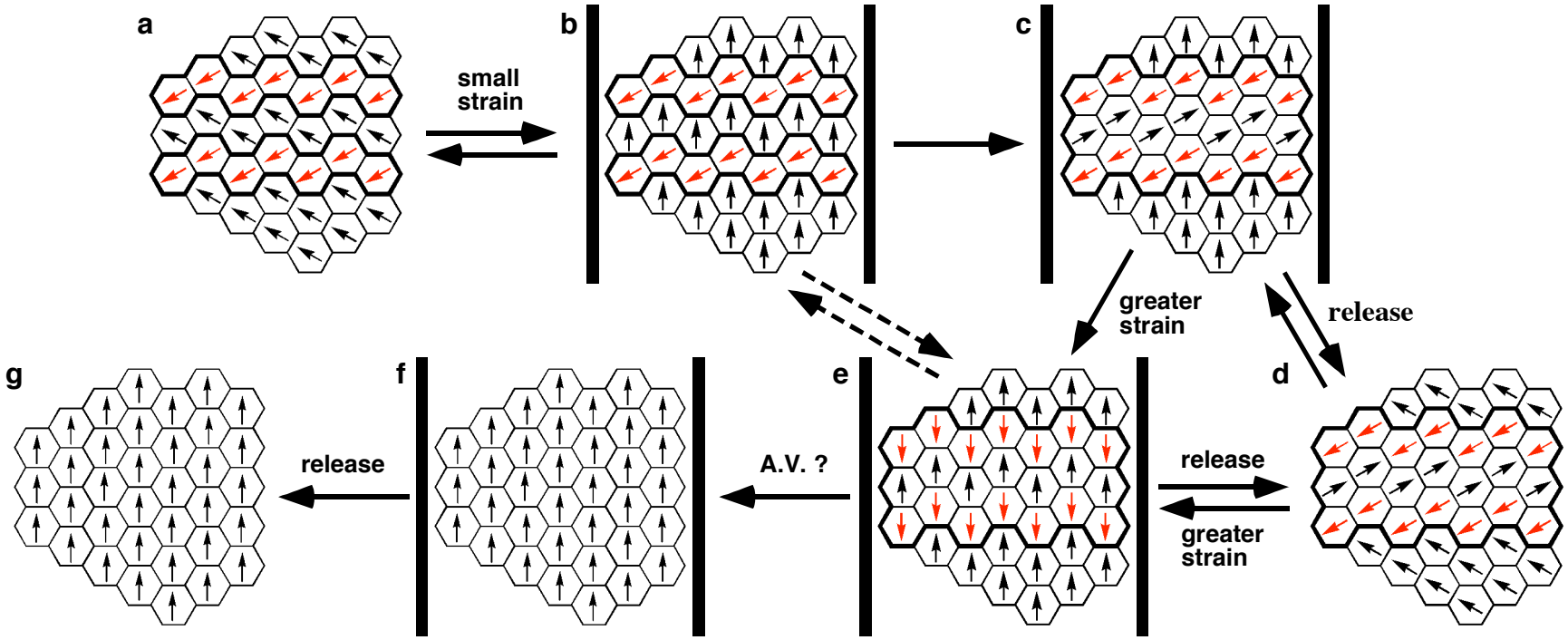

Figure 5.10 The proposed mechanism of ferroelasticity and the origin of the "memory effect" in UICs. **(a)** The unstressed crystal. This crystal is composed of a mother domain that is twinned with small populations of nanoscopic domains, the orientation of which is approximately 60° from the mother. In this example twins are epitaxially matched across {130}{130} boundaries. **(b)** When a light compressive force is applied (using the black stress bars), ferroelastic domain switching of the mother domain to the daughter creates strain mismatch at boundaries with the nanoscopic twin. This unfavorable condition can be alleviated either by reversion to **a** (if the stress is released) or by a second reorientation of interleaving daughter domains to produce twins displaced along the channel by 5.5 Å and rotated by 180° from the nanoscopic domains **(c)**. This twin is epitaxially mismatched with surrounding regions; like **b**, it can drive domain reversion. It is thought that the growth of nanoscopic domains under stress lowers their energy by increasing their volume in comparison to the surface area at epitaxially mismatched boundaries. Accordingly, the removal of stress and concomitant domain reversion of daughter can sometimes leave these domains intact, as in **d**. However, since the strain of the nanoscopic twin opposes the applied stress, greater strain can cause it to reorient as well to form **e**. (This may also occur from state **b**.) In **e**, the nanoscopic domains and the daughter are merohedrally twinned. Although stability is gained via strain epitaxy, the loss of host-guest hydrogen bonding at the twin boundaries destabilizes the merohedral domains to some extent. **(f)** Acoustomechanical vibration (A.V.) is known to stabilize daughter domains. This may occur through the reorganization of nanoscopic domains so they become aligned with the daughter, as in **f**. This allows the reconstruction of host-guest hydrogen bonds that were missing at the twin interfaces in **c**, **d** and **e**. **(g)** Since the daughter is no longer destabilized by strain mismatch and missing hydrogen bonds, it remains following stress release.

incorporates small amounts of nanoscopic twins that are degenerate with respect to the applied stress. These twins border the mother domain along epitaxially matched {130}{130} boundaries, so they are probably quite stable in the unstressed crystal. (Although not discussed in this diagram, nanoscopic twins along {110}{110} are also possible. For appropriately oriented stress, these can give rise to the memory effect via a mechanism similar to the one depicted in Figure 5.10.)

The helical nature of the urea channel dictates that guests in the mother and nanoscopic twin it encloses, which are related by ~60° rotation, are displaced from one another along the urea channel by 1.83 Å (or, alternatively, that value plus 11.0 or 22.0 Å). As the crystal is lightly stressed, the mother undergoes domain switching to create daughter for which the strain does not oppose the applied stress. This requires 60° rotation *away* from the nanoscopic twin orientation, so they are now related by 120° rotation and 3.68 Å translation (Figure 5.10b). At this point, these domains are not epitaxially matched at their intersection, and a high-energy {130}{100} boundary has resulted (refer to Figure 4.3b). This kind of strain mismatch is thought to destabilize the daughter and drive domain reversion in pseudoelastic crystals (see Section 4.2.2). In this diagram, such a process involves reversion from the state depicted in Figure 5.10b to a.

For the nanoscopic domains in Figure 5.10b, the orientation of strain makes them destabilized by the applied stress. Further destabilization comes from epitaxial mismatch with surrounding daughter domain. To alleviate the problem of epitaxial mismatch, either of two outcomes can be envisioned: the nanoscopic twins can reorient so as to coincide with the daughter, or the daughter can reorient so as to coincide with the

nanoscopic twin. Each outcome results in the formation of a {100}{100} twin described in Figure 4.3c and the recurrence of strain epitaxy.

The case in which the nanoscopic twin reorients to coincide with the daughter is discussed first. This possibility appears reasonable because the nanoscopic twin in Figure 5.10b remains in opposition to the stress (and the daughter does not). With the assumption that channels within each domain have the same chirality, the orientation of the stress bar and the helical channel architecture requires a rotation-translation of the nanoscopic twin *in the opposite sense* as the transformation from mother to daughter, forming the state in Figure 5.10e. Thus, guests within the reoriented nanoscopic twin and daughter become differentiable by 180° and a 5.5 Å translation along the channel. In a metrically orthorhombic lattice such as this, twins related by 180° rotation (about a primary axis) are merohedral. However, because merohedral twins[46,47] exhibit coincident reflections, the reorientation of nanoscopic twins cannot explain the appearance of the reflections from this anomalous orientation state in the stressed crystal described in Figure 5.7. Although it may be possible for nanoscopic twin to become coincident with daughter (i.e., Figure 5.10 b → Figure 5.10e, this transformation remains unproven; the arrows connecting Figure 5.10b and e are therefore dashed.

The second possibility, the reorientation of daughter domain, is quite intriguing. If portions of the daughter reorient *instead* of nanoscopic twin, the reoriented daughter can become epitaxially matched with the nanoscopic twin and lend stability to that region. The realignment of small portions of daughter domains with nanoscopic twins creates epitaxially matched {130}{130} boundaries between the two (Figure 5.10c) and increases the size of the nanoscopic twins. The ratio of volume to surface area for this

merged twin is larger than for the nanoscopic twin in Figure 5.10a, so it should exhibit increased stability. As above, this displacive twin contains guests that are related by 180° rotation and 5.5 Å translation. However, the orientation of this twin is the same as for the initial (unmerged) nanoscopic twin, so it is possible that such merged twins could diffract X-rays coherently. Although portions of the daughter must reorient in a way that resists the applied force, this mechanism explains the emergence of reflections from the third orientation in the stress diffraction experiment and is plausible at lower stresses. The creation of larger, epitaxially matched displacive twins between daughter and nanoscopic twin will stabilize the metastable nanoscopic twin; growth of this domain makes it observable to X-ray diffraction and, in certain cases, with optical microscopy (see Figures 5.4e-f and 4.16). The stability achieved by merging daughter and nanoscopic twins suggests that the energetics at twin interfaces can overcome the energetic bias induced by the applied force at low stresses. (It should be pointed out that, although the displacive twins are epitaxially matched, the host-guest hydrogen bond network is disrupted at the domain boundary because the guest hydrogen bond acceptors are offset. As discussed in Section 1.1.2, hydrogen bonding between donor ureas and two guests imparts a large degree of cooperativity and stability to the crystal. It follows that a reduction in the host-guest hydrogen bonding at the domain boundary between displacive twins should lessen its stability, although probably not enough to offset the stability incurred by the formation of epitaxially matched boundaries.)

The disappearance of the third domain orientation from X-ray rotation images collected at higher stresses is also explained by this mechanism. If the displacive twin in Figure 5.10c should form, it appears reasonable that this domain can undergo ferroelastic

reorientation as a result of increased stress. In the stress diffraction experiment, the reflection intensity from the third orientation state disappeared between 2 and 4% strain. If the merged twin (Figure 5.10c) undergoes domain switching, it would form a displacively twinned region within the daughter, as in Figure 5.10e. Here, the merged twin has reoriented in response to the increased stress and has become aligned with the daughter domains: a second merohedral twin is formed, and the reflections from the third orientation become merged with those of the daughter.

Upon release of stress, the recurrence of reflections from the merged twin (Figure 5.7i) indicates relaxation to the state such as that depicted in Figure 5.10d. Here, the daughter has relaxed to mother, and the merged nanoscopic twin has reverted to its original orientation. However, the observation of reflections from the merged twin after release of stress demonstrates that the merged twins remain intact. Apparently, epitaxial match between the merged twin and mother domain (Figure 5.10d) favors their boundary over epitaxially mismatched boundaries between unmerged nanoscopic twin and daughter (Figure 5.10b) so that the merged twin is still observable. (From the observed diffraction intensity, discussed above, it appears that an appreciable population of this twin is generated in this experiment.) Thus, the domain structure of the parent and its energetics have changed as a result of stress.

Because they possess different potential energies, domain structures such as those depicted in Figure 5.10b-e should exhibit different reversion kinetics. As discussed in Section 4.4.2, there is strong evidence that instantaneous reversion rates depend on the applied strain. For the crystal containing 11.5% 2-undecanone, three consecutive stress attempts to similar strains (0.44, 0.55 and 0.39%, respectively) revealed close similarities

in the distribution of instantaneous rates. However, when the crystal was compressed a fourth time, to 0.77% strain, the distribution of rates exhibited an appreciable shift to slower values, and the lifetime of the reversion event was extended from about 30 ms to 730 ms. This behavior could arise for several reasons, including: (1) the daughter occupies regions of different guest composition, (2) the domain wall traverses different regions of the crystal, and (3) greater amounts of displacive twin (Figure 5.10e) are formed at increased applied strains. Since, during the fourth attempt, the daughter occupied a different region (see Figure 4.34), options 1 and 2 might appear to be favored over 3. However, during the fifth attempt (to 0.56%), the daughter grew to approximately the same size as in the fourth attempt, and the rate distribution shifted toward faster rates. For this crystal, repeated daughter formation within the same region gave rise to increased reversion rates, which suggests the reversion kinetics were not affected by differences in crystal composition or location (options 1 and 2) but leaves open the possibility that reversion can be influenced by the domain structure of the reverting region. The faster rates observed in stress attempt V could result from either an increase in the driving force for domain reversion or a decrease in the number of defects that resist reversion. In the model presented in Figure 5.10, the first option (greater driving force) corresponds to a domain structure such as that of Figure 5.10b whereas the second option (fewer defects that resist reversion) might correspond to a domain structure such as Figure 5.10e. In either case, the distribution of instantaneous rates appears to depend on the amount of compression, which is postulated to have an important effect on the domain structure.

For the process of domain switching described in Figure 5.10, the potential energy surface should look like Figure 5.11.[2] Unlike the potential energy surface described in Figure 4.1, this diagram also explores the possible effects of nanoscopic twinning. Starting from a mother domain and epitaxially matched {130}{130} nanoscopic twin (A), the application of stress along the horizontal direction (see black stress bars) results in domain switching of the mother to give daughter B (Figure 5.10b). As long as the nanoscopic domain does not itself reorient, the resulting {130}{100} boundary between daughter and nanoscopic twin destabilizes B with respect to A. The application of greater amounts of stress drives the ferroelastic reorientation of nanoscopic domains that produces a daughter, C (Figure 5.10e), that is epitaxially matched and therefore lower in energy than B. For both states, the loss of host-guest hydrogen bonds at the twin interface (for A, {130}{130}; for C, {100}{100}) should destabilize the system relative an untwinned domain. But how does this difference in stability correlate with the size of the nanoscopic twin?

Although their size and number remain unknown, Figures 5.10 and 5.11 depict the limiting case in which the nanoscopic twins measure one unit cell across. Within domains of this size, guest-host-guest hydrogen bonds can form within the nanoscopic domain in A, but not in C. This contributes to the destabilization of C. As the width of the twin is increased, the disparity between A and C should be reduced so that at some point they become comparable in energy. The importance of this effect can be estimated by counting the number of guest-host-guest hydrogen bonds that can be formed as a function of twin size. In Figure 5.11, A has three of these bonds, while C has none. In a real crystal, these twins almost certainly span lengths greater than seven channels, so C

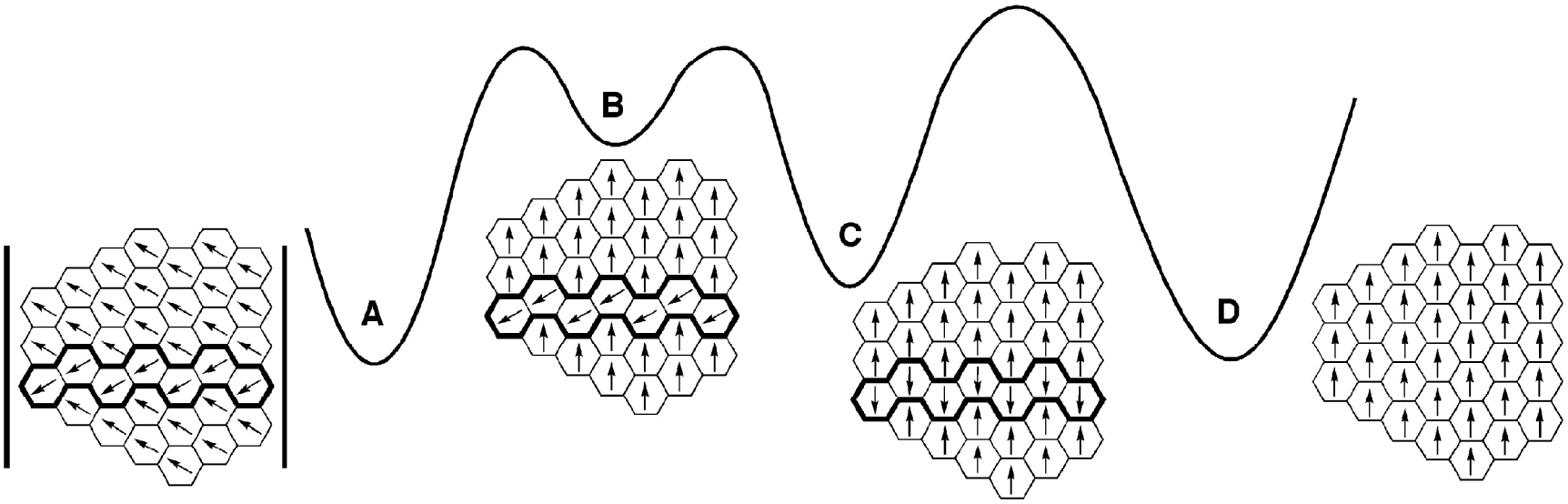

Figure 5.11 A schematic potential energy (PE) surface for ferroelastic domain switching in UICs and representative domain structures. Starting from A, the mother and nanoscopic domains are epitaxially matched along {130}{130} boundaries (Figure 5.10a). (Here, the nanoscopic domain is drawn as a single channel that is surrounded by large regions of mother. The size and number of nanoscopic twins is not known. In addition, twins may also occur along {110}{110} boundaries.) Neither of these domains is stable when stress is applied horizontally (see black stress bars). Under stress, the mother domain is most likely to reorient first (see text), yielding a state such as B. For this disordered state, energetic destabilization is caused by strain mismatch at the {100}{130} boundary between daughter and nanoscopic domains. If the stress is removed, this metastable state will revert to A. However, the alignment of nanoscopic domains with the daughter can relieve the strain mismatch and stabilize the daughter. This process is thought to involve merging the daughter and nanoscopic twin, as depicted in C (see Figure 5.10e). Although epitaxially matched, C is missing some of the host-guest hydrogen bonds present at {100}{100} boundaries within each twin. If the nanoscopic domains are small enough, this destabilization may be great enough to drive pseudoelastic reversion to A. However, acoustomechanical vibration under stress may facilitate the reorientation and translation of guests within the nanoscopic domain so that they become aligned with the daughter, D (see Figure 5.10f). For this to occur, the strain of these channels must at some point oppose the applied stress; the barrier for this process should therefore be higher than that between B and C. For D, the strain mismatch of B has been repaired and the hydrogen bonds missing in C have been recovered; the defects created by stressing the crystal have been annealed so that the daughter is now stable compared to the mother. (D may be lower in energy than A). Figure adapted from Hollingsworth, *et al.*, *Cryst. Growth Des.*, **5**, 2100-2116, (2005).

should be appreciably destabilized if the nanoscopic twin is one channel across. However, as the width of the twin increases, the disparity between C and A decreases. For a twin *n* channels wide, the fraction, f, of possible host-guest hydrogen bonds that are satisfied can be computed[4] as $f_A = \frac{(2n-1)}{2n}$ for state A; for state C, $f_C = \frac{(2n-2)}{2n}$. From these relationships it is clear that the difference in the number of hydrogen bonds between states A and C drops off quickly: by $n = 3$, $\frac{f_C}{f_A} = 0.80$; for $n = 10$, $\frac{f_C}{f_A} = 0.95$. Inasmuch as the barrier to ferroelastic domain switching is substantial and host-guest hydrogen bonds in C are comparable in strength to those in A, the energetic disparity between states A and C (arising from differences in the number of hydrogen bonds) should be unimportant for all except the thinnest nanoscopic twins.

This discussion is important because it provides an approximation of the size of a typical nanoscopic twin in ferroelastic UICs. The pseudoelastic memory effect of UIC crystals containing 2,10-undecanedione is well established.[2,37] If the model for nanoscopic twinning and its effect on the ferroelastic potential energy surface is correct, then C must less stable than A. Otherwise pseudoelastic reversion would not occur at higher strains. In the first *in situ* stress diffraction experiment (Section 5.2.2), reflections from the third domain orientation disappeared above 2% strain. When this occurs, state C should become populated; if it is indeed destabilized with respect to state A, the population of C should favor pseudoelastic reversion. As discussed Section 4.3.2 (see Figure 4.9), there are many examples of crystals that exhibit pseudoelastic reversion from strains of greater than 2%. Thus, it appears that C is destabilized with respect to A,

which suggests the presence of at least a fraction of nanoscopic twins that are small enough for hydrogen bond differences to be important. From the above discussion, the width of such twins might be on the order of 10 channels or less.

In Figure 5.10, the potential effect of acoustomechanical vibration is also explored. In the stress experiment described in Section 4.3.2, a UIC crystal containing a 90:10 mixture of 2,10-undecanedione and 2-undecanone demonstrated pseudoelastic behavior at 35 cN force. When once again compressed with 31 cN of force, the application of a 4.1 kHz acoustomechanical vibration resulted in the creation of plastic daughter domains. Apparently, treatment of this crystal with acoustomechanical vibration reduced the favorability of spontaneous reversion. If the driving force for the ferroelastic memory arises from epitaxial mismatch at nanoscopic twin boundaries (as in Figure 5.10b), then the recovery of strain epitaxy through a process of merging twins (as in Figure 5.10c) should lead to its "erasure." In addition, for a merged displacive twin (Figure 5.10e), such an "erasure" might involve reorientation of the displacive twin so that it becomes part of the daughter domain. One possible way for this to occur is depicted in the progression from Figure 5.10e to f. Between these states, conversion of the displacive daughter (Figure 5.10e) to the annealed daughter (Figure 5.10f) requires a 180° rotation and 5.5Å translation of the guest along the channel axis. Although this process appears difficult, similarly large guest translations of 5.5Å have been observed in phase transitions of stacked-loop UICs at even much lower temperatures.[48] For the system of interest, acoustomechanical vibration may provide the energetic impetus for such large scale reorganization. By annealing the nanoscopic twins within the daughter domain, hydrogen bonds lost at the displacive domain boundary are regained. The

relaxation of nanoscopic domains by acoustomechanical vibration may then result in a more stable, permanent daughter domain.

Should acoustomechanical relaxation decrease the population of merged nanoscopic domains shown in Figure 5.10c, a reduction in their reflection intensity might be observable in the X-ray rotation photos of the stressed crystal. Because acoustomechanical treatment reduces the tendency for spontaneous domain reversion, one might anticipate that this treatment could give rise to several possible changes in domain structure, including (1) the alignment of switched daughter channels with unswitched nanoscopic twins (Figure 5.10b to c), (2) domain switching of nanoscopic twins (Figure 5.10b to e), (3) reorientation of merged twins (Figure 5.10c to e), or (4) the rearrangement of the merged nanoscopic twins to match the daughter (Figure 5.10e to f). For a given crystal, the likelihood of these possibilities probably depends on the crystal's domain structure when the acoustomechanical vibration is applied. As discussed above, stress-diffraction experiments of greater sophistication may provide information that will favor (or disfavor) some of these possibilities.

In a follow-up experiment, a third UIC crystal grown[49] by Dr. Matthew Peterson from a methanol solution containing a 90:10 mixture 2,10-undecanedione and 2-undecanone was stressed, and alternating photomicrographs and rotation images were collected.[50] This experiment was to be more refined than the first two, with a clearer idea of what could be observed. Following cleavage from a larger crystal, the stressed fragment had a width (L_0) of 870 μm. (Thus the greatest precision in the applied strain is estimated at 0.4%.) For most of the rotation images, the initial goniometer settings were $2\theta = 20°$, $\omega = 0°$, $\phi = 30°$, $\chi = -30°$; from this, 6°, 30 s rotations in ϕ were used. (For the

rotation image provided in Figure 5.12j, $2\theta = 0°$.) Photomicrographs were recorded at $\phi = 108°$ (all other parameters were the same), and the crystal-detector distance was 10 cm.

The stress experiment is illustrated in Figure 5.12. This fragment was mounted to the goniometer stress-strain device using epoxy adhesive. In photomicrograph **a**, taken before the application of stress, the region of X-ray incidence appears as a single domain; the accompanying rotation image demonstrates a single crystal lattice with the correct orientation of a and b axes (see Figure 5.12a). (There is a small, switched region located immediately to the left of the estimated area of incidence. The single set of reflections observed in oscillation images such as Figure 5.11a suggests that this domain lies outside of the incident region and therefore does not interfere with the experiment.) In total, the crystal was subjected to seven cycles of stress and release: the maximum strains were 0.9%, 1.1%, 1.4%, 1.8%, 2.1%, 3.7 and 5.3%. As with the second experiment, the applied stress varied between collection of oscillation images and photomicrographs (Figure 5.12a-q); stress values are provided for each. During the first cycle, the emergence of a reflection from a second domain was optically visible at 0.5% strain (see arrow in Figure 5.12b). A schematic diagram of this daughter (which is oriented the same as the daughter domain that lies outside of the incident region) is provided in Figure 5.12b. Here, one notes {110}{110} boundaries between mother and daughter regions. In the accompanying photomicrograph, a small band can be seen to cross the region of X-ray incidence (see arrow). Although it is unclear from this image whether or not this band is daughter domain, its continued growth at greater stresses (see arrows in Figure 5.12c-e) and related increase in reflection intensity suggests that it is. At 0.9% strain (Figure 5.12c), this band appeared to grow (as did others), and the additional reflection

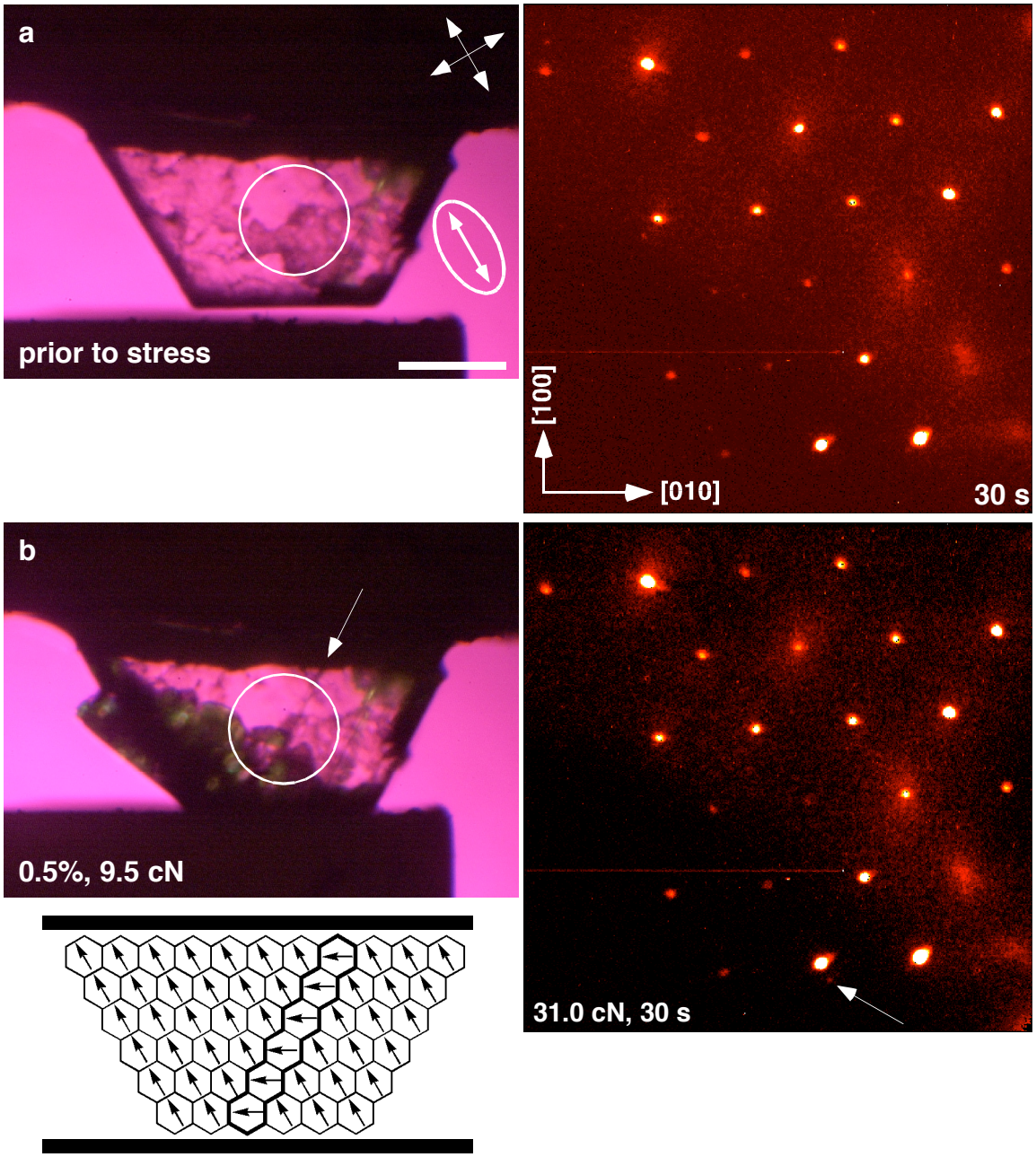

Figure 5.12 *In situ* stress diffraction experiment on a UIC crystal containing a mixture of approximately 90:10 2,10-undecanedione and 2-undecanone. At each stress increment, a photomicrograph (crossed polars, λ plate) was taken followed by a X-ray rotation image. In the photomicrographs, the slow axis orientation of the mother domain is denoted by the single arrow; the polarizer and analyzer are approximately parallel to the crossed arrows. Stress applied along the vertical axis (the stress bars are visible in the photomicrographs) produced daughter domain with slow axis orientation approximately 60° CCW from this. During collection of the rotation images, $[100]_{mother}$ was vertical (see arrow in **a**), and the detector was located 10 cm from the crystal. The approximate location of incidence for the X-rays (0.50 mm collimation) is denoted by the white circle. For each photomicrograph, percent strain and the applied force applied are provided; for each rotation image, the applied force and the time of exposure are provided. Scale bar (in the photomicrographs) = 0.50 mm. With the exception of **j**, the diffractometer parameters are $2\theta = 20°$, $\omega = 0°$, $\phi = 30°$ to $36°$, $\chi = -30°$. For **j**, $2\theta = 0°$.

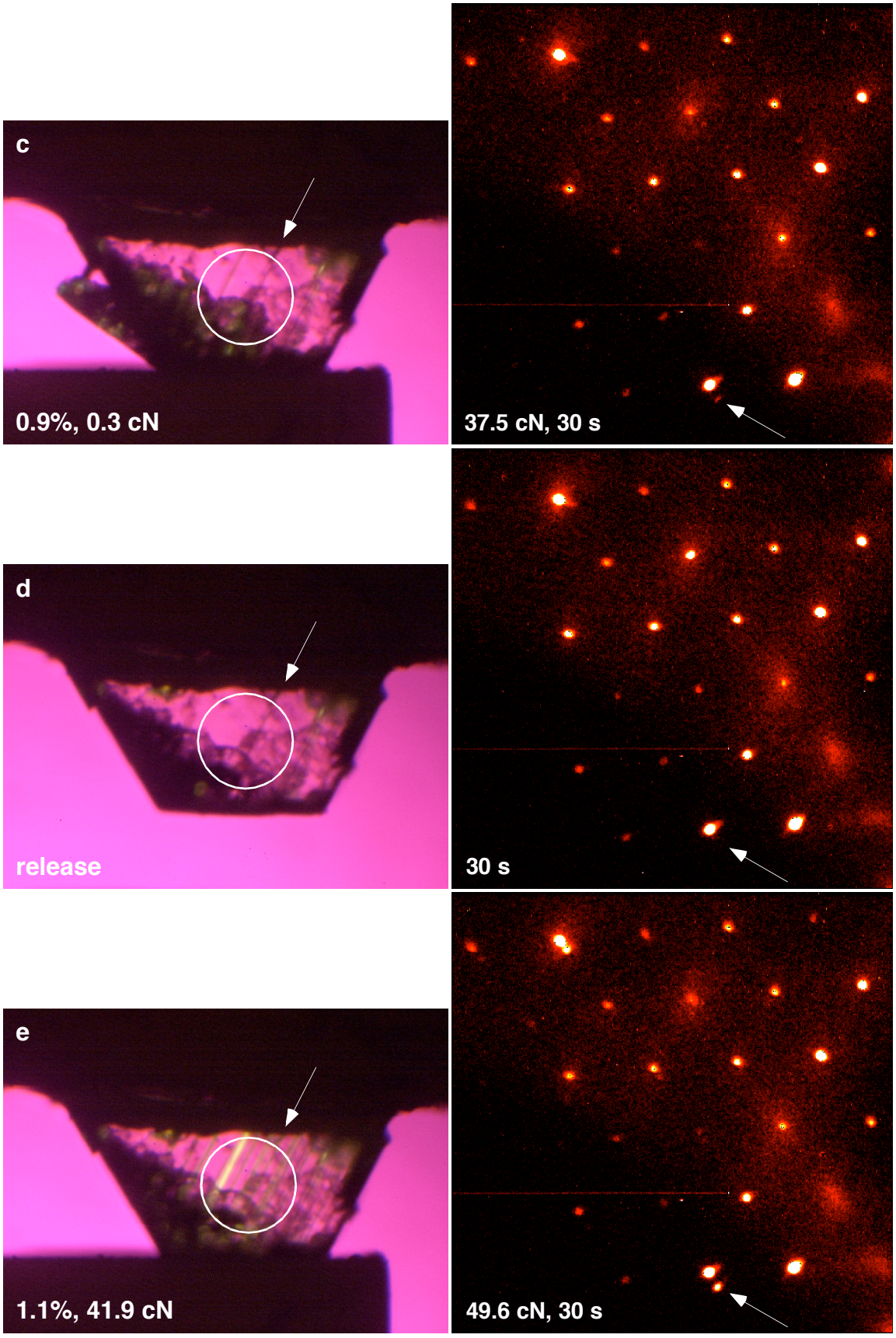
c
0.9%, 0.3 cN
37.5 cN, 30 s
d
release
30 s
e
1.1%, 41.9 cN
49.6 cN, 30 s

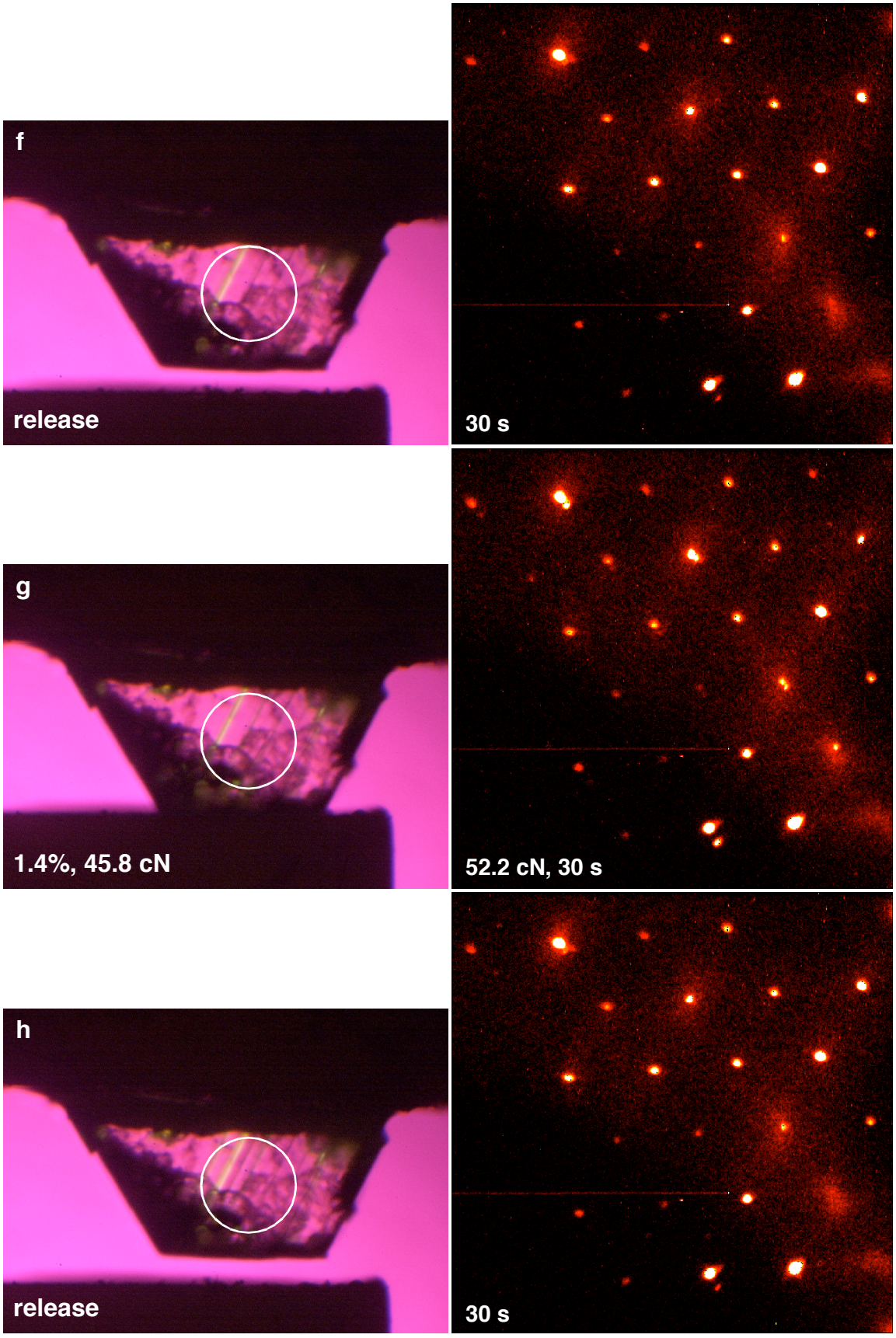
f
release
30 s
g
1.4%, 45.8 cN
52.2 cN, 30 s
h
release
30 s

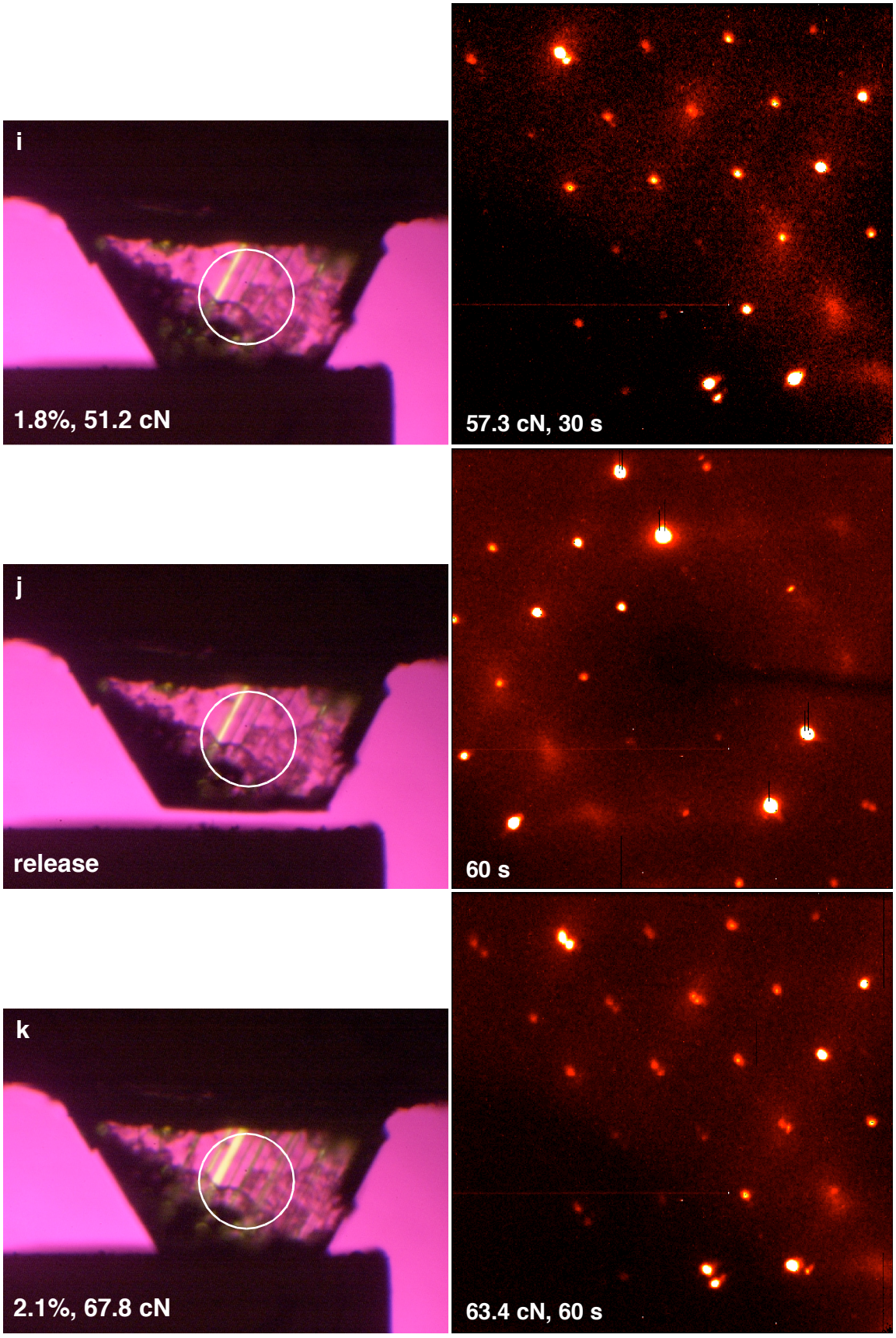
i
1.8%, 51.2 cN
57.3 cN, 30 s
j
release
60 s
k
2.1%, 67.8 cN
63.4 cN, 60 s

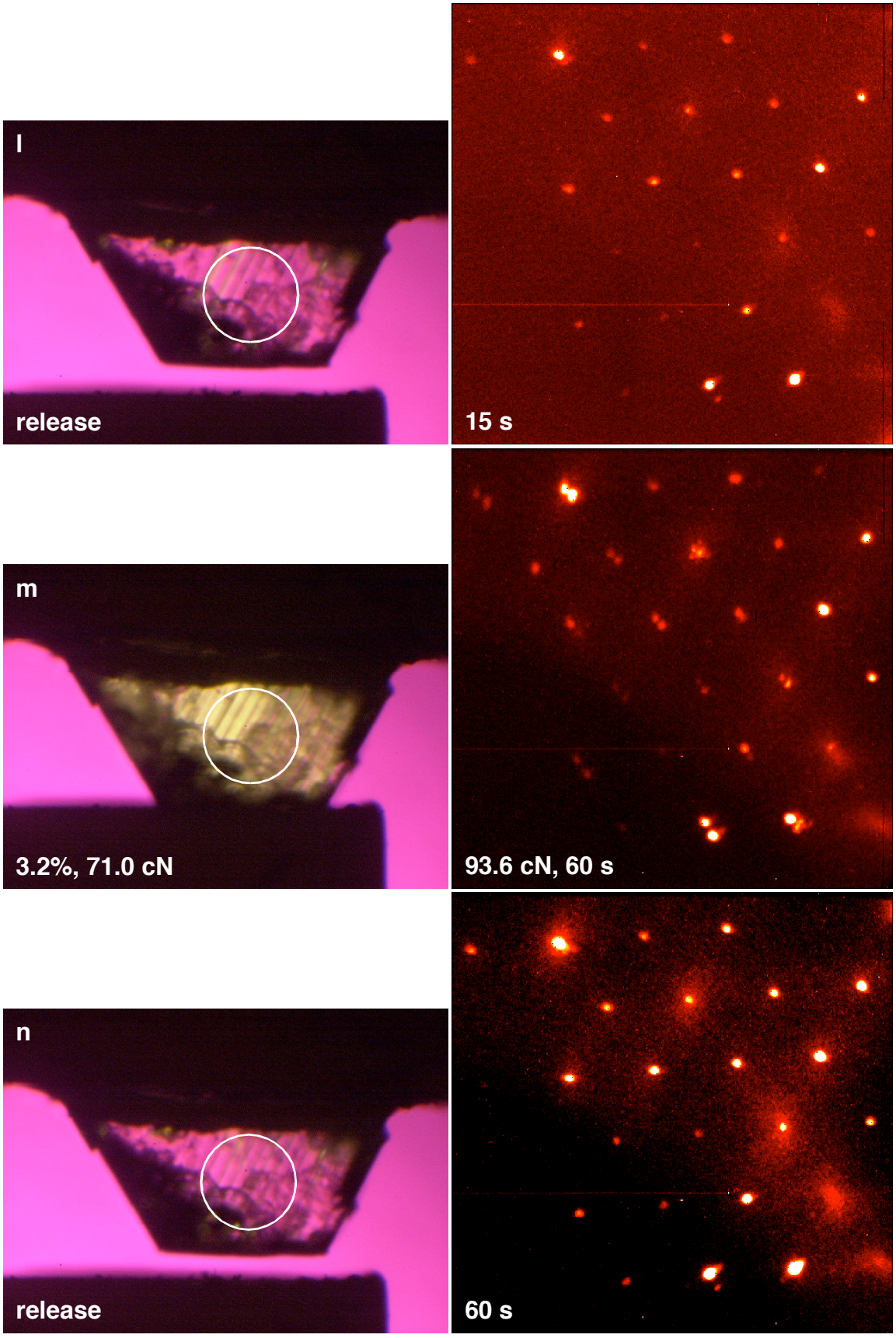
l
release
15 s
m
3.2%, 71.0 cN
93.6 cN, 60 s
n
release
60 s

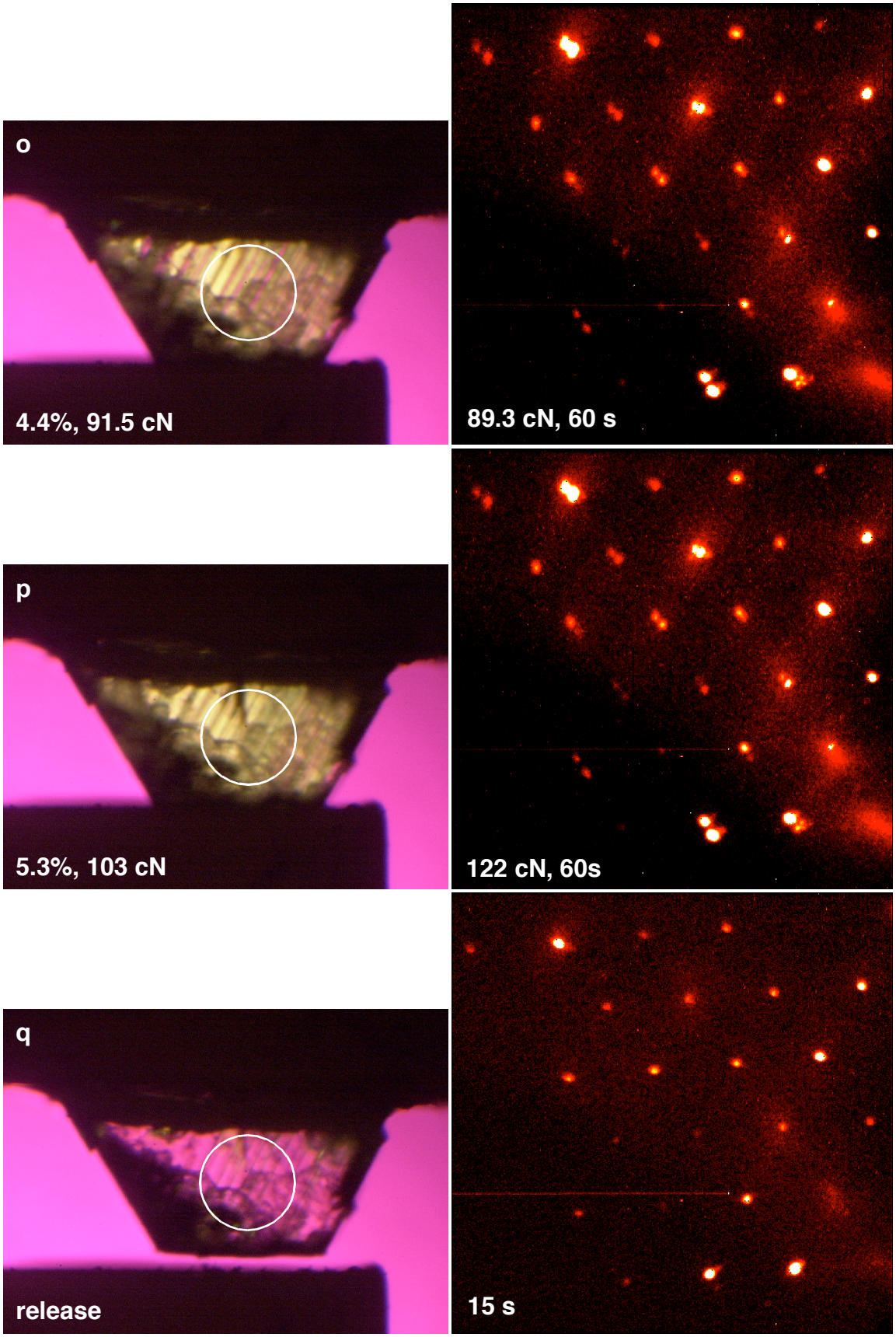
o
4.4%, 91.5 cN
89.3 cN, 60 s
p
5.3%, 103 cN
122 cN, 60s
q
release
15 s

increased in intensity. Upon stress release, the additional reflection disappeared (see arrow in Figure 5.12d), but the band remained in the photomicrograph.

Also apparent is damage to the crystal that occurred immediately following contact with the stress bar (Figure 5.12b). Apparently, a portion of the crystal splintered. Following stress release, this debris was carefully removed with an air duster (note disappearance in Figure 5.12d). This splinter did not affect the visible appearance of the rotation images.

When stressed again, daughter domains became clearly visible in the photomicrographs and the diffraction pattern (Figure 5.12e-f). Following release from 1.4% strain, plastic behavior was observed (Figure 5.12h). Five additional cycles of stress and release were attempted (Figure 5.12i-q). In each attempt, the removal of stress resulted in plastic behavior but not in the emergence of a third set of reflections. At the increased distance between crystal and detector (10 cm) and the high diffraction angles observed ($2\theta = 20°$), the third lattice should be clearly observable. Following the stress experiment, a partial data set was collected for this crystal.[50] Unfortunately, realistic lattice constants were not derived from these data, so the unit cells could were not identified.[51] Was the experiment a failure? Not exactly: it was possible to observe reflections from the daughter domain gain and lose intensity as the crystal was lightly stressed. That reflections attributable to the third orientation were not observed does not mean that nanoscopic twins were not present, nor does it prove that they cannot grow and exert an influence on the ferroelastic behavior of the crystal. For this crystal, the number or size of nanoscopic twins may have been so small that their merged domain with daughter was too small to diffract coherently or to be clearly observed in the diffraction

pattern. In fact, for some crystals the X-ray topographs reveal very weak striations or none at all.[52] Soon, this crystal will be studied with SWBXT to observe its dynamical diffraction contrast. For future experiments it will be essential to screen crystals for striations before (and after) the stress experiment. The synthesis of information collected by topography, stress diffraction, and other experiments may answer unresolved questions and could provide definitive support for whether or submicroscopic domains can be observed using diffraction. In addition, it might be possible to observe a correlation (if one exists) between topograph striation contrast before stress and diffraction intensity for merged twins.

5.2.2 The *Ex Situ* Stress Diffraction Experiment

When a UIC containing a mixture of 2,10-undecanedione and 2-undecanone is subjected to stress, ferroelastic domain reorientation permits the crystal to accommodate this stress and avoid structural damage. In section 5.2.1 it was proposed that nanoscopic twins can reorient in a fashion similar to the bulk "mother" domain. This hypothesis is based on an *in situ* stress-diffraction experiment, in which domains whose ferroelastic distortion was degenerate with respect to the mother were observed. The orientation of this domain is approximately 60° from the mother domain, and, like the mother, opposes the applied stress. Prior to stressing, reflections from this domain were unobserved. At strains of around 2%, reflections from this domain became visible before disappearing at greater compression.

It was further hypothesized that the appearance of these reflections was a consequence of merging portions of the daughter created in the stress experiment and

nanoscopic twins that were already present. Daughter domains created during stress exhibit strain mismatch with these twins, thus creating an energetically unfavorable state. This problem can be remedied by the reorientation of guests in the daughter channels so that they become oriented 180° from those in bordering nanoscopic twins. In the resulting displacive twin, guests are related by 180° rotation about [001] and 5.5 Å translation along [001]. The merohedral nature of this merged domain makes X-ray reflections from contributing daughter and nanoscopic twin coincident.

Because the merged twins are oriented so that their ferroelastic distortion is oriented 30° from the applied stress, they may undergo ferroelastic domain reversion themselves. When this occurs, the merged domains become merohedral with the daughter domains, and their reflection maxima become coincident. Just as the daughter domain may revert on stress release, the merged domain may return to its original orientation so that those reflections become visible once again.

When the merged nanoscopic twin is reoriented (Figure 5.10c to 5.10e), a merohedral twin is formed with the daughter, and reflections from the third orientation disappear. If the diffraction from these displacive regions remains coherent, one might expect the intensity of the daughter to increase accordingly, although the structure factors for specific reflections may change in unpredictable ways because of this disorder. In Chapter 4 it was demonstrated that crystals containing less than 13-14% 2-undecanone can exhibit pseudoelastic behavior when released from very light strains. If the merging of nanoscopic twins (Figure 5.10c,e) is promoted at low strains (as argued in Section 5.2.2), then their population might be increased by repeated compression to strains from which the crystal can spontaneously revert. A final compression to a greater strain from

which domain reversion *does not occur* should lock the daughter and nanoscopic twin into a merohedral lattice such as the one depicted in Figure 5.10e. For this twin, the observed reflection intensity should include contributions from both domains. Since guests in these domains are related by 5.5Å translation and 180° rotation, they might be differentiable using X-ray diffraction. A data set collection combined with careful modeling of the expected twin would hopefully provide a structure solution in which the populations of both twins could be determined using a disordered guest model.

For this experiment, a fragment was cleaved from a crystal grown[53] from a methanol solution containing a 94:6 mixture of 2,10-undecanedione and 2-undecanone (Figure 5.13a-b). This fragment had approximate dimensions of 0.45 × 0.35 × 0.49 mm thick, with flat {110} faces to which compressive stress could be applied. In the stress experiment, the crystal was stressed a total of seven times, to strains of 0.80, 1.1, 0.80, 0.70, 0.80, 1.9 and finally 3.5%.[54] In each successive strain the crystal exhibited some degree of plastic behavior. The final stress, to 3.5% strain, provided a crystal with over 70% permanent daughter domain remaining after stress release (Figure 5.13g-h). The unswitched material was removed to produce a fragment estimated from photomicrographs to be 99% daughter domain. From photomicrographs taken between crossed polars (see Figure 5.13i and j), regions of mother domain and of the third orientation state were observable. (These are presented schematically in Figure 5.13k.) Thus, the domain structure for this crystal included other domains that should contribute to the collected X-ray data.

A search for rotational twins in the high angle reflections was unsuccessful; however, as discussed in Section 5.2.1, reflections from each of the three possible

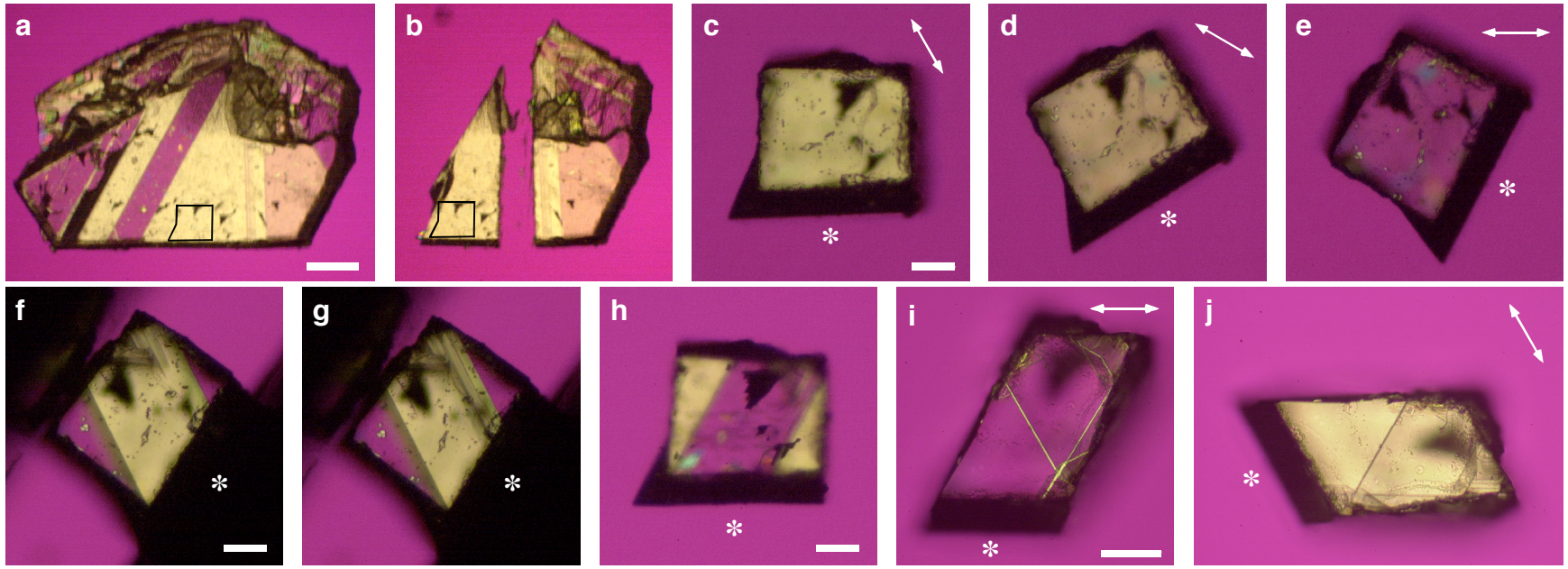

Figure 5.13 A stress experiment performed on a UIC fragment containing a 92:8 mixture of 2-10-undecanedione and 2-undecanone. Photomicrographs taken between crossed polars and with λ plate. **(a,b)** Prior to stressing, the fragment was cut from a larger crystal; its approximate location is outlined in black. Scale bar = 0.50 mm (Meiji, 20x). **(c-e)** The fragment before stress. In each photo, the asterisk (*) indicates the growth face of the fragment and the white arrow denotes the slow axis in the (001) cross section of the mother domain. Scale bar = 0.10 mm (Nikon 5x). **(f,g)** The fragment was stressed a total of seven times. In each cycle the crystal exhibited some plastic domain switching behavior (see text). These photomicrographs were taken during the final stress cycle. The bars of the stress device can be seen at top left and bottom right. Scale bar = 0.10 mm (Nikon 5x). **(f)** At 3.5% strain. Here, the mother is in the extinguishing position (as in **e**), and the slow axis of the daughter domain is oriented so that it lies parallel to the stress bars and growth face (and is therefore perpendicular to the applied stress). **(g)** Following stress release: predominantly plastic domain switching has occurred. **(h)** The fragment after removal from the stress device (crystal orientation as in **c**). Here, the crystal is oriented as in **c** and the daughter is in the extinguishing position (slow axis oriented along the horizontal). Scale bar = 0.10 mm (Nikon 5x). **(i,j)** The unswitched regions were cleaved from the fragment for X-ray diffraction. Scale bar = 0.10 mm (Nikon 10x). In both photos the slow axis orientation of the daughter domain is indicated by the white arrows. **(i)** Fragment oriented as in **c** and **h**. Here, the daughter domain is in the extinguishing position (see arrow). While cleaving, stripes of other domain orientations did appear unexpectedly. From photomicrographs, these regions are estimated to compose less than 1% to the total fragment volume. The domain structure of this crystal is presented schematically in **k**, which includes a copy of the photomicrograph in **i**. **(j)** The fragment rotated 60° CW.

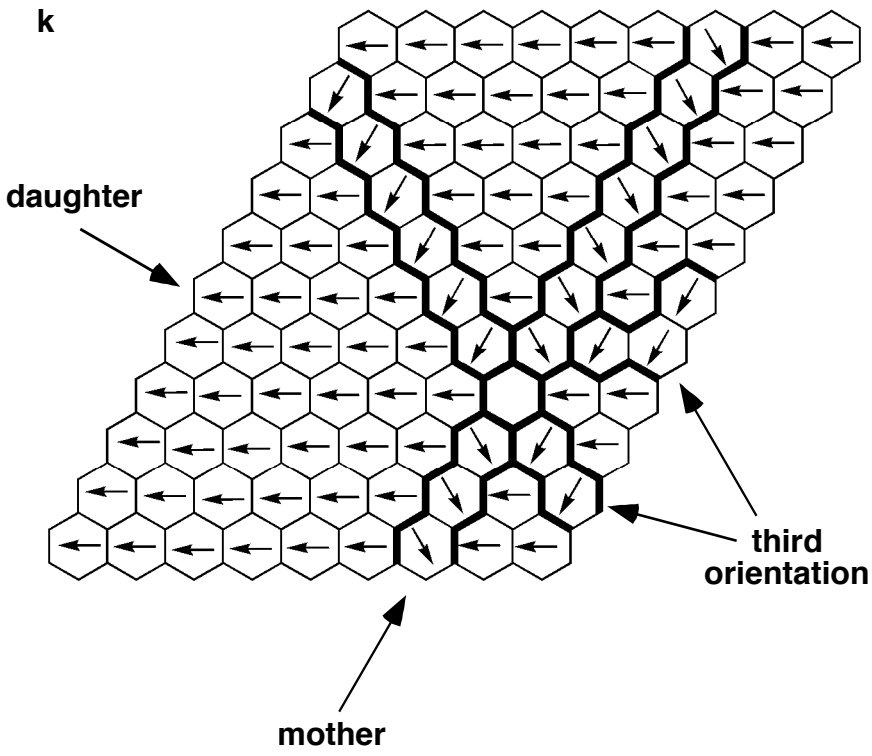
k
daughter
third
orientation
mother

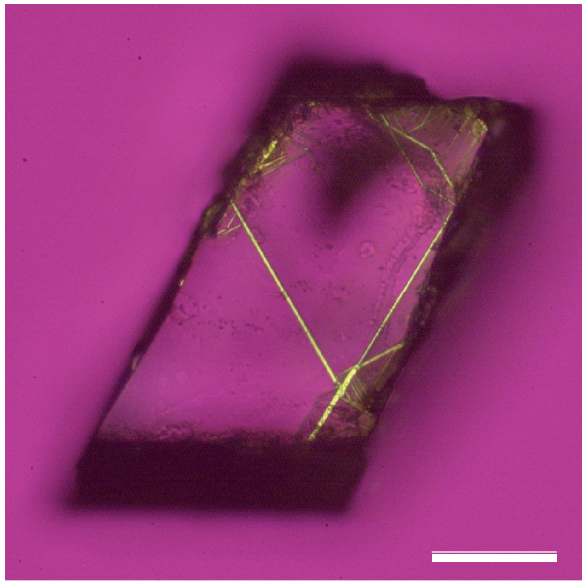

domains should be coincident at low angles. Thus, the integration of these data may include contributions from the other domains, which are related to the first by ±60° rotation. Although the presence of this twin was not accounted for in the structural model, no residual electron density was observable in the final refinements that can be attributed to twinning. This is discussed below.

For this crystal, an X-ray data set was collected[55] and the crystal structure solved. This structure solution was refined initially with only the "major" guest (daughter) sites populated; the 180°/5.5 Å displacive twin was added later to model the expected guest disorder. To identify minor differences in structure, these results were then compared to the structure solution and refinement for an unstressed fragment of a crystal grown in a solution containing a 92:8 mixture of 2,10-undecanedione and 2-undecanone (described below).

The modeling of disorder in the X-ray structure solution for this experiment was approached in much the same fashion as the crystal structure for the UIC containing a mixture of 2,10-undecanedione and 10-bromo-2-decanone.[56] The room temperature crystal structure of 2,10-undecanedione/urea exhibits $C222_1$ space symmetry.[37] However, from the experiment on the mixed crystal containing 10-bromo-2-decanone, it is clear that mixed crystals in this series are better modeled in space group P1. For this symmetry there are 36 ureas and four guests sites in the unit cell, each of which can be refined independently. Each of these was readily located in the structure solution. Since the diketone and monoketone guests occupy similar positions, each guest site was modeled as a mixture of the diketone and undecane. The use of a single molecule of undecane instead of two molecules of 2-undecanone (which account for two possible orientations

of monoketone along the channel) does not account for differences in the populations of monoketone oriented differently along [001]. In Section 2.2.4.2, these differences were shown to be quite small for the crystal containing a mixture of 2,10-undecanedione and 10-bromo-2-decanone, but the end for end recognition in mixtures of 2,10-undecanedione and 2-undecanone is not known for the growth sector in question. However, the purpose of this structure was not to quantify nonrandom occupancies of guest impurities, but to observe the presence of displacive twins created from nanoscopic domains in the ferroelastic crystal. The approximation is preferable because it helps to improve the ratio of data to variable parameters.

At the outset, both crystals were refined with isotropic thermal parameters so that the guest populations could be determined. (Later attempts to refine with anisotropic thermal ellipsoids resulted in non-positive definite thermal parameters. For the displacive twin model, 3314 parameters describe the anisotropic solution, and the ratio of data to parameters is approximately 7:1. For the isotropic model, this ratio is 28:1, so the solution is more tractable.) In refining the isotropic model, one introduces an unnatural constraint to the system that can be manifested in unusually large errors in calculated bond lengths or residual electron density in the Fourier analysis. As shown below, the consistency of bond lengths and angles between this solution and the structure of 2,10-undecanedione/urea[37] and with values determined in other crystal structures[57] suggests that this model is reasonable.

For comparison, the structural model was first applied to an unstressed crystal (Figure 5.14) grown in a methanol solution containing a 92:8 mixture of 2,10-undecanedione and 2-undecanone. For this crystal, data collection was performed[58] at

123 K, and the structure was solved at 0.74 Å resolution. Integration[59] of 21363 unique reflections (15726 > 2σ(I)), constrained to orthorhombic metric symmetry, yields a C-centered lattice with the following constants:

a = 8.2522 (4) Å
b = 13.7593 (7) Å
c = 32.7818 (17) Å

V = 3722.2 (4) Å^3.

In the P1 solution there are four guest sites and 36 ureas. As outlined above, each guest site was modeled as a mixture of undecane and 2,10-undecanedione. Other chemically reasonable constraints and restraints were applied to the crystallographic model. (These are more fully introduced elsewhere.[60]) For each type of guest (diketone or undecane), chemically reasonable 1,2 and 1,3 bond distances and were restrained (using SADI, σ = 0.001), while thermal parameters were constrained (using EADP), between all chemically similar guest sites. For instance, all guest acyl oxygens are restrained to have similar 1-2 and 1-3 bond distances and identical thermal parameters. For the diketone guests, the α-methylenes (C03 and C09) were treated as equivalent (in bond lengths and thermal parameters), as were the β-methylenes (C04 and C08), the acyl carbons (C02 and C10), and the terminal methyl carbons (C01 and C11). Because of their relative isolation from the hydrogen bonding ketone, the three internal guest carbons (C05, C06 and C07) were constrained to have equivalent coordinates in the diketones and alkanes occupying the same guest sites. The application of these restrictions increased the ratio of data to parameters and tended to stabilize the refinement. Finally, in order to discourage unreasonable bond distances at the termini of the undecane guest, the α-β and

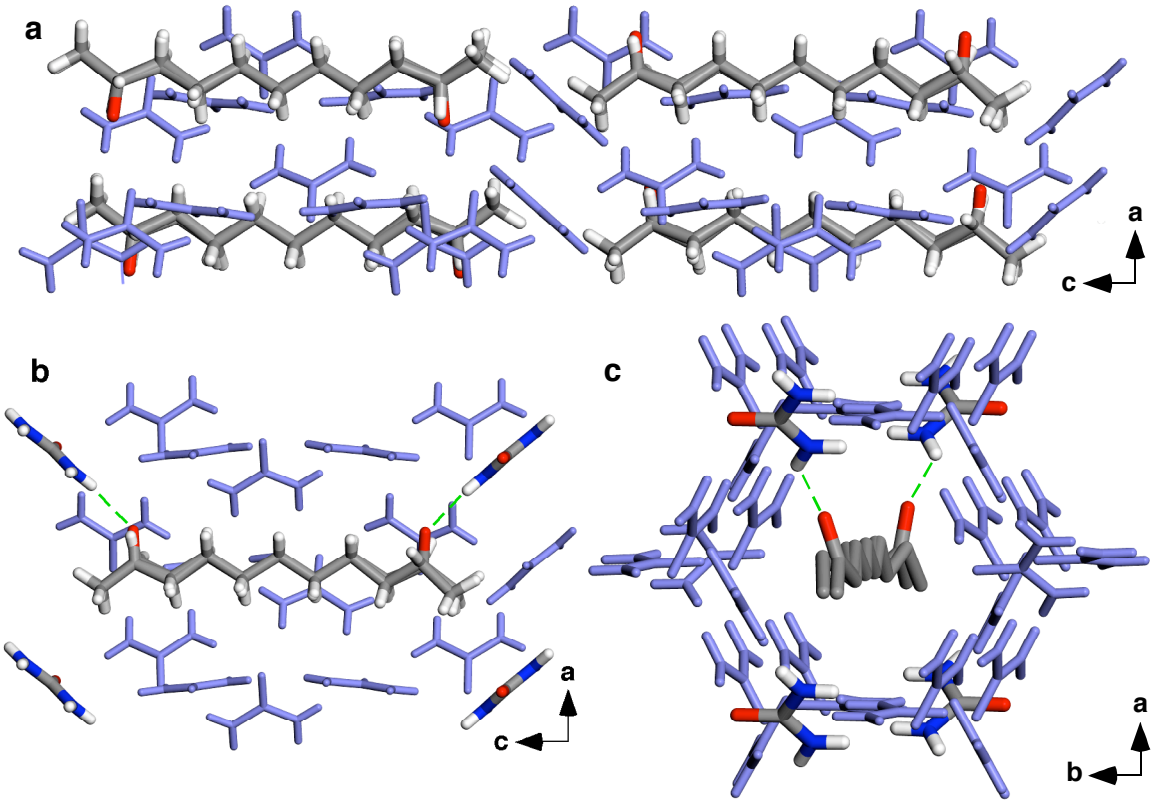

Figure 5.14 The crystal structure solution from an unstressed UIC fragment grown from a methanolic solution containing a 92:8 mixture of 2,10-undecanedione and 2-undecanone. In the P1 solution there are four guests and 36 ureas per unit cell. **(a)** View of the channel along [010] (the arrows indicate unit cell orientation). For clarity, the ureas are colored blue. In this image, the positions of each modelled guest (diketone and undecane) overlap appreciably. **(b)** A single guest site (D), viewed from the same perspective as in **a**. Here, hydrogen bonded ureas are emboldened and hydrogen bonds between them and guest ketones are denoted by the green dashed lines. **(c)** A view of site D along the channel axis. For clarity, the guest hydrogens have been removed and the viewing direction skewed slightly from [001]. The table below provides data on bond distances and angles for the structure, as well as a comparison with values of bond lengths in the literature. (For the literature value column, *n* represents the number of observations for each bond type). Literature data from Allen, *et al.*, *J. Chem. Soc. Perkin Trans. II*, 12, S1-S19, (1987). Thermal ellipsoid plots (50% probability) are included on the following page

	Bond Distances (Å)			**Bond Angles (°)**	
Environment	**Bond**	**Avg. (σ), min, max**	**Literature, *n***	**Bond**	**Avg. (σ), min, max**
Urea	C=O	1.266 (9)	1.256 (7), 24	N–C–N	118.4 (6)
		1.248, 1.285			117.0, 119.7
	C–N	1.333 (11)	1.334 (8), 48	O–C–N	120.8 (6)
		1.300, 1.353			121.9, 119.3
Ketone	C=O	1.214 (0)	1.210 (8), 474	C01–C02–C03	117.4_9 (4)
		1.214, 1.214			117.4, 117.5
	C01–C02	1.474_3 (5)	1.51 (2), 952	C01–C02–O02	122.5_9 (6)
		1.474, 1.475			122.5, 122.7
	C02–C03	1.509_5 (5)	1.51 (2), 952	C03–C02–O02	119.8_0 (4)
		1.509, 1.510			119.8, 119.9
Alkyl Chain	C03→C09	1.520 (12)	1.53 (2), 5777	C03→C09	114.4 (2.3)
	both guests	1.511, 1.547		both guests	109.4, 116.2

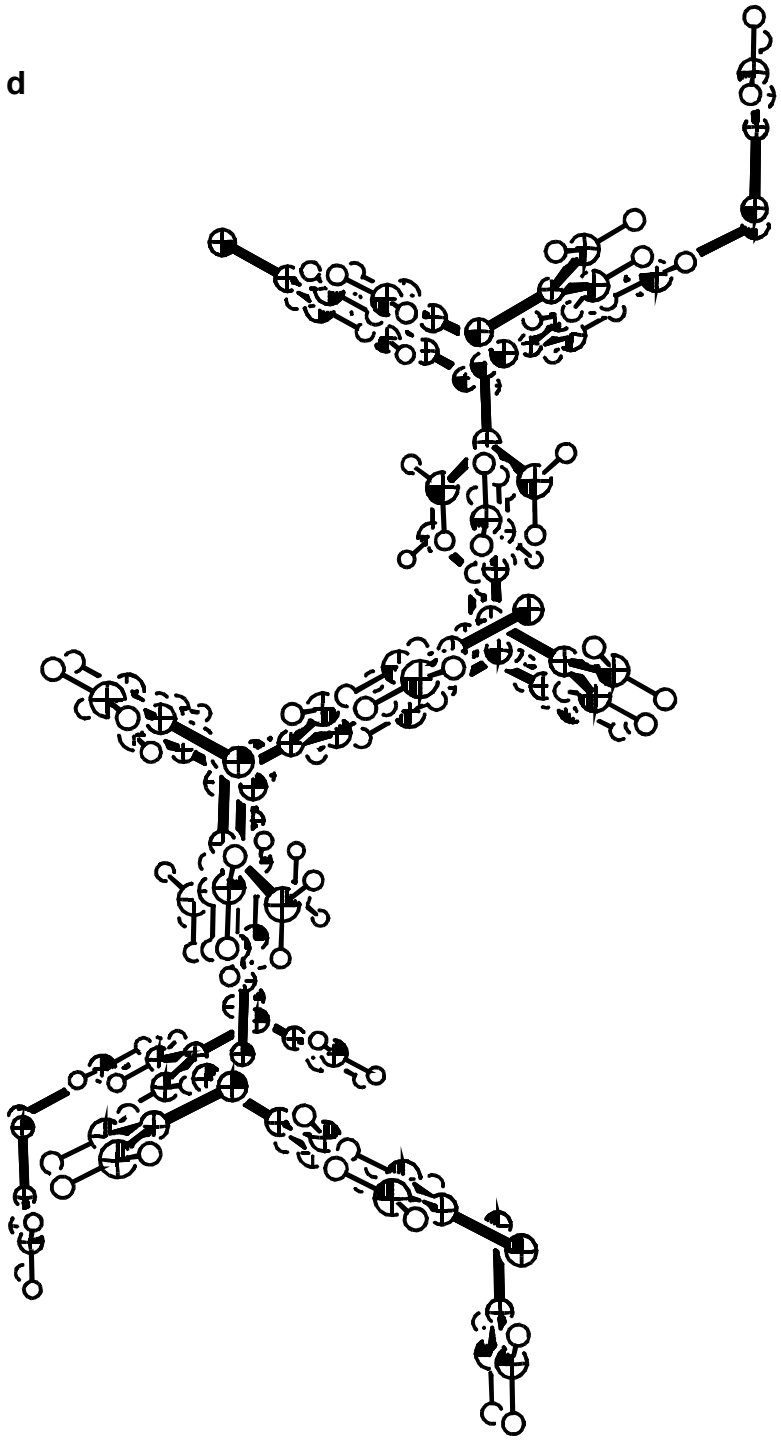

ORTEP plot of the isotropic structure solution, drawn at 50% probability. **(d)** View along the [001] channel, ureas only. This plot was drawn using ORTEP-3 for Windows, Farrugia, L.J., *Journal of Applied Crystallography*, (1997), *30*, 565.

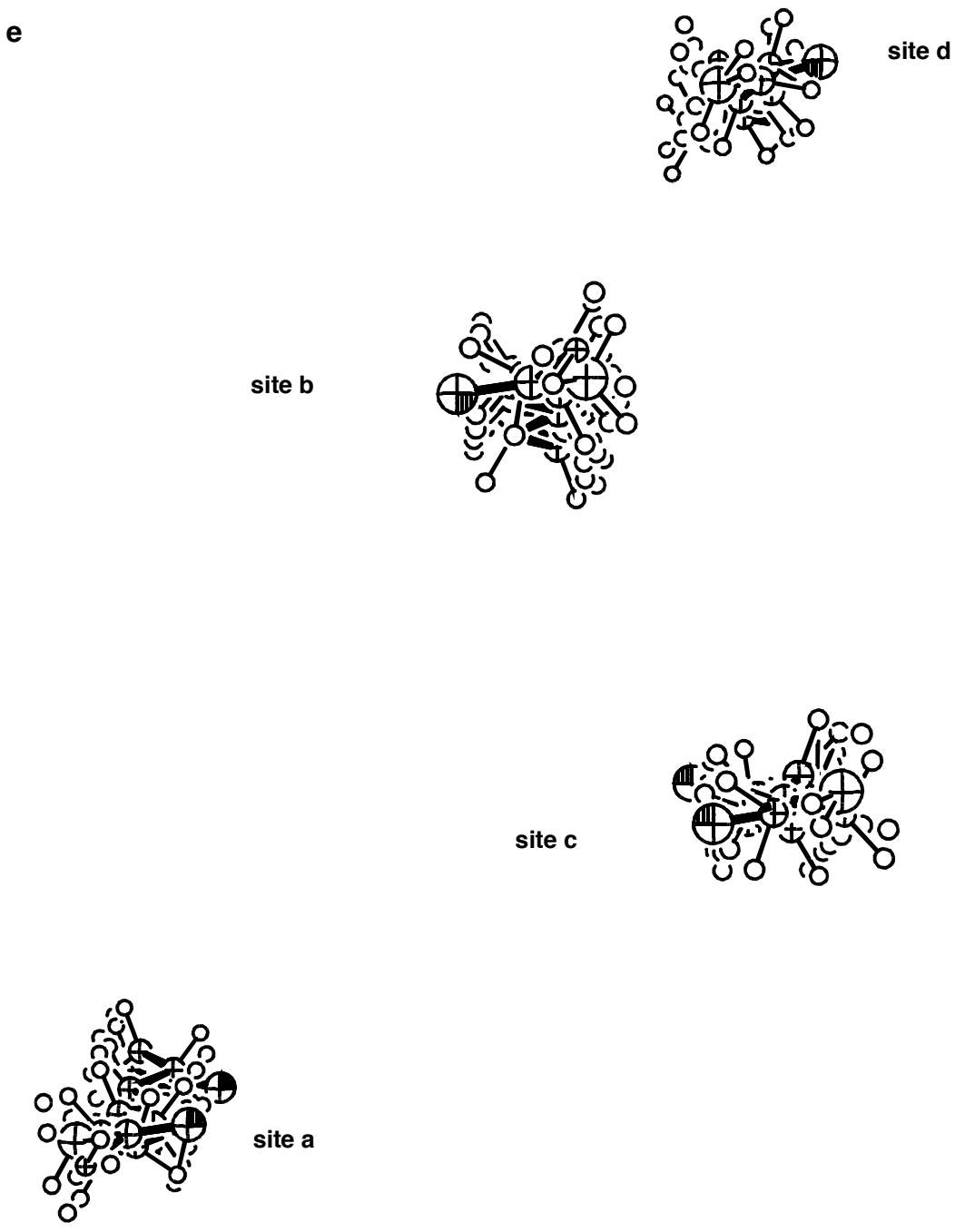

ORTEP plot of the isotropic structure solution, drawn at 50% probability. **(e)** View of the four guest sites, from the same vantage as **d**. This plot was drawn using ORTEP-3 for Windows, Farrugia, L.J., *Journal of Applied Crystallography*, (1997), *30*, 565.

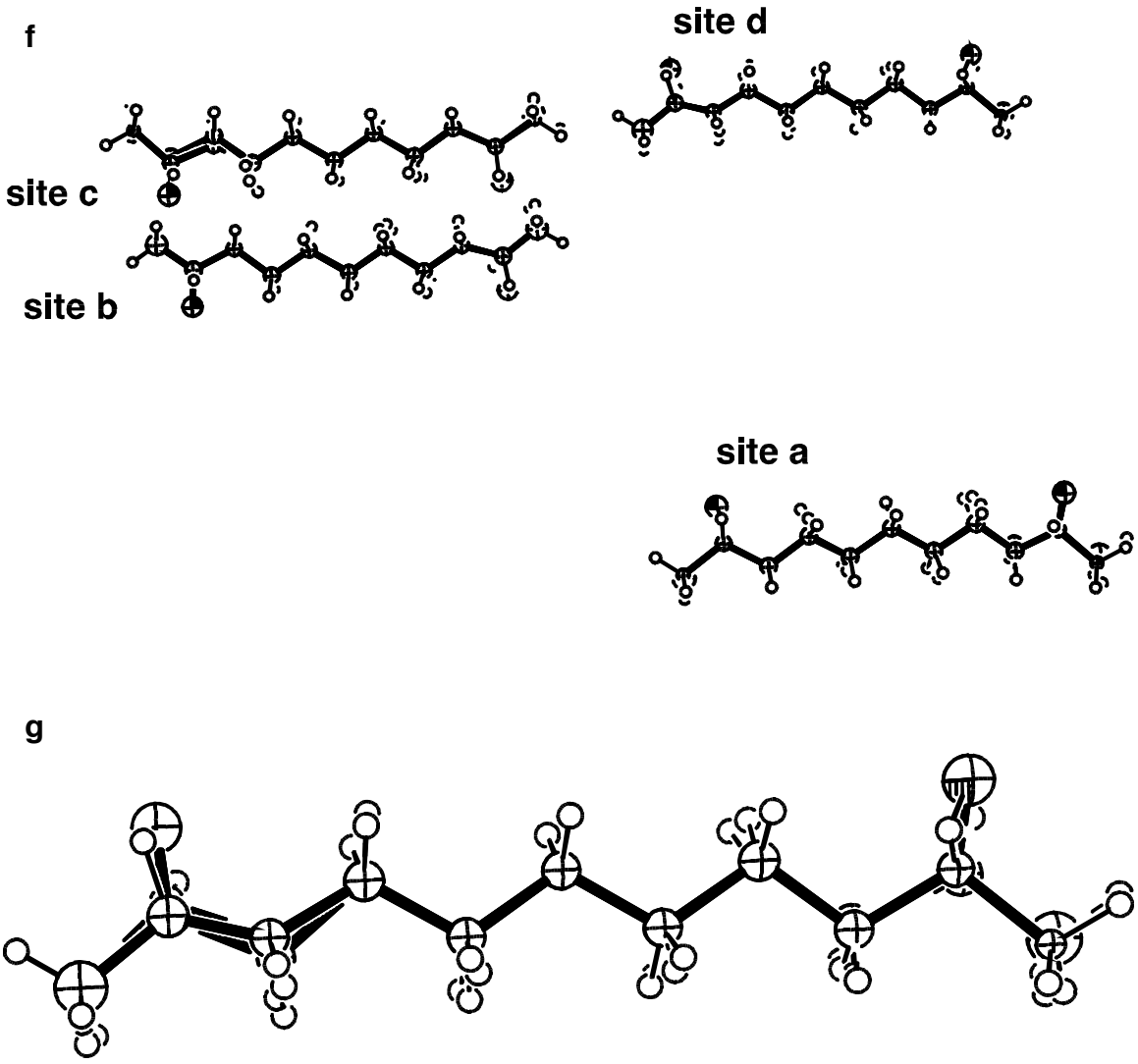

ORTEP plots of the isotropic structure solution, drawn at 50% probability. **(f)** The four guest sites, viewed perpendicular to the channel (parallel to [010]). The ureas are not shown. Two overlapping guests (2,10-undecanedione and undecane) are modeled at each site. **(g)** Close-up view of one guest (D), from the same vantage as **f**. These plots were drawn using ORTEP-3 for Windows, Farrugia, L.J., *Journal of Applied Crystallography*, (1997), *30*, 565.

β-γ carbon bond distances were constrained (using DFIX, σ = 0.01) to 1.50 Å. These distances are similar to those observed in other crystal structures of alkane chains.[57] (Although the constraint of bond distances may not be ideal, it was necessary in order to obtain chemically reasonable bond distances from the available data.[61]) In summary, only the host ureas were not subject to conditions that restrain or constrain their parameters. Finally, the four terminal heavy atoms for each guest (C01, C02, O02 and C03) were restrained to lie in a plane, using the FLAT command.

Initial refinements, in which site populations were allowed to vary, were performed with isotropic thermal parameters. For these, the undecane population refined[62] to about 8%, which translates to about 16% 2-undecanone content. Although this particular crystal was not analyzed for guest content, HPLC analysis of 3 sectors (9 injections total) collected in the same batch gave 10.9 (4)% monoketone.[63] Once the guest populations were defined, (as 10.9% using the FVAR command) anisotropic refinement led to unstable behavior. (When ureas or guest carbon atoms were allowed to refine anisotropically[64], thermal parameters of guest atoms became non-positive definite or the refinement would not converge.) For the isotropic model,[65] the final cycle of full-matrix least-squares refinement was based on 21363 reflections and 821 variable parameters (26:1) with 1421 restraints and converged (mean shift/σ = 0.004 Å and max shift = 0.008 Å for C10D_400z, a methylene carbon on an undecane guest) with unweighted and weighted agreement factors for all data of:

R1 = $\Sigma\{|Fo| - |Fc|\}/\Sigma|Fo| = 0.1244$
wR2 = $\{\Sigma w(Fo^2 - Fc^2)^2/\Sigma[w(Fo^2)]^2\}^{1/2} = 0.3267$
where
$w = 1/(\sigma^2(Fo^2) + (aP)^2$
$a = 0.1$
and
$P = [2(Fc^2) + \max(Fo^2, 0)]/3.$

(For 15724 reflections for which $F_o > 4\sigma(F_o)$, R1 = 0.1073 and wR2 = 0.3126.) For this refinement, the goodness of fit (GooF) was 2.214 (for all data), and the extinction parameter (EXTI) refined to 0.0055. The maximum and minimum peaks in the final difference Fourier map corresponded to 0.895 and -0.761 e/Å^3, respectively. A face-indexed absorption correction was applied[66] using the mass attenuation factors of Creagh and Hubbell.[67] For this crystal, $\mu = 0.104$ mm^{-1} and transmission factors ranged from 0.9565 to 0.9655. This correction yields R(int) = 0.092. The Flack (x) parameter was 0.4(11). For this data, a variety of weighting schemes were applied[68] in which the contribution of P was varied (by changing the value of a in the above expression). Of these, the default SHELXTL weighting scheme provided the most reasonable bond distances and angles. A table of bond distances and angles are provided in Figure 5.14.

Figure 5.14 presents the refined crystal structure. This structure solution appears quite like the structure of 2,10-undecanedione/urea (Chapter 1 and Figure 1.3) and (as solved) possesses a left-handed urea helix with the host-guest hydrogen bonding pattern predicted in Figure 1.8b. For each guest site in the P1 solution, overlap between the pair of modeled guests (diketone and undecane) is appreciable. Guests form hydrogen bonds with every third urea along the {100} faces of the channel. Qualitatively, the unstressed crystal structure is quite similar to that of pure 2,10-undecanedione/urea.

For the stressed crystal (Figure 5.13), an X-ray data set was collected[55] at 116 K. Integration[69] of 23941 unique reflections produced a C-centered orthorhombic cell, with the following cell constants:

a = 8.2640(4) Å
b = 13.7786(7) Å
c = 32.8292(16) Å

V = 3738.1(3) Å^3.

Using the same model applied to the unstressed crystal, an initial refinement produced a structure at 0.74 Å resolution. The final cycle of full-matrix least-squares refinement[70] was based on 23941 reflections and 842 variable parameters (28:1 ratio) with 1329 restraints and converged (mean shift/σ = 0.010 Å and max shift = 0.002 Å for H10I_100z, a methylene hydrogen on an undecane guest) with unweighted and weighted agreement factors for all data of:

R1 = $\Sigma\{|Fo| - |Fc|\}/\Sigma|Fo| = 0.1231$
wR2 = $\{\Sigma w(Fo^2 - Fc^2)^2/\Sigma[w(Fo^2)]^2\}^{1/2} = 0.2913$
where
$w = 1/(\sigma^2(Fo^2) + (aP)^2$
and
$a = 0.1$
$P = [2(Fc^2) + \max(Fo^2, 0)]/3$.

(For 11981 reflections for which $F_o > 4\sigma(F_o)$, R1 = 0.0917 and wR2 = 0.2913) For this refinement the goodness of fit (GooF) was 1.717 (for all data) and the extinction parameter (EXTI) refined to 0.0041. The maximum and minimum peaks on the final difference Fourier map correspond to 0.92 and -0.75 e/Å^3, respectively. The majority of residual electron density is located very near "existing" atoms (primarily the host) and is not attributable to additional guests not present in the current model. A face-indexed absorption correction was applied[71] using the mass attenuation factors of Creagh and

Hubbell.[67] For this crystal, $\mu = 0.104$ mm^{-1} and transmission factors ranged from 0.9641 to 0.9480. This correction yields R(int) = 0.0524. Although this crystal was not analyzed for guest content, HPLC analysis of eight other sectors of crystals collected from the same batch provided a monoketone content of 7.7(5) %.[72] In the refinement, the site occupancy factors were constrained to 7.6% monoketone.

With a satisfactory model of the "major" guest population, it was possible to consider the "minor," displacive, population of the nanoscopic domains. Within a linear channel, the merohedral twin can be displaced in either of two directions. However, the helical nature of the UIC channel favors one option over the other; otherwise, in the process of domain switching (e.g., on going from Figure 5.10c to 5.10e), the strain of the merged domain will at some point directly oppose the applied force. For this crystal, a right-handed helix was found in the crystal structure solution, with Flack (x) parameter = -0.4(10). When the enantiomorph (left-handed helix) was created (using MOVE) and refined,[73] the Flack (x) parameter was 1.2(10). Because the presence of only light elements precludes an accurate determination of absolute stereochemistry by methods such as those of Bijvoet[74] or Flack,[75] the original right-handed solution was used. However, the incorrect assignment of helical chirality does not alter the conclusions based on this structure solution because the stereochemical relationship between the major guest sites and the displacive sites should not change with the chirality of the system.

Upon consideration of molecular models, the minor population of the displacive twin should be shifted from the major population along the +*c* axis. To model this

second site, copies of guests solved using the untwinned model were inserted manually via application[76] of the following transformation operation,

$$\left|-x, y, z + 1/6\right|,$$

which models the 5.5Å/180° displacement. The displacive guest was inserted using the FRAG and FEND commands of SHELXTL. These commands allow the insertion of a group whose geometry is fixed. In other words, the displacive guest was refined as a rigid body that possessed the same intramolecular parameters as members of the major guest population. (A set of restraints and constraints analogous to those applied to the major population was applied to the displacive guests.) This treatment does not permit the addition of rigid body constraints onto the inserted fragment; for this reason, alkyl hydrogens (which are best treated as riding on the coordinates of the atom to which they are attached) were not included in the initial displacive model. (This is because, for inserted fragments, the displacive guests are positioned ("ride") according to atoms C05, C06 and C07, whose coordinates are fixed. Since the guest hydrogens are themselves treated according to a riding model, they cannot be included in the inserted fragments.) Figure 5.15 presents a portion of the structural model. Here, the diketone component of one guest site is pictured (the undecane guest has been removed for clarity); it forms hydrogen bonds with the ureas colored green (1 and 10' in the helical wheel diagram). In the model, the displacive guest (in yellow) is rotated 180° and translated by 5.5 Å along [100] so that it forms hydrogen bonds with ureas 4 and 7' (in red).

The refinement[77] was performed with initial populations of 95% daughter and 5% displacive twin that were allowed to refine against each other as components of the same, unrestrained, free variable (FVAR). (This limits their total population to 100%.) The

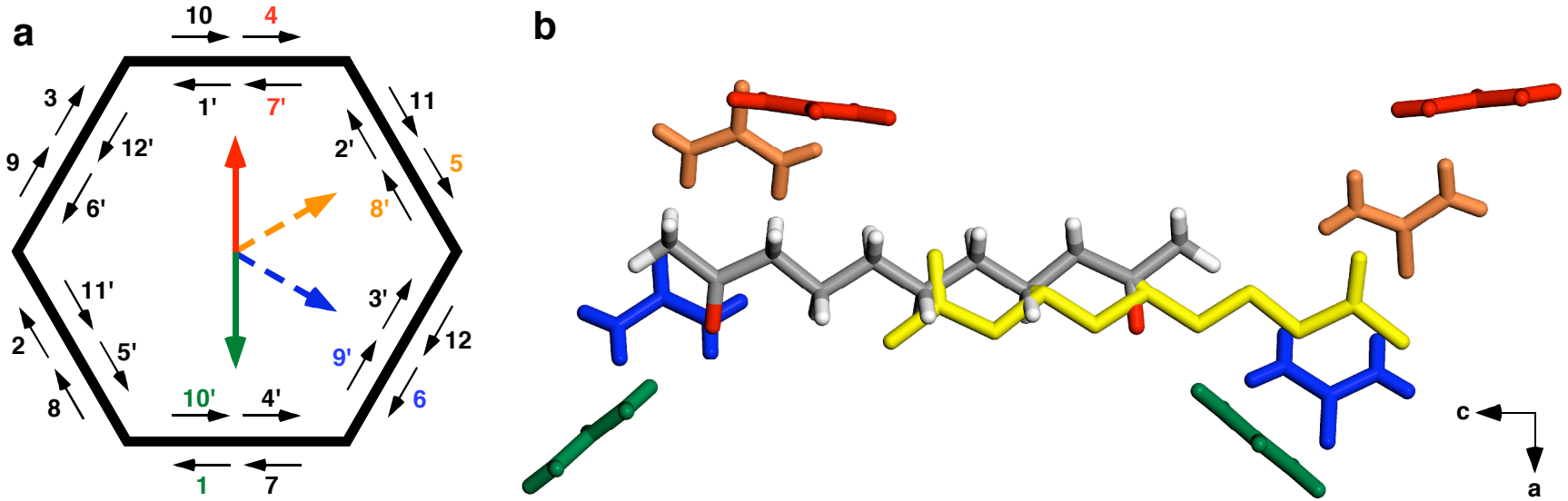

Figure 5.15 Modeling displacive guests in the stressed UIC containing a 92:8 mixture of 2,10-undecanedione and 2-undecanone. In a ferroelastic UIC, guests within different rotational twins should be oriented in a predictable fashion. **(a)** A helical wheel diagram depicting the orientations possible for the guests in various domains in such a crystal. This diagram is representative of the right-handed helices of the crystal structure in **b**: urea (n+1) is related to urea n by a 60° CCW motion along the helix and a translation 1.83 Å away from the viewer (down into the page and along [001]). The colored arrows depict the four guest orientations possible within this crystal. (Here, only one of the guest orientations is shown; the second guest is created from the first by a twofold screw operation.) For instance, the orientation of the mother domain (established from photomicrographs taken prior to stress) is such that the guest is hydrogen bonded to ureas 6 and 9' (blue arrow). For daughter created as stress is applied along the horizontal (see Figure 5.12), guests will translate 1.83 Å along [001] (away from the viewer) and rotate 60° CW so they are directed towards ureas 1 and 10' (green arrow). The nanoscopic twin is thought to be oriented 60° from the mother so that it is degenerate with respect to stress applied along the horizontal. Guests in this domain are are located 1.83 Å along [00$\bar{1}$] and are rotated 60° CCW from guests in the mother; here they will form hydrogen bonds to ureas 5 and 8' (orange arrow). With enough stress, guests in this orientation should undergo ferroelastic domain reorientation, as well. In order that the strain does not oppose the applied stress during the domain switching process, this rotation-translation occurs *in the opposite sense*. Whereas guests within the mother rotate 60° CW and translate 1.83 Å along [001], guests in the nanoscopic twin rotate 60° CCW and translate 1.83 Å along [00$\bar{1}$]. This results in a net displacement of 180° and 5.5 Å between daughter and displacive nanoscopic twin so that its guests are oriented towards ureas 4 and 7' (red arrow). **(b)** The X-ray structure solution for the stressed UIC fragment with data collected at 116 K. Shown here is a single guest site from the X-ray structure solution of the displacive daughter, viewed along [010]. If rotated 90° CW (from above), this picture has the same point of view as the helical wheel in **a**. For clarity, only the diketones for daughter and modeled [00$\bar{1}$] displacive twin (in yellow) are pictured, and ureas not involved in hydrogen bonding with one of the four domains illustrated in **a** have been omitted. Ureas are colored according to the convention in **a**: mother (blue), daughter (green), unmerged nanoscopic twin (orange) and displacive twin (red).

resulting output exhibited convergence to 102% major guest (daughter), or < 0% displacive twin. The refinement statistics and figures of merit resemble those of the "untwinned" model described above. Several attempts at this model with slight variations in initial restraints (including damping factors and initial populations) yielded essentially the same result. For this model, the weighted and unweighted agreement factors for all data were as follows:

R1 = $\Sigma\{|Fo| - |Fc|\}/\Sigma|Fo| = 0.1238$
wR2 = $\{\Sigma w(Fo^2 - Fc^2)^2/\Sigma[w(Fo^2)]^2\}^{1/2} = 0.2933$
where
$w = 1/(\sigma^2(Fo^2) + (aP)^2$
and
$a = 0.1$
$P = [2(Fc^2) + \max(Fo^2, 0)]/3.$

(For 11981 reflections for which $F_o > 4\sigma(F_o)$, R1 = 0.0925 and wR2 = 0.2802.) This refinement converged (mean shift/σ = 0.013 Å and max shift = 0.001 Å for C01D_400z, a terminal methyl carbon for undecane, major site) for a goodness of fit (GooF) of 1.729 (for all data) and an extinction parameter (EXTI) of 0.0038. The maximum and minimum peaks on the final difference Fourier map correspond to 0.93 and -0.86 e/Å^3, respectively.

Although contrary to the known mechanism of ferroelastic domain switching, it was important to test the possibility that the minor twin had been displaced from the major population along the -c axis. Thus, a model analogous to the one above was constructed in which the displaced guest was related to the major site by the following transformation matrix:

$$|-x, y, z - 1/6|.$$

This refinement[78] was conducted in the same fashion as before, with the initial population of the major site set at 95%; again the variable that describes the population of

the displacive twin refined to 102% daughter (< 0% displacive guest). For this model, the weighted and unweighted agreement factors for all data were as follows:

R1 = $\Sigma\{|Fo| - |Fc|\}/\Sigma|Fo| = 0.1235$
wR2 = $\{\Sigma w(Fo^2 - Fc^2)^2/\Sigma[w(Fo^2)]^2\}^{1/2} = 0.2910$
where
$w = 1/(\sigma^2(Fo^2) + (aP)^2$
and
$a = 0.1$
$P = [2(Fc^2) + \max(Fo^2, 0)]/3.$

(For 11981 reflections for which $F_o > 4\sigma(F_o)$, R1 = 0.0920 and wR2 = 0.2777.) This refinement converged (mean shift/σ = 0.020 Å and max shift = 0.008 Å for C01B_200z, a terminal methyl carbon for undecane in the major site) for a goodness of fit (GooF) of 1.714 (for all data) and an extinction parameter (EXTI) of 0.0039. The maximum and minimum peaks on the final difference Fourier map correspond to 0.92 and -0.85 e/Å^3, respectively. The appreciable similarity between the refined output for both models and that of the "untwinned" model indicates the addition of displaced twin has a vanishingly small effect on the capacity for the model to fit the reflection data. In other words, a population that refines to a site occupancy of zero cannot significantly influence the refinement statistics of a model in which it is included. Such a population apparently refines to zero because its presence is not necessary for the model to account for the experimental data. This indicates that the nanoscopic domains within the displacive twin were not detected in this experiment.

It is noted here that a third model, in which the displacive guest was rotated by 180º and translated by 16.5 Å, was not attempted. The presence of such a twin would have required the presence of an initial nanoscopic twin in which the guest is rotated by 60º and translated by 11.0 + 1.83 Å from the guest in the original mother domain. This kind of twinning is conceivable, so it should be considered in addition to the simpler twinning operation that involves a 60º rotation and 1.83Å translation. The second model

described above, in which the displacive guest is translated by 1/6 of the unit cell along -c, is equivalent to the mechanistically reasonable model that one would use for an initial nanoscopic twin in which the guest was rotated by 60º and translated by 22.0 + 1.83 Å from the guest in the mother domain.

The experiment outlined in this section illustrates the difficulty in identifying directly the presence of nanoscopic twins. By stressing the crystal multiple times, it was hoped that a significant percentage of nanoscopic twins would form a displacive twin with the plastic daughter. Careful crystal structure modeling and analysis failed to produce definitive evidence for the nanoscopic twin. The X-ray scattering contribution of the third orientation was not discernable in this experiment even though the crystal was contaminated by twins of the third orientation (Figure 5.13k). Although diffraction contrast in X-ray topographs is thought to indicate their presence, X-ray diffraction is apparently not sensitive enough to detect nanoscopic twins in this particular case.

In light of this negative result, another experiment of this type was performed[79] on a fragment obtained from the same crystal that had provided the unstressed fragment. Six cycles of stress and release were attempted, to 0.24%, 0.15%, 0.45%, 0.35%, 2.28% and 1.74% strain. Although this crystal had already demonstrated predominantly plastic behavior in the previous stress cycle, acoustomechanical vibration was applied for two minutes during the final stress cycle. (At the time this experiment was performed, the effect of acoustomechanical relaxation on domain structure was not well understood.) Subsequent X-ray data collection and analysis were conducted as described above. The refinement of the untwinned model was conducted in the same way as with the other stressed crystal, with the exception that the site occupancy of 2-undecanone, 10.9%, was

the same as that for the unstressed crystal described above.[63] From the data set collected[80] at 123 K, integration[81] of 23246 reflections (constrained to orthorhombic symmetry) produced a C-centered orthorhombic cell, with the following cell constants:

a = 8.2499(4) Å
b = 13.7578(7) Å
c = 32.7966(16) Å

V = 3722.4 (3) Å^3.

This structure solution produced a left-handed urea helix. Here, the Flack (x) parameter was -0.4(11). (Refinement[82] of the structure of the right-handed enantiomorph yielded x = 1.3(11).) For the untwinned model (left-handed helix), the final cycle of full-matrix least-squares refinement[83] was based on 23246 reflections and 842 variable parameters (28:1 ratio) and converged (mean shift/σ = 0.021 Å and max shift = 0.001 Å for C01B_200z, a terminal methyl carbon on an undecane guest) with unweighted and weighted agreement factors for all data of:

R1 = $\Sigma\{|Fo| - |Fc|\}/\Sigma|Fo| = 0.1224$
wR2 = $\{\Sigma w(Fo^2 - Fc^2)^2/\Sigma[w(Fo^2)]^2\}^{1/2} = 0.3597$
where
$w = 1/(\sigma^2(Fo^2) + (aP)^2$
and
$a = 0.1$
$P = [2(Fc^2) + \max(Fo^2, 0)]/3$.

(For 11981 reflections for which $F_o > 4\sigma(F_o)$, R1 = 0.1135 and wR2 = 0.3480.) Here, the goodness of fit (GooF) of 2.580 (for all data) and the extinction parameter (EXTI) refined to 0.0022. The maximum and minimum peaks on the final difference Fourier map correspond to 0.96 and -0.82 e/Å^3, respectively. A face-indexed absorption correction was applied[84] using the mass attenuation factors of Creagh and Hubbell.[67] For this

crystal, $\mu = 0.105$ mm^{-1} and transmission factors ranged from 0.9497 to 0.9694. This correction yields R(int) = 0.076.

For this crystal, the displacive twin was modeled in the same fashion as discussed above. Unfortunately, refinements performed that incorporated the displacive twin translated in either direction along the channel (along +*c* or -*c*) were not stable.[85] Because the model and the restrictions applied to it were the same for both crystals examined, it is not clear why these refinements were unsuccessful.

In a stressed crystal, it is likely that a large majority of the observed reflection intensity is due to the daughter; only a vanishing fraction arises from the merohedral twin. This experiment, which involves modeling diffraction data for populations close to zero, is obviously difficult to perform successfully. A negative result, though discouraging, does not prove the absence of nanoscopic twinning. Indeed, the observation of diffraction contrast and the growth of domains of the third orientation state support the hypothesized presence of nanoscopic twins. Although as of yet unproven, it is possible that for a given crystal the number (or size) of nanoscopic twins may be related to the intensity of striations observed in X-ray topographs. None of the crystals in this experiment were screened with SWBXT; future experiments will require prescreening for striation intensity prior to stress or diffraction experiments.

5.3 Discussion

The experiments described in the preceding chapter outline progress that has been made in identifying the source of the ferroelastic memory effect in urea inclusion compounds containing 2,10-undecanedione and 2-undecanone. The identification of

nanoscopic ferroelastic domains was instrumental in the development of the current model for pseudoelasticity. In a crystal under stress, strain mismatch between adjacent domains is thought to play an important role in the energetics of the ferroelasticity in UICs. Thus, the energetics of strain epitaxy or lack thereof can facilitate or inhibit pseudoelastic domain reversion and may ultimately control ferroelastic behavior.

A more thorough understanding of pseudoelasticity in urea inclusion compounds will arise from the study of nanoscopic twinning and strain epitaxy between these and other domains. The observation of nanoscopic twinning using X-ray topography represented a large step forward in this research. In the stress-diffraction experiment, the emergence of X-ray reflections of a third domain orientation for a crystal under stress suggests some process by which the nanoscopic twins may be enlarged; the behavior of these reflections as a function of crystal strain provides important insights into the nature of this process. The 60° rotational correspondence between mother, daughter and third orientation allows facile prediction of which domains should exhibit strain epitaxy (or mismatch) at their boundaries and under what conditions these orientation states are favored.

Greater insights into nanoscopic twinning and its effect on pesudoelasticy will require the use of a crystal for which intense striations have been observed using X-ray topography. If the striation intensity is related to the number of nanoscopic twins, then such a crystal should produce reasonable intensity for the third domain orientation when stressed on a diffractometer. A carefully performed experiment of this kind will involve smaller increments of strain and the collection of X-ray rotation images and optical photos without the need for large changes in the position of the crystal, which have

indeterminate influences on the experiment. Such an experiment can more accurately identify the parameters (strain, applied force, etc.) that give rise to the emergence of reflections due to merged nanoscopic twins and determine, with greater certainty, whether or not new domains are detected via diffraction before they become visible optically.

There are many questions that can be addressed by an experiment of this sort. For crystals with different striation intensities, do the parameters relating strain and the observation of merged twins vary? For a crystal with no striation contrast, is it still possible to observe merging of nanoscopic twins? Does this affect pseudoelastic reversibility? Does the composition of the crystal have an effect on the merging process? Does the distribution of guest populations (if present) have a measurable effect on the ferroelastic behavior? What additional energetic influences are present? Are such factors compatible with the current mechanistic model? These and many other questions may be approached from a more sophisticated stress-diffraction experiment.

Certainly the findings discussed herein are analogous to phenomena observed in other types of ferroelastic materials. As discussed in Chapter 1, materials exhibiting superelastic and rubber-like behavior are also pseudoelastic. For these, the diffusionless nature and random distribution of stressed-defects in martensitic alloys makes the driving force for rubber-like behavior and superelasticity a *volume effect*.[86] However, for the ferroelastic UICs, the interactions between strain-mismatched twins occur along the relatively lamellar twin boundaries; here, the effect can be considered an *interfacial effect*. (It may be argued, though, that the process of merging nanoscopic twins reduces the lamellar features of these sites.[2]) The memory effect in martensitic shape-memory

alloys has been demonstrated to depend on the symmetry relationship between point defects and their surroundings.[22-25] For these materials, point defects within the parent phase retain the parent symmetry when the alloy is deformed. In much the same fashion as in UICs, strain mismatch between the defects and the newly created daughter domain provides the driving force for pseudoelasticity. For both sorts of materials, annealing involves repair of the symmetry mismatch within the daughter phase, which leads to its stabilization. In this regard, urea inclusion compounds appear very similar to a large variety of functional, technologically important materials.

References Cited

1. Dudley, M. "Topography, X-ray" in *Encyclopedia of Applied Physics*, vol. 21 (ed. Trigg, G. L.) (Wiley-VCH, Berlin, 1997) pp. 533-547.
2. Hollingsworth, M. D., Peterson, M. L., Rush, J. R., Brown, M. E., Abel, M. J., Black, A. A., Dudley, M., Raghothamachar, B., Werner-Zwanziger, U., Still, E. J. & Vanecko, J. A. Memory and perfection in ferroelastic inclusion compounds. *Cryst. Growth Des.* **5**, 2100-2116 (2005).
3. Hollingsworth, M. D., Brown, M. E., Dudley, M., Chung, H., Peterson, M. L. & Hillier, A. C. Template effects, asymmetry, and twinning in helical inclusion compounds. *Angew. Chem. Int. Ed.* **41**, 965-969 (2002).
4. Hollingsworth, M. D. Personal Communication to J. R. Rush (2006).
5. Darwin, C. G. The reflexion of X-rays from imperfect crystals. *Philos. Mag.* **43**, 800-829 (1922).
6. Glusker, J. P., Lewis, M. & Rossi, M. *Crystal Structure Analysis for Chemists and Biologists*, (VCH Publishers, Inc., New York, 1994), pp. 210-211.
7. Hartshorne, N. H. & Stuart, A. *Crystals and the Polarising Microscope*, (Edward Arnold, Ltd., London, 1970), pp. 13-19.
8. Dunitz, J. D. *X-ray analysis and the Structure of Organic Molecules*, (VCH Publishers, Inc., New York, 1995), pp. 290-297.
9. Zachariasen, W. J. A general theory of X-ray diffraction in crystals. *Acta Crystallogr. A* **23**, 558-564 (1967).
10. Robertson, J. M. *Organic Crystals and Molecules*, (Cornell University Press, Ithaca, 1953), pp. 90-91.
11. Ewald, P. P. Introduction to the dynamical theory of X-ray diffraction. *Acta Crystallogr. A* **25**, 103-108 (1969).
12. Dudley, M. & Huang, X. "X-ray Topography" in *Characterisation of Optoelectronic Materials*, (ed. Jiminez, J.) (Taylor and Francis, Oxford, 2003) Chapter 7.
13. Yoneda, Y., Kohmura, Y., Suzuki, Y., Hamazaki, S.-I. & Takashige, M. X-ray diffraction topography on a $BaTiO_3$ crystal. *J. Phys. Soc. Japan* **73**, 1050-1053 (2004).
14. Liu, W. J., Jiang, S. S., Ding, Y., Wu, X. S., Wang, J. Y., Hu, X. B. & Jiang, J. H. Synchrotron radiation topographic observation of $KTiOPO_4$ crystals under an electric field. *J. Appl. Crystallogr.* **32**, 187-192 (1999).
15. Keye, E. T. & Annis, A. D. Studies of phases, phase transitions and properties of some PLZT ceramics. *Ferroelectrics* **5**, 77-89 (1973).
16. Carl, K. & Geisen, K. Dielectric and optical properties of a quasi-ferroelectric PLZT ceramic. *Proc. IEEE* **61**, 967-974 (1973).
17. Leonowicz, M. E. & Vaughan, D. E. W. Proposed synthetic zeolite ECR-1 structure gives a new zeolite framework topology. *Nature (London)* **329**, 819-821 (1987).
18. Megaw, H. D. Temperature changes in the crystal structure of barium titanate oxide. *Proc. Roy. Soc. A* **189**, 261-283 (1947).

19. Fong, D. D., Stephenson, G. B., Streiffer, S. K., Eastman, J. A., Auciello, O., Fuoss, P. H. & Thompson, C. Ferroelectricity in ultrathin perovskite films. *Science (Washington, D. C.)* **304**, 1650-1653 (2004).
20. Aizu, K. Possible species of "ferroelastic" crystals and of simultaneously ferroelectric and ferroelastic crystals. *J. Phys. Soc. Japan* **27**, 387-96 (1969).
21. Aizu, K. Possible species of ferromagnetic, ferroelectric and ferroelastic crystals. *Phys. Rev. B* **2**, 754-772 (1970).
22. Marukawa, K. & Tsuchiya, K. Short-range ordering as the cause of the rubber-like behavior in alloy martensites. *Scripta Metall. Mater.* **32**, 77-82 (1995).
23. Suzuki, T., Tonokawa, T. & Ohba, T. Role of short-range order in martensitic transformation. *J. Phys. IV* **5**, 1065-1070 (1995).
24. Ren, X. & Otsuka, K. Origin of rubber-like behavior in metal alloys. *Nature (London)* **389**, 579-581 (1997).
25. Ren, X. & Otsuka, K. Universal symmetry property of point defects in crystals. *Phys. Rev. Lett.* **85**, 1016-1019 (2000).
26. Ren, X. Large electric-field-induced strain in ferroelectric crystals by point-defect-mediated reversible domain switching. *Nature Materials* **3**, 91-94 (2004).
27. Otsuka, K. & Ren, X. Mechanism of martensite aging effect. *Scripta Mater.* **50**, 207-212 (2003).
28. Rush, J. R. Laboratory notebook entry jrr-e063. (2004).
29. Rush, J. R. Laboratory notebook entry jrr-e073; X-ray data set jr0417. (2004).
30. Rush, J. R. Laboratory notebook entry jrr-d075. X-ray data collection jr04171, frames 221 through 341. (2004).
31. Rush, J. R. Laboratory notebook entry jrr-e072. (2004).
32. Rush, J. R. Laboratory notebook entry jrr-d165. (2004).
33. Rush, J. R. See, for instance, laboratory notebook entry jrr-e073-13. (2004).
34. Rush, J. R. Laboratory notebook entries jrr-e073 through jrr-e075. For stress strain data, see file jrr-e073 stress strain.xls. (2004).
35. Rush, J. R. Laboratory notebook entry jrr-e073. (2004).
36. Rush, J. R. Laboratory notebook entry jrr-e089; X-ray data set jr0420. (2004).
37. Brown, M. E. & Hollingsworth, M. D. Stress-induced domain reorientation in urea inclusion compounds. *Nature (London)* **376**, 323-327 (1995).
38. Hollingsworth, M. D. & Peterson, M. L. SWBXT experiments performed at Brookhaven National Laboratory. (2001).
39. Busing, W. R. & Levy, H. A. Angle calculations for 3- and 4-circle X-ray and neutron diffractometers. *Acta Crystallogr.* **22**, 457-464 (1967).
40. Sheldrick, G. M. ShelXTL-97. Program for crystal structure refinement. (1997).
41. Chung, H., Dudley, M., Brown, M. E. & Hollingsworth, M. D. Synchrotron white beam x-ray topography characterization of defect structures in 2,10-undecanedione/urea inclusion compounds. *Mol. Cryst. Liq. Cryst.* **276**, 203-212 (1996).
42. Sands, D. E. *Vectors and Tensors in Crystallography*, (Dover Publications, Inc., New York, 1995), p. 170.
43. Rush, J. R. Laboratory notebook entries jrr-f163, jrr-f168 and jrr-f229. See jrr-f229 transformations.xls. (2006).

44. Hollingsworth, M. D. & Rush, J. R. Unpublished observations. See e073-19assignments.xls, 170_12L.bmp, 170_12M.bmp, 170_12R.bmp (2006).
45. Rush, J. R. Laboratory notebook entries jrr-e221 through jrr-e226. (2005).
46. Cahn, R. W. Twinned Crystals. *Adv. Phys.* **3**, 363-445 (1954).
47. Yeates, T. O. "Detecting and overcoming crystal twinning" in *Methods in Enzymology*, vol. 276 (eds. Abelson, J. N., Simon, M. I., Sweet, R. M., Carter, C. W., Jr. & Carter, C. W.) (Elsivier Science and Technology, San Diego, 1997) pp. 344-358.
48. Hollingsworth, M. D., Peterson, M. L., Pate, K. L., Dinkelmeyer, B. D. & Brown, M. E. Unanticipated guest motion during a phase transition in a ferroelastic inclusion compound. *J. Am. Chem. Soc.* **124**, 2094-2095 (2002).
49. Peterson, M. L. Laboratory notebook entry MLP-a-242-10. (1999).
50. Rush, J. R. Laboratory notebook entries jrr-e227 through e233. XRD data set jr0507. (2005).
51. Rush, J. R. Laboratory notebook entry jrr-f156. (2007).
52. Hollingsworth, M. D. Personal Communication to J. R. Rush (2005).
53. Rush, J. R. Laboratory notebook entry jrr-d169. (2004).
54. Rush, J. R. Laboratory notebook entry jrr-e123 through jrr-e125. (2005).
55. Rush, J. R. Laboratory notebook entry jrr-e137. (2005).
56. Rush, J. R. & Hollingsworth, M. D. Unpublished Observation. See X-ray structure solution jr0402. (2004).
57. Allen, F. H., Kennard, O., Watson, D. G., Bremmer, L., Orpen, G. & Taylor, R. Tables of bond lengths determined by X-ray and neutron diffraction. Part 1. Bond lengths in organic compounds. *J. Chem. Soc. Perk. Trans. 2*, S1-S19 (1987).
58. Rush, J. R. Laboratory notebook entry jrr-e047. (2005).
59. Rush, J. R. Laboratory notebook entry jrr-e049. (2005).
60. Rush, J. R. Crystal structure report for X-ray structure solution jr0414: jr0414 v1.doc. (2007).
61. Rush, J. R. Laboratory notebook entry jrr-e057-2. (2004).
62. Rush, J. R. Laboratory notebook entry jrr-f258-2. (2007).
63. Rush, J. R. Laboratory notebook entries jrr-d237-7, jrr-d237-8 and jrr-d237-9. See data file jr0413 like xtal hplc.xls. (2004).
64. Rush, J. R. Laboratory notebook entry jrr-e097-3. (2005).
65. Rush, J. R. Laboratory notebook entry jrr-f258-3. Crystal structure solution jr0414; filename f258-3.ins. (2007).
66. Rush, J. R. Laboratory notebook entry jrr-e049-6. (2004).
67. Creagh, D. C. & Hubbell, J. H. "mass attenuation factors = absorption coeff" in *International Tables for Crystallography, volume C*, vol. C (ed. Wilson, A. J. C.) (Kluwer Academic Publishers, 1992) Table 4.2.4.3, pages 200-206.
68. Rush, J. R. Laboratory notebook entry jrr-f259. See structure report jr0414. (2007).
69. Rush, J. R. Laboratory notebook entry jrr-e157. (2005).
70. Rush, J. R. Laboratory notebook entry jrr-f176-2. Crystal structure solution jr0501. (2006).

71. Rush, J. R. Laboratory notebook entry jrr-e157-3. (2005).
72. Rush, J. R. Laboratory notebook entry jrr-d243. (2004).
73. Rush, J. R. Laboratory notebook entry jrr-e157-7. Crystal structure solution jr0501, jrr-e157-7.res. (2005).
74. Bijvoet, J. M., Peerdeman, A. F. & van Bommel, A. J. Determination of the absolute configuration of optically active compounds by means of X-rays. *Nature (London)* **168**, 271-2 (1951).
75. Flack, H. D. On enantiomorph-polarity estimation. *Acta Crystallogr.* **A39**, 876-881 (1983).
76. Rush, J. R. Laboratory notebook entry jrr-e104. Filename e104 displacive.xls. (2004).
77. Rush, J. R. Laboratory notebook entry jrr-f178-2. Crystal structure solution jr0501. (2006).
78. Rush, J. R. Laboratory notebook entry jrr-f177-2. Crystal structure solution jr0501. (2006).
79. Rush, J. R. Laboratory notebook entry jrr-e016. X-ray data set jr0413. (2004).
80. Rush, J. R. Laboratory notebook entry jrr-e016. (2004).
81. Rush, J. R. Laboratory notebook entry jrr-e050. (2004).
82. Rush, J. R. Laboratory notebook entry jrr-f261-5. Crystal structure solution jr0413; filename f261-5.ins. (2007).
83. Rush, J. R. Laboratory notebook entry jrr-f261-4. Crystal structure solution jr0413; filename f261-4.ins. (2007).
84. Rush, J. R. Laboratory notebook entry jrr-e104-4. (2004).
85. Rush, J. R. Laboratory notebook entry jrr-f140. (2006).
86. Lieberman, D. S., Schmerling, M. A. & Karz, R. W. "Ferroelastic "memory" and mechanical properties in gold-cadmium" in *Shape Memory Effects in Alloys*, (ed. Perkins, J.) (Plenum Press, Ltd., New York, 1975) pp. 203-244.